UNIVERSITY OF CALIFORNIA

Los Angeles

Dynamic Shape-changing Hydrogels for Tissue Engineering

A dissertation submitted in partial satisfaction of the

requirements for the degree Doctor of Philosophy

in Bioengineering

by

Stephanie Marie Delgado

2018

ABSTRACT OF THE DISSERTATION

Dynamic Shape-changing Hydrogels for Tissue Engineering

by

Stephanie Marie Delgado

Doctor of Philosophy in Bioengineering

University of California, Los Angeles, 2018

Professor Andrea M. Kasko, Chair

In embryogenesis and morphogenesis, cell clusters or sheets organize into units of increasing complexity from multi-cell layers, to tissues, organs and eventually whole organisms. Dynamic changes in shape are an essential part of morphogenesis and even the most complex biological structures are formed from fairly simple units through numerous shape transformation steps. Although nature has found ways to elegantly exploit shape transformation in plants and animals, the field is much newer to polymer scientists and engineers. Furthermore, tissue engineers are only starting to explore shape transformation for cell and tissue culture. Current shape changing scaffolds are not permissive of self-folding actuation at arbitrary time points nor are they permissive of step-wise folding, similar to what is observed during morphogenesis and development. The subject of this manuscript is on shape-changing photodegradable hydrogels for cell and tissue culture. We first discuss the physical basis for how light is used to pattern

differences in swelling throughout a hydrogel film. The differences in swelling are balanced by the hydrogel's network elasticity, resulting in folding of free-floating hydrogels. Beyond demonstrating shape-change as a proof of concept, we systematically review the effect of material, chemical, and physical parameters on curvature. Next, we discuss the use of planar sheet geometries and spatiotemporal light patterning to actuate hydrogel folding with different mean and Gaussian curvatures that are relevant for human biology. Finally, we demonstrate that the hydrogels are capable of supporting 2D seeded cell culture and 3D encapsulation. Mammalian cells on the hydrogel scaffolds are shape changed at arbitrary time points and remain viable. We thus demonstrate photodegradable hydrogel shape change as a viable concept for dynamic, 4D cell culture.

The dissertation of Stephanie Marie Delgado is approved.

Amy Catherine Rowat

Nabil J Tawil

Paul S Weiss

Gerard Chee Lai Wong

Andrea M. Kasko, Committee Chair

University of California, Los Angeles

2018

DEDICATION

This thesis is dedicated in loving memory of my grandmothers, Estrella Delgado Sion and Ana Mesa Penagos. Their appreciation for all things beautiful—including textile patterns, plants and nature—inspired my vision for this biologically inspired research.

I also dedicate this work to my parents who gifted my first microscope and nurtured my love for reading and free spirit.

Table of Contents

LIST OF FIGURES

LIST OF TABLES

LIST OF SYMBOLS

α_s	Linear elongation parameter
α_x	Respective bilayer thicknesses, x=1,2…
γ	Film or bilayer thickness
ε	Molar absorptivity
κ_{app}	Degradation rate constant
κ_0	Curvature
λ	Wavelength
ν_1	Solvent molar volume
v_{2m}	Polymer volume fraction at equilibrium
v_e	Effective number of polymer chains in a network
v_b	Intact strands (bottom half)
v_t	Intact strands (top half)
ρ	Radius of curvature
σ	Coefficient of expansion
φ	Quantum yield
χ_1	Flory-Huggins parameter
c	Speed of light
h	Planck's constant
p	Pitch
p_{rg}	Reverse gel point
r_b	Inner lumen radius
t	Time

t_c	Critical time to hydrogel erosion
w	Rectangular sheet width (short side)
w_b	Width of the bending region
w_s	Width of stretching region
z	Through depth position
C_b	Bottom (or opposite) side gel length after equilibration
C_t	Top (or exposed) side gel length after equilibration
E	Elastic modulus
G	Shear modulus
H	Mean curvature
I	Light irradiance
I_0	Incident light irradiance
J_0	Light dose
K	Gaussian curvature
L, L_0	Rectangular sheet length (long side)
L_f	Helix end-to-end distance
N	Number of turns in helix
N_A	Avogadro's number
Q_m	Equilibrium volume swelling ratio
Q_t	Volume swelling ratio (top half)
Q_b	Volume swelling ratio (bottom half)
R	Gas constant (8.314 $J \times mol^{-1} \times K^{-1}$)
T	Temperature

V_0 Volume of the unswollen (dry) polymer network

ACKNOWLEDGMENTS

There are countless people to thank for helpful discussions and motivational support throughout this rollercoaster of a journey. While I cannot name everyone here, I would like to give special thanks to key people involved in this thesis.

Kasko Lab

A special thanks to my PhD advisor, Andrea Kasko, who saw me through this (almost) 6 year evolution, originally suggested the photodegradable shape changing system idea and entrusted me to develop the project. I am forever grateful for your scientific insight, patience, and reminding me to trust my intuition. Thank you for assembling such a wonderful group of scientists and for instilling in me a love and appreciation for basic science research. With that, all members of the Kasko lab deserve an acknowledgment for their camaraderie throughout the years and making coming to lab so fun. I am sure we will continue to be life-long friends and dear colleagues. Of special note, Elli Käpylä, co-author on Käpylä et al.,[1] was instrumental in designing our first proof of concept experiments and the publication of our first paper on the topic. Sam Norris also participated in countless hours of discussion about almost any topic imaginable and helped develop a cell counting tool for the fluorescence-based viability assay, developed the photodegradation model (which we used to design our starting conditions for preliminary tests) and helped initiate the idea to study the different photodegradable macromers. Darice Wong also particularly helped with early discussions concerning experimental design. Changying Xue and Stephanie Deshayes supplied some of the photodegradable and PEG macromers and provided invaluable support on research

and life in general. Thomas Horn helped with image analysis and Justin Su wrote an image analysis code; both were immensely helpful.

Colleagues at UCLA, University of Miami, and University of New South Wales

Michael Hicks (April Pyle lab) helped with discussions and provided the human fetal muscle cells. Wen-Chin Huang (Song Li lab) kindly provided the human aorta endothelial cells. Kirsten Turlo also took the time to serve as a mentor on all things education, science, and life. I gratefully acknowledge my committee members, Amy Rowat, Bill Tawil, Paul Weiss, and Gerard Wong for their time and advice. A special asknowledgement is in effect to Gerard Wong for so eloquently introducing Polymer and Flory Theory. Finally, I extend a warm thanks to my undergraduate research advisors Fabrice Manns, Jean-Marie Parel, and Arthur Ho. Thank you for your constant encouragement and somehow seeding the crazy idea of pursuing a PhD in an unbelieving young Miami girl. I will remember my time at UCLA and the University of Miami with fondness and cherish the healthy and inspiring learning environment provided for students eager to learn like myself.

Family and friends

Last but not least, I want acknowledge all my wonderful and supportive family and dear friends that are like family. You inspire the best version of us and motivate my never-ending journey in search of truth. A special thanks to my parents (Hilda and Jaime Delgado), Sina Kalbasi, Amal Katrib, Vianica Moraguez, Angela Sanchez, Sarah Anassori, Dian Huang, and Elli Käpylä for your support at crucial times.

Funding support

I also gratefully acknowledge my funding support from the Eugene V. Cota-Robles Fellowship funded by the University of California Office of the President, the UCLA Graduate Division, and the UCLA Bioengineering Department as well as the Comprehensive Training in Neuroimaging Fundamentals and Applications (NIH/NIDA T90-DA022768). Furthermore, this work was largely supported by the National Institutes of Health through the NIH Director's New Innovator Award Program (1-DP2-OD008533). I also acknowledge the use of confocal microscope at the UCLA BSCRC Microscopy Core imaging facility at no cost to us.

Copyright Permissions

Finally, I gratefully acknowledge the use of material included in Chapters 3 and 5 from our publication from Ref. 1. Figure 2.1 was reproduced with permission from Ref. 2. Elements of Figure 2.2 were reproduced with permission from Ref. 3, 4 "Copyright 2008 National Academy of Sciences" and 5. Figure 2.3 was reproduced with permission from Ref. 6. Figure 2.4 was reproduced with permission from Ref. 7. Elements of Figure 4.14 were reproduced with permission from Ref. 8 and 9. Elements of Figure 4.17 were reproduced with permission from Ref. 10. Elements of Figure 4.18 were reproduced with permission from Ref. 9. Elements of Figure 4.19 were reproduced with permission from Ref. 11.

VITA

Education

Ph.D.	Bioengineering, University of California, Los Angeles Thesis: Dynamic Shape-changing Hydrogels for Tissue Engineering Advanced to candidacy: June 2016	Expected June 2018
M.S.	Bioengineering, University of California, Los Angeles GPA: 3.7	December 2014
B.S.	Biomedical Engineering, University of Miami, Coral Gables GPA: 3.8	May 2008

Experience

Graduate Research Assistant 2012-current

Biomaterials and Tissue Engineering (Kasko) Lab, UCLA, Los Angeles, CA

Develop stimuli responsive biomaterials for dynamic cell culture

Program Manager: Neurology Research Clinical Trials 2011-2012

Florida Hospital for Children- Center for Pediatric Research, Orlando, FL

Initiated new neurology clinical research center. Responsible for: serving as liaison between investigators, clinicians, engineers and regulatory staff, initiating first IND stem cell trial at new site and ensuring compliance with FDA, internal regulatory and funding agencies

Senior Research Associate 2010

Ophthalmic Biophysics Center at Bascom Palmer Eye Institute, Miami, FL

Worked with R&D team of mechanical, optical, biomedical and electrical engineers to develop ophthalmic autorefractor for intraoperative use

Research Fellow (Whitaker International Fellow) 2008-2009

Institute for Eye Research, Brien Holden Vision Institute, Sydney, NSW, Australia

Collaborated with multidisciplinary team of optometrists, engineers and clinical research scientists to complete human studies to measure far and near sighted peripheral vision as part of the largest anti-myopia initiative using non-surgical techniques

Undergraduate Research Assistant 2005-2008

Ophthalmic Biophysics Center at Bascom Palmer Eye Institute, Miami, FL

Assisted with ophthalmic animal surgeries and collaborated in planning international ophthalmic research conferences (Accommodation Club and KPro Study Group)

Student Lab Assistant 2004

Biomedical Optics and Laser Laboratory, University of Miami, Coral Gables, FL

Assisted lab manager on a project using laser interstitial thermal therapy for treatment of breast tumors

Teaching Experience

Teaching Assistant, UCLA Biomedical Research Minor 2017-2018

Biomedical Research: Essential Skills and Concepts (Topics: Genetics and cardiac tissue regeneration, Duchenne muscular dystrophy and skeletal muscle regeneration)

Teaching Assistant, UCLA Dept. of Bioengineering 2015-2016

Targeted Drug Delivery and Controlled Drug Release
Tissue Engineering

Publications

S. M. Delgado*, Kapyla, E.*, and A. M. Kasko (2016). ACS Appl Mater Interfaces **8**(28): 17885-17893. DOI: 10.1021/acsami.6b05527

Veerendranath, P., L. Donovan, M. Taneja, T. J. Naduvilath, Q. Garrett, **S. Delgado**, V. S. Sangwan and A. Ho (2014). Optom Vis Sci **91**(7): 752-759. DOI: 10.1097/OPX.0000000000000294

Whatham, A., F. Zimmermann, A. Martinez, **S. Delgado**, P. L. de la Jara, P. Sankaridurg and A. Ho (2009). J Vis **9**(3): 14 11-13. DOI: 10.1167/9.3.14

Conference Presentations

S.M. Delgado, E. Kapyla, A.M. Kasko, "Cell-Laden Hydrogel Assembly and Enzyme-Mediated Crosslinking." 18th UC Bioengineering Symposium, June 2017.

S.M. Delgado, A.M. Kasko, "Shape Changing Photodegradable Hydrogels for 2D to 3D Cell Culture." Society for Biomaterials, April 2017.

Chapter 1

INTRODUCTION

I. Shape transformation in nature

Shape-changing materials have recently attracted much interest in the scientific and engineering communities due to their applications in diverse areas including biology, electronics and semiconductors and robotics.[12-14] We use shape change, or shape transformation, to refer to the folding of planar materials in to 3D shapes upon exposure to an external stimulus. Shape transformation is actuated by inhomogeneities—either within the material or its surrounding medium.[12] We can gather inspiration for the creation of synthetic shape changing materials from nature, where shape transformation frequently occurs without a need for electrical power supplies or batteries.

Shape transformation in plants

Shape transformation occurs in plants in the absence of electrical or muscle actuators (these are more common in animals). Rather, plants undergo hydration-dependent changes in curvature,[15-17] making them attractive to study since their shape transformation does not rely on electrical stimulation. In plants, the change in hydration of a hygroscopic, hydrogel-like extracellular matrix, leads to swelling or shrinkage depending on environmental humidity.[18] Furthermore, the shape change direction depends on the alignment of cellulose fibrils, which are embedded in the surrounding extracellular matrix.[16] Anisotropies in the swelling state of the composite polymeric material generate curvature due to their elasticity. For example, rapid snap buckling is observed in plants, such as the Venus flytrap that can close in sub second times. Forterre et al. measured changes in leaf curvature between the open and closed states of the Venus

flytrap and suggested that the plant mediates the shape transformation both actively and passively in a series of closing phases.[19] They observed that large well-hydrated, and initially more curved leaves were more readily able to undergo complete snap-buckling closure compared to small and less curved leaves. Hayward and Santangelo and coworkers have studied similarly metastable curved synthetic polymer analogs that also undergo snap-buckling 3D shape transitions.[20,21] In another example of hydration-dependent shape change, Erb et al. take inspiration from shape transformation in seed dispersal units of plants and generate similar curvatures in synthetic analogs.[22] They demonstrate both bending and twisting of alumina-gelatin composites—akin to shape transformation events observed in pinecone and seedpod opening and closing. These examples demonstrate how shape change often occurs in plants and how we can take inspiration from nature to create synthetic analogs.

Morphogenesis and other shape transformations in animals

Shape transformation in animals occurs through a combination of passive and active electrochemical events. Much of what we know about shape change in animals is derived from developmental biology. Dynamic changes in shape are an essential part of morphogenesis and even the most complex biological structures are formed from fairly simple units through numerous transformation steps. For example, in the process of neurulation, the development of the vertebrate brain and spinal cord begins from the folding of the thickened neural plate leading to closure of the neural groove and formation of the neural tube.[23] The development of the four chambers of the heart also requires extensive shape transformation, beginning with the spreading and folding of the cardiac crescent leading to the fusion of the heart tube. The heart tube sequentially

elongates, and then undergoes looping and further growth, followed by septation of the chambers.[10,24]

A goal of tissue engineering is to recreate functional tissue analogs of organs, such as the heart. Although, the technology is not there yet for complex organs such as the human heart, significant progress is being made along different avenues. For example, Nawroth et al. took inspiration from shape transformation in animals and used a tissue engineering approach to recreate a partially synthetic analog of swimming jellyfish. Cardiomyocytes isolated from rat (active component) were patterned on silicone polymers (passive component).[25] They modulated material geometries and stiffness as well as cardiomyocte alignment to recover jellyfish-like stroking motions when the composite material was exposed to an electrical current in water. Similar mechanistic studies of animal movement and shape change can be applied to generate increasingly complex tissue engineered constructs.

II. Mimicking shape transformation in nature

Synthetic shape-changing materials

Timoshenko originally derived the theory of bilayer bending in 1925 for bilayer metal rods with different thermal expansion coefficients.[26] Although metals may be attractive for certain biomedical applications, such as surgical devices, polymeric materials are better suited for tissue engineering due to their more similar material properties to soft tissue. Engineering of shape changing polymeric materials is a newer field, with most research being done post 2000.[14,27,28] Gracias reviewed four general techniques for creating self-folding polymeric films, including: (1) fused bilayers (2) generating heterogeneities in crosslinking along the lateral dimensions of a film (3)

generating heterogeneities in crosslinking along a film's thickness (4) releasing a pre-strained film from a substrate.[14]

Bilayers are among the simplest shape changing systems and conversely among the most commonly reported. They are typically fabricated by sequential deposition of UV-crosslinked polymers with different swelling properties. An early study demonstrating shape change on hydrogels in the presence of mammalian cells did so using polyethylene glycol (PEG) bilayers with different molecular weights. Cells were encapsulated in the layer with higher molecular weight PEG and the gels were swollen in cell medium, thus generating folded structures.[7] Since then, others have reported similar bilayer technologies for shape changing cell-laden hydrogel scaffolds.[29]

Successes and limitations of current research

Despite being a young field of research, design of polymeric shape-changing systems has garnered significant interest from diverse disciplines.[28,30] The incorporation of living cells in polymeric materials for tissue engineered applications is still much more limited. However, proof of concept studies demonstrate that cells cultured on scaffolds can be folded from planar sheets to 3D folded structures while maintaining cell viability.[7,29,31,32] Less is known about what effects the shape transformation has on bioactivity. In order to determine the effect of shape transformation on bioactivity, the timing of shape transformation should ideally be controlled in order to study cell response before and after (or with and without) shape transformation with otherwise constant conditions.

A limitation of prior cell culture systems is that they were typically pre-fabricated with the inhomogeneities that generate shape change. Thus, folding happens immediately upon introduction to water or cell culture media. Therefore, there is limited to no control

over the timing of shape transformation. However, during morphogenesis and development, the sequential timing of shape change and folding events is critical to the final form and function of the tissue.[33,34] Previously reported shape change systems for cell culture do not have the flexibility to permit user-defined shape change timing and as such cannot mimic the sequential timing of shape change events observed during morphogenesis.

Other shape changing cell culture scaffolds that use thermally responsive materials like poly(*N*-isopropylacrylamide) (pNIPAM) to initiate shape transformation in the presence of cells have been reported.[35] However, while stimuli responsive materials, like pNIPAM, can be used to generate reversible folding, the conditions must be suitable for cell culture. Since mammalian cells require specific temperature, pH and ionic strength, these stimuli that are commonly used for actuating polymeric shape change are not readily suitable for initiating shape change at arbitrary time points in the presence of cells. In order to study the time dependent effect of shape transformation on cell bioactivity, alternate approaches are required.

III. Dissertation focus

Overview

The aim of this dissertation is to introduce and to develop photodegradation as a tool for actuating shape change in pre-equilibrated hydrogels for tissue engineering. We use a class of hydrogels containing *ortho*-nitrobenzyl (*o*-NB) moieties, previously reported to support 2D and 3D cell culture.[36,37] The hydrogels degrade when exposed to long-wave UV light, in a spatiotemporal manner.

Previous research has been done to demonstrate different synthetic shape-transformation materials and actuation stimuli, largely influenced by mechanisms observed in nature. Polymers are generally responsible for shape transformation in nature due to their prevalence in living organisms and their ability to undergo large volume changes in response to several stimuli. Polymers are also commonly used for cell culture. However, shape-change actuation in the presence of cells requires that not only the material, but also the stimulus not be harmful to cells. This constraint has largely limited shape change in the presence of cells to shape changing scaffolds with pre-fabricated inhomogeneities that folded upon dissolution of an underlying attached substrate in water or cell culture medium. Therefore, the goal of this dissertation is to demonstrate photodegradable hydrogel shape change as a viable concept for dynamic, or 4D cell culture.

Significance

This dissertation presents results on the first cell culture scaffold that permits shape change in the presence of cells at arbitrary, user-defined time points. Prior approaches do not allow for user-defined shape-change actuation. We developed light-actuated shape-changing hydrogels with appreciation for the spatiotemporal significance of timed shape-change events during morphogenesis and development. We hope that the photodegradable shape-changing hydrogels presented in this dissertation will be used to study the effect of changes in curvature and strain-induced stretching and bending on cell response. Furthermore, we introduce a framework for generating different mean and Gaussian curvatures in the same photodegradable materials in an effort to demonstrate a variety of 3D shapes that can be generated from initially planar equilibrated sheets. We

expect these shapes to be of relevance for recapitulating curvatures seen in morphogenesis and development as well.

Outline of chapters

We first describe the conceptualization of UV-photodegradation actuated self-folding hydrogels in Chapter 3. Furthermore, we explore variables affecting folding curvature by varying material, chemical and physical properties. In Chapter 4, we demonstrate generation of arbitrary curvatures within the same photodegradable material in an effort to recapitulate curvatures observed during embryogenesis and in adults. The ability to shape change hydrogels in the presence of mammalian cells is discussed in Chapter 5. Finally, in Chapter 6, we discuss dissertation conclusions and future directions.

Chapter 2

BACKGROUND

I. Hydrogels

Hydrogels are water-swollen cross-linked polymer networks. They are ideal soft tissue culture scaffolds given their similarities to the extracellular matrix—the non-cellular component of tissue[38] that are largely responsible for its shape. Extracellular matrix (ECM) is composed of proteins and polysaccharides, called glycosaminoglycans, which are often covalently linked to proteins forming what are termed proteoglycans.[39] These protein and polysaccharide complexes form water-swollen networks surrounding tissue resident cells, often occupying more space than the cells. Once believed to exclusively play a passive role in giving tissues their physical structure, the ECM is emerging as a dynamic and active regulator of cellular behaviors including cell growth, differentiation, morphogenesis and regeneration. Rozario and DeSimone review the ECM's role in providing binding sites, regulating growth factor signaling, as well as in sensing and transducing mechanical signals.[40] Due to the ECM's involvement as a structural component of tissue, as well as its role in regulating cell behavior, research in tissue engineering and regenerative medicine has focused attention towards its recapitulation for cell and tissue culture applications.

Given their water-swollen nature and tunable mechanical and chemical properties, hydrogels have garnered interest as extracellular matrix analogs for cell culture.[41] A primary advantage of using hydrogels for cell culture over hard tissue culture plastic derives from their tunable mechanical and chemical properties. Hydrogels can be

fabricated from natural or synthetic hydrophilic polymers to desired specifications. Naturally derived hydrogels have the advantage of containing native bioactive components such as the ubiquitous RGD binding domain first discovered in fibronectin[42] and later found in other adhesive extracellular proteins[43] and/or matrix metalloproteinase (MMP) degradable sites.[44] However, a disadvantage of naturally derived molecules is their variability from batch to next and their often ill-defined nature.[45,46] Alternatively, synthetic hydrogels can be well characterized and more reproducible, yet they lack bioactive components. Scientists have thus developed strategies for incorporating bioactive components in synthetic hydrogels to promote adhesion and cell spreading,[47,48] MMP degradable sites[49], as well as other critical factors for tissue morphogenesis and maintenance.[46,50] Furthermore, Flory,[51] deGennes,[52] Peppas,[53,54] and Brannon-Peppas and coworkers[55] have established a framework of governing equations for estimating hydrogel mechanical properties based on their molecular weight, mesh size and volume swelling ratios. The rapidly increasing interest in development of hydrogel chemistries, characterization techniques and rational engineering design has spurred a series of several excellent, review articles.[54,56,57] Furthermore, a variety of hydrogel technologies now provide a toolbox with which to probe in vitro questions that could not be accessed by traditional 2D culture on tissue culture plastic.

II. Mechanical and biochemical signals in biology and how their temporal-spatial presentation affects tissue development

It is not surprising that scientists have started to uncover in vitro cell behaviors using hydrogels that could not be studied using traditional cell culture techniques. For example, the seminal paper by Bissell and coworkers demonstrated that mammary

epithelial cells cultured in 3D environments were capable of forming multicellular colonies with central lumen that produced collagen—much like mammary epithelial cells form acini in vivo—whereas the same cells cultured on 2D substrates, spread into monolayers that did not resemble physiological phenotypes.[58] These findings highlight the importance of culturing cells in a native 3D ECM-like presentation for reproducing physiological conditions. However, even 2D culture on hydrogels has led to important discoveries regarding cell function as a result of the microenvironment. For example, Disher and coworkers demonstrated that adult stem cells cultured on substrates with a range of stiffnesses differentiated into different phenotypes.[59] The finding that stem cells cultured on soft (< 1 kPa), intermediate (8-17 kPa) or stiff (25-40 kPa) substrates led to differentiation down neuronal, muscle or osteogenic lineages respectively, paved the way for subsequent research towards engineering substrates of matched mechanical stiffness for cell and tissue culture.[60-62]

Although less is understood about dynamic and spatially dependent processes, the significance of ECM molecules' role in tissue development (morphogenesis) and regeneration is receiving increasing attention from researchers. For example, the heart condition, cardia bifida, results in the formation of two hearts when developing myocardial precursor cells fail to meet at the midline and fuse to form the heart tube during early development. Studies done in mice[63] and zebrafish[64] showed that fibronectin mutations could lead to the pathogenic phenotype. In zebrafish, when fibronectin was absent, the heart tube failed to fuse. However, when fibronectin was only absent at the midline and not at the lateral edges, myocardial precursor cells had delayed migration towards the midline. They did, however, eventually reach the midline

and form a heart tube with abnormal morphology.[2] These experiments demonstrate that fibronectin at the midline affects the timing of myocardial migration, yet is not required for migration and fusion. Furthermore, it highlights the significance of both temporally and spatially controlled processes during embryogenesis.

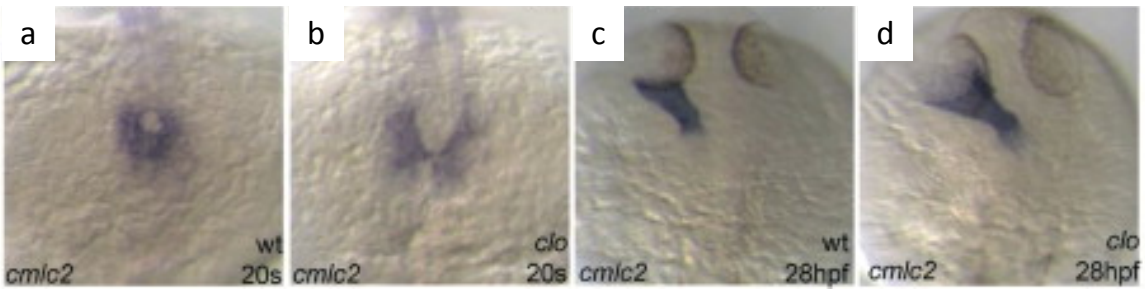

Figure 2.1. Effect of fibronectin absence at midline on cardiomyocyte migration and fusion to form heart tube in zebrafish. In (a) and (c), wildtype cardiomyoctyes (cmlc2) fuse at the midline at 20 seconds and form linear heart tube at 28 hours post fertilization respectively. When fibronectin is absent at the midline (c/o mutant), there is delayed fusion (b) however, the cardiomyocytes eventually fuse and form a dilated heart tube (d). The image was reproduced with permission from Ref. 2.

Knowledge from developmental biology can be used to guide design of regenerative medicine strategies.[65,66] For example, skin wound healing in the developing mouse embryo is scar-free during the first 16 days of gestation.[67] This capability is in contrast to healing in the adult mammal or at later gestational stages, which is characterized by an inflammatory response and scar formation.[68,69] Fetal skin regeneration is instead characterized by faster collagen deposition[68] and high hyaluronic acid content compared to adults.[70,71] Furthermore, although hypoxic conditions correlate with poor wound healing in the adult, hypoxemic conditions in the fetus do not deter efficient wound healing. Our developing understanding of wound healing in the fetus is instructing design of wound healing and regenerative medicine for adults—for example there are now several hyaluronic acid products on the market to treat wrinkles in aging skin as well as for wound dressings.[72,73] Still, our understanding of developmental biology is mostly instructed by molecular mechanisms (e.g., using knock-out and over-

expression of target molecules as well as determining the presence/absence of molecules). Less is understood about dynamic and multi-faceted physical factors such as the effect of mechanics on changes in gene expression. This limitation suggests why, even with the mapping of the human genome,[74,75] there is yet a paucity of understanding of many diseases, including congenital disorders.

Part of the problem is that we lack tools for studying dynamic processes in vitro. This type of research is mostly carried out in animal models due to a lack of representative human tissue models. Experimental developmental biology is carried out in animal models such as nematode worm, drosophila, zebrafish, chick and mouse. Experiments in animal models have informed our understanding of important processes, such as heart and gut development. For example, Tabin and coworkers found that gut tube rotation is controlled by changes in the attached dorsal mesentery.[3,4,8] Tissue folding in developing vertebrates often occurs due to strain in an epithelial layer and underlying ECM. In the case of the gut tube, its sole connection to the body wall via the dorsal mesentery, led researchers to look towards the dorsal mesentery to explain its rotation. Theories that packing constraints of the growing gut tube in the body cavity cause the looping morphology were disproved in chick through surgical dissection of the gut tube attached to the dorsal mesentery from the body cavity. The looping morphology was retained once the gut tube and dorsal mesentery were released, disproving the constrained body cavity volume theory.[5] Other studies done in chick showed that changes in mesenchymal and epithelial cell architecture on the left and right sides of the dorsal mesentery are regulated by left-right asymmetries of transcription factors, Pitx2 and Isl1, in the developing gut. Misexpression of the genes, leading to homogenous

spatial presentation of Pitx2 or Isl1, prevents asymmetries in the mesentery and limits tilting of the attached gut tube (Figure 2.2). Both a more compacted mesenchyme and columnar epithelial cells on both sides (left and right) of the dorsal mesentery resulted from homogeneous expression of Pitx2 and Isl1 and were sufficient to establish limited tilting of gut tube in chick mutants.[3] Computer simulations that looked at the effect of changes in cell-cell adhesion and cell shape in both the epithelium and the mesenchyme of the dorsal mesentery as well as ECM swelling also support results in the chick model.[4] Importantly, the computer simulations support the Pitx2/Isl1 misexpression results, and tell us how to enhance, or modulate, gut tilting using the ECM. Changes in ECM swelling and stiffness (under certain conditions) enhanced gut tilting compared to differences in cell-cell adhesion caused by Pitx2/Isl1 asymmetries alone. Computer simulations were supported by immunostaining of chick embryos for N-cadherin, Pitx2, Isl1 and ECM molecules—glucosaminoglycans (GAGs) and hyaluronic acid. Interestingly, they found that misexpression of N-cadherin on the right side of the dorsal mesentery led to accumulation of GAGs (Figure 2.2) and reduced hyaluronic acid but it did not affect Pitx2 mRNA expression. These results demonstrate that N-cadherin—upregulated by Pitx2 and Isl1—not only regulates cell-cell adhesion but also affects the ECM composition. In wild type, the resulting compaction of the mesentery and change in epithelium morphology from cuboidal to columnar on the left side, along with increased volume on the right leads to primary tilting of the gut tube towards the left. The primary gut tube rotation orientation has downstream effects on the subsequent rotation directions.[3] These in vivo, in silico, and ex vivo findings were further supported by experiments using a purely synthetic model. Savin et al. used a rubber tube to mimic

the gut tube and a latex sheet to mimic the mesentery. Stretching the latex sheet along its length as it is adhered to the initially straight, unstrained rubber tube results in looping reminiscent of gut tube looping (Figure 2.2). They demonstrate that modulation of the differential strain, modulus of the respective sheet and tube components, tube diameter and sheet thickness affected the looping patterns. These parameters could be modeled using simple scaling laws to predict the looping pattern pitch and radius. Furthermore, experimentally determined biophysical measurements of different avian species and mouse were used to verify agreement with the theoretical and physical model.[5] However, even with this in-depth physical and molecular-level understanding, gut tube malrotation is still the most common congenital disease affecting the small intestine. It is believed to produce symptoms in 1 in 6000 births.[76] And while research in model organisms traditionally precedes treatments in the clinic, species differences often lead to unpredicted failed treatments when transitioning from the animal model to humans.

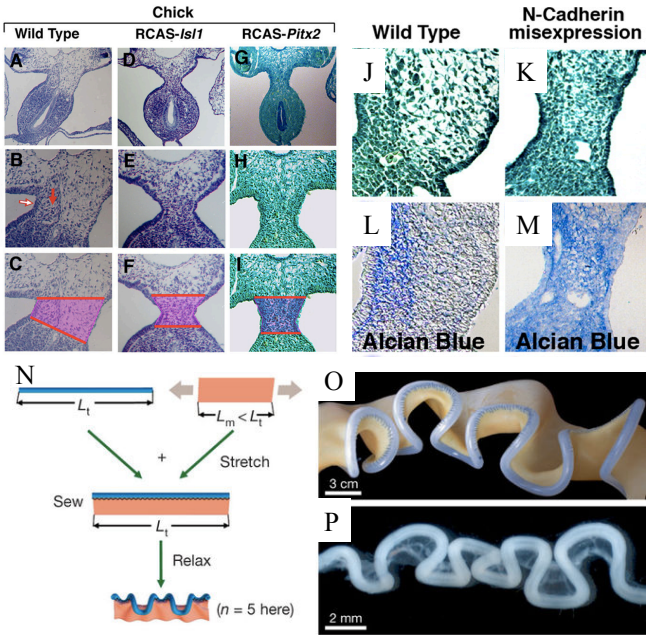

Figure 2.2 Gut tube rotation due to left-right asymmetries in attached dorsal mesentery. (A-I) on the left are histology cross-sections of midgut from chick and were reproduced with permission from Ref. 3. (A-C) are from wild-type, (D-F) are following misexpression of Isl1 and (G-I) are following misexpression of Pitx2. Image (J-M) are histological cross-sections of the dorsal mesentery from the midgut that were modified and reproduced from Ref. 4 "Copyright 2008 National Academy of Sciences". (J and L) are from wild type. In (J) stains for N-cadherin and (L) stains for acidic GAGs show left-right asymmetries. Misexpression of N-cadherin in (K) and (M) show homogeneous expression of N-cadherin in (K) and increased GAGs in (M). (N-P) are reproduced with permission from Ref. 5. (N) is a schematic representation of how the physical model of looping was assembled using a rubber tube and sheet. In (O), the attached tube and sheet are released and fold in to looping structure that looks similar to looping in the chick gut at E12 in (P).

The results from Tabin and co-workers both elucidate mechanisms that initiate gut looping direction and give a physical framework for determining looping patterns given specific biophysical parameters of the gut tube and dorsal mesentery. Less is known about what effect(s), changes in tissue shape have on genetic/protein level expression. In one example, Shyer et al. demonstrate that tissue shape, and curvature, affects molecular expression that localizes intestinal stem cells at the base of villi and not at the peaks (Figure 2.3).[6] This study draws attention towards the poorly studied concept of how physical changes guide cell behavior in vitro. While we have a better understanding of morphogenetic changes downstream of molecular level changes, much less is known about the reverse effect. Tabin et al. demonstrated parameters affecting gut rotation and looping using in vivo, ex vivo, computational as well as purely synthetic models. Yet, access to tissue engineered in vitro tools for studying the effect of changes in shape and ECM remodeling on cell biology is much more limited. These effects are challenging to study in vivo and impossible to study in purely synthetic models or ex vivo due to the requirement of studying the cellular response to a physical perturbation. This is where hydrogels that have volumetric shapes that are (i) sensitive to changes in swelling and elasticity, and (ii) can be remodeled by cells, may offer a vehicle for studying a largely untouched field.

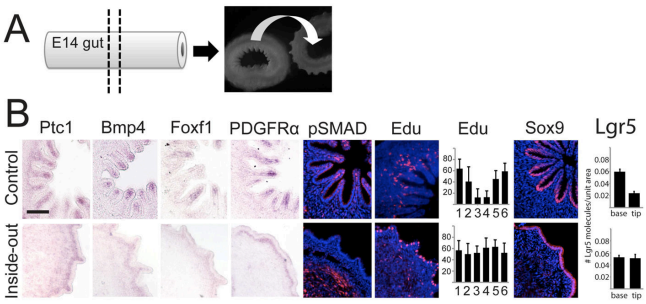

Figure 2.3 Effect of villi curvature on stem cell localization in intestine. Embryonic gut tube excised at E14 and cultured for 36 h in original shape (control) or inside out so villi are stretched and lining outside of tube. Villus cluster probes were concentrated at villus tips and proliferation and stem markers limited to villi base for controls. Instead, inside out sections stained for villus cluster probes at low intensities and more diffusely. Proliferation and stemness markers were not restricted from the villi tips as they are under physiologic conditions. Image reproduced with permission from Ref. 6.

Gartner and co-workers elegantly demonstrated the use of a functionally relevant hydrogel substrate made of ECM molecules for engineering tissue folding.[32] They seeded fibroblasts in pre-calculated patterns (determined using finite element modeling) on Matrigel substrates. The fibroblasts compacted the ECM and laid down aligned collagen fibers. As a result, patterned substrates resulted in the formation of large scale coiling, tubular and spherical folding of millimeter scale substrates. Their study demonstrates that mesenchymal cells alone are capable of compacting overlying ECM to generate predictable folding patterns that are biologically relevant for morphogenesis. Importantly, they highlight a tissue-engineered model that can be used to study shape-change in the presence of cells. This model intriguingly demonstrates how mesenchymal cells alone are capable of remodeling an overlying substrate to initiate shape-change events. However, using cells to actuate shape-change does not allow us to decouple the effect of shape-change on cell biology. Since the cells participate in generating the shape-change event, it is difficult to determine whether any measured changes in molecular level expression resulted from or was caused by the shape-change. In order to decouple the effects, actuation of shape-change, or changes in scaffold architecture, should occur independently of the patterned cells. Here, we suggest that shape-changing hydrogels can offer a substrate with which to culture cells on and actuate folding events for studying the effect of physical forces on cell behaviors as well as for creating 3D cell-laden folded shapes.

III. Nature inspired dynamic control over hydrogel chemical-physical properties

We drew inspiration for shape-changing hydrogels from examples in living organisms. Folding generally occurs due to mismatched strain at a material interface. If

the materials are elastic, and not brittle, folding will occur to balance the mismatched actuation strain. For example, plant leaves and seed dispersal units (like pine cones and seed pods) are composed of copolymers of relatively rigid and aligned cellulose fibers embedded in flexible tissue. Due to differences in swelling and the alignment direction of the fibers, they fold in response to humidity levels.[22,77] Similarly, the ability of a jellyfish to generate stroking motion is due to a combination of rigid myofibrils embedded in a soft hydrogel matrix.[25]

Polymeric materials, and hydrogels in particular, are well-suited for self-folding applications because they undergo pronounced volume changes in response to a variety of stimuli such as pH,[78-80] temperature[20,81-83] and light.[84-86] Interpenetrating networks have also been used to actuate controlled folding in response to several stimuli.[87,88] Inspired by nature, Lewis and co-workers reported a hydrogel ink composed of cellulose fibrils embedded in a soft hydrogel acrylamide matrix for the 4D printing of complex self-folding shapes.[89] This technique was used to print biomimetic self-folding structures with predictive control over mean and Gaussian curvature. Others used similar biomimetic approaches of embedding cellulose nanocomposites in a rubbery matrix to generate stimuli responsive materials with reversible, large changes in stiffness.[90,91] However, the compatibility of this method for cell culture has not yet been demonstrated.

Self-folding hydrogel films can be used to generate cell-friendly structures with 3D complexity at multiple length scales, which is difficult to achieve with printing or lithography alone.[12] Shape-changing material systems are most commonly generated using hydrogel bilayers that are fabricated by sequential deposition and UV crosslinking of polymers with different swelling properties. These bilayer designs are often combined

with stimuli responsive materials, such as poly(*N*-isopropylacrylamide) (pNIPAM), to generate reversible shape-change in response to thermal actuation. PNIPAM is a temperature responsive material with a lower critical solution temperature (LCST) that can be tuned close to physiological temperature.[92] Thin pNIPAM films can be designed to reversibly swell and fold or relax and flatten at temperatures below or above the LCST respectively.[93] Several groups reported pNIPAM-based shape-change systems for biological applications. Ionov and co-workers reported the use of pNIPAM and polycaprolactone bilayers for the reversible encapsulation of yeast cells.[94] In another approach, Hayward and co-workers used RGD-functionalized pNIPAM gels patterned with surface creases. The gels were used to induce thermally reversible encapsulation of seeded porcine epithelial cells[35] or to apply tensile strain on seeded C2C12 cells.[95] These pNIPAM based systems are applicable for studying cell behavior only over short time scales since the actuation temperatures are at least 10°C below the standard mammalian cell culture temperature of 37 °C. Ionov[96] and Sitti[29] also reported gelatin based shape-change systems that fold in response to a thermal actuation. Both groups make use of gelatin's solubility in aqueous solutions at 37 °C to actuate changes in curvature of bilayers at 37 °C. Although this temperature is well suited for cell culture, it also dictates that the folding event must occur immediately, or soon after, mammalian cell seeding. In other words, these systems are not suitable for actuating shape-change at arbitrary time points from the cell seeding time.

Self-folding without the need for a change in temperature is more suitable for dynamic cell culture applications. Gracias and co-workers were the first to report this type of shape-change in the presence of mammalian cells using poly(ethylene glycol)

diacrylate (PEGDA) bilayers of different molecular weights. The differences in crosslink density generated different strains between the layers due to their differences in swelling. The bilayer system was shown to be compatible with cell encapsulation (Figure 2.4).[7,31] However, a general drawback of a bilayer systems is the sequential fabrication process in which sufficient adhesion between different layers needs to be ensured in order to avoid delamination during swelling and folding. Furthermore, the heterogeneities that generate folding are built in to the bilayers during the fabrication process. This means that the folding from a planar sheet to a 3D structure, again, can only be induced immediately after fabrication, during equilibration in water. This is also true for systems in which thin film folding occurs upon release from a water-soluble sacrificial layer.[97]

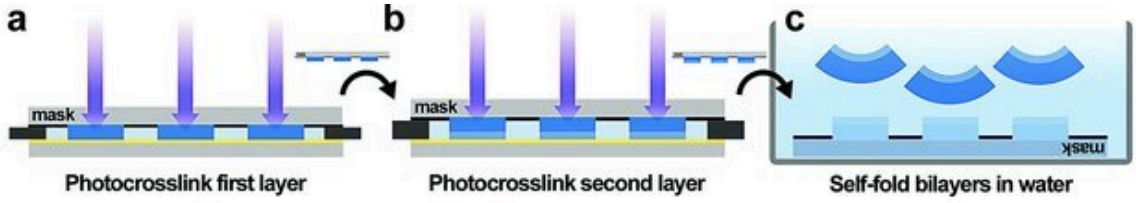

Figure 2.4 Schematic representation of PEG bilayer shape changing hydrogels. The bilayers, prepared with different molecular weight PEGs, undergo differential swelling and fold upon being placed in water. Image reproduced with permission from Ref. 7.

IV. Using light to control dynamic hydrogel properties

Although self-folding systems are used to create increasingly complex 3D shapes, most systems are either not cell compatible or are pre-engineered with heterogeneities that generate immediate folding upon equilibration in solution. Thus, previously reported shape-changing materials cannot be dynamically transformed from flat sheets to folded structures in the presence of cells at a user-defined time point. To address this, we looked to photoresponsive hydrogels. Light controlled chemical reactions have several benefits. One advantage of using light controlled reactions is that light can be guided to specific spatial directions at user defined time points. Furthermore, similar to small molecule or

biologics administration, light dose can be tuned in order to modulate the desired response. Finally, the wavelength can often be tuned to control orthogonal processes. These points are all reviewed in Ruskowitz and DeForest, 2018.[98]

Several biologically compatible photochemistries are also discussed in the Ruskowitz review. Nitrobenzyl functional groups are of particular interest due to their long history for biological applications[99] and demonstrated incorporation in to biocompatible hydrogel matrices for photouncaging.[36] In their seminal paper, Anseth and coworkers demonstrate the conjugation of an acrylated *ortho*-nitrobenzyl (*o*-NB) moiety to a PEG backbone. The acrylate functionality is conjugated to the photolabile *o*-NB moiety such that upon exposure to long-wave UV light, it is "uncaged". The acrylate functionality is also used to polymerize a growing kinetic chain using radical initiated hydrogel polymerization. In this way, a hydrogel is polymerized from the acrylate functional groups and at a user-defined time point, the linkages are degraded upon exposure to UV light.[36] They demonstrate degradation of the hydrogel using either single photon UV light or near IR multiphoton light.

Since the introduction of photodegradable *o*-NB hydrogels by Anseth and co-workers, a library of *o*-NB molecules with differences in reactivity at different wavelengths was reported for spatially controlled release of encapsulated hMSCs from hydrogels.[37] Characterization of the *o*-NB macromers' photoreactivity (rate constants of degradation, quantum yields and molar extinction coefficients) at several wavelengths—365, 405 and 436 nm—also led to the development of a computational model predicting the ratio of pendant chains as a function of time and depth (through the hydrogel).[100] Furthermore, *o*-NB photodegradable hydrogels were used to create swelling-induced

surface patterns at different wavelengths.[11] Xue et al. demonstrated that differences in attenuation coefficients at 365 and 405 nm could be used to generate unique surface features that are unlike the photomask used for patterning. So-called basket weave patterns were formed, after sequential patterning of square grid photomasks arranged offset from each other, only under specific wavelength and light dose patterning conditions. They postulate that the ratio of the 2D square pattern size, relative to the depth of degradation—a function of the light dose and wavelength dependent attenuation coefficient—is responsible for the unique pattern formation. That is, when the degradation depth was high compared to the 2D square photomask pattern size, basket weave patterns appeared, but when the degradation depth was low compared to the 2D square size, the more familiar square patterns were transferred to the hydrogel. Because the attenuation coefficient is higher at 365 nm compared to 405 nm, the basket weave patterns were generated for larger squares using 405 nm than was possible at 365 nm. These results are supported by the attenuation coefficient parameters determined by Griffin et al.[37] Furthermore, they suggest that the *o*-NB macromer used for the study attenuates UV light, generating differences in crosslink density, and thus swelling, which are limited to the gel surface. As a result, we hypothesized that attenuation of high UV light doses through the depth of an optically thick photodegradable *o*-NB hydrogel would similarly generate differences in crosslink density—resulting in differences in swelling through the hydrogel depth—that could generate folding due to the mismatched actuation strains.

V. Scope of work

The subject of this manuscript is thus on shape changing photodegradable hydrogels for cell and tissue culture. We first discuss the physical basis for how the differences in swelling throughout a partially degraded hydrogel film are balanced by the network elasticity. In the case of free hydrogels (i.e., not attached to a substrate) the differences in swelling induced actuation strain result in folding. Beyond demonstrating shape-change as a proof of concept, we systematically review the effect of material, chemical and physical parameters on curvature. Next, we discuss the actuation of different folding directions in order to generate hydrogels with curvatures that are relevant for human biology. Finally, we demonstrate that the hydrogels are not only capable of supporting either 2D seeded cell culture and 3D encapsulation, but that the cell-laden gels can be shape-changed at arbitrary time points.

Chapter 3

Synthesis and post-polymerization photopatterning of shape-changing hydrogel films

I. Theory: Crosslink density gradient generates swelling gradient and folding in thin films post-polymerization

Light attenuation used to generate gradient

Self-folding polymer and hydrogel thin films have been used to create increasingly complex 3D shapes, yet most systems are either not cell compatible or are pre-engineered with heterogeneities that cause folding immediately upon release from a substrate or upon equilibration in aqueous solvent. Thus, shape-changing materials cannot currently be dynamically transformed from flat sheets to folded structures in the presence of cells, on demand, at a user-defined time point. To address this limitation, we designed a photodegradable shape-changing system based on *ortho*-nitrobenzyl (*o*-NB) moieties incorporated into a PEG macromer. This type of hydrogel was first developed by Anseth and coworkers[36] and has previously been used in our group to create swelling-induced surface patterns.[11] Photodegradable hydrogels, such as the library of *ortho*-nitrobenzyl conjugated PEG hydrogels reported by Kasko and colleagues can be degraded post-gelation using long-wave UV to visible light (365-405 nm).[37]

Unlike bilayers with different swelling characteristics in each layer, or thin films with crosslink density heterogeneities introduced during polymerization, photodegradable hydrogel films are synthesized such that the initial post-gelation crosslink density is homogenous. With these starting conditions there is isotropic swelling and the film remains flat with no external stimulus. The crosslink density can be tuned post-

polymerization by conjugating pendant acrylates (or other polymerization branch points) to photolabile *o*-NB moieties (Figure 3.1). The acrylate groups are used to polymerize the hydrogel network kinetic chain using a radical initiator. At a user-defined time point, the photodegradable hydrogel films are exposed to UV light, at which point the crosslinks begin to degrade. The degradation rate is a product of the molar absorptivity and quantum yield of the photolabile moiety and is equal to

$$k_{app} = \frac{\varphi \varepsilon \lambda I_0 (2.303 \times 10^{-6})}{N_A h c} \qquad \textbf{(1)}$$

where φ is the quantum yield, ε is molar absorptivity, λ is wavelength, I_0 is incident light intensity, N_A is Avogadro's number, h is Planck's constant and c is the speed of light. Light is attenuated through the film depth as a function of incident light intensity and molar absorbance. The attenuation of light is described by the Beer–Lambert law in which the intensity of light $I(z,t)$ at a given position z and time t is expressed as

$$I(z,t) = I_0 exp\left[-\sum \varepsilon_j \int_z^\infty c_j(z',t)dz'\right] \quad \textbf{(2)}$$

The concentration and molar absorptivity of the j^{th} photoabsorbing species are denoted by c_j and ε_j, respectively. Therefore, for optically thick hydrogel films, at a certain depth normal to the side of light incidence, depending on the light dose and concentration of absorbing species, light is attenuated sufficiently so that there is no degradation and the crosslinks remain intact. This creates degraded and non-degraded regions through the thickness of the gel translating to a crosslink density gradient.

Difference in swelling balanced by elasticity of network

In the absence of an external stimulus, a homogenous hydrogel swells until it equilibrates with the surrounding solution. The agreement between the entropic free

energy of mixing of polymer and solvent and the elastic free energy for crosslinked polymer networks, such as hydrogels, has been described by Flory:[51]

$$-[\ln(1-v_{2m})+v_{2m}+\chi_1 v_{2m}^2]=\mathrm{v}_1(v_e/V_0)(v_{2m}^{1/3}-v_{2m}/2) \qquad \textbf{(3)}$$

where v_{2m} is the polymer volume fraction at equilibrium, which can also be represented as $1/Q_m$ where Q_m is the equilibrium volume swelling ratio, χ_1 represents the Flory-Huggins parameter, v_1 is the solvent molar volume, v_e is the effective number of polymer chains in a network and V_0 is the volume of the unswollen (dry) polymer network. The terms on the left of the equation account for mixing/entropic parameters and the terms on the right account for the elastic free energy. If we substitute v_{2m} with $1/Q_m$ and consider the case of highly swollen hydrogels (i.e. when $Q_m > 10$) equation **(3)** can be rewritten as

$$Q_m^{5/3} \cong (V_0/v_e)(\tfrac{1}{2}-\chi_1)/\mathrm{v}_1 \qquad \textbf{(4)}$$

Furthermore, the shear modulus, G, is related to the effective number of polymer chains by:

$$G=\frac{RTv_e}{V} \qquad \textbf{(5)}$$

where R is the gas constant (8.314 $\mathrm{J\times mol^{-1}\times K^{-1}}$) and T is temperature.

Combining equations (**(4)**) and **(5)** we arrive at:

$$G \cong RT(\tfrac{1}{2}-\chi_1)/\mathrm{v}_1 Q_m^{5/3} \qquad \textbf{(6)}$$

Of note is the inverse relationship between modulus and the five-thirds power volume swelling ratio.

Equations **(4)** and **(6)** describe how volume swelling and modulus vary as a function of elastically active polymer chains and polymer volume fraction. However, they do not describe the resulting shape deformation due to volumetric inhomogeneities

in crosslink density. The crosslink density difference through the film depth translates to a difference in volumetric swelling and modulus. The less cross-linked, degraded regions have increased swelling and decreased modulus, while the more cross-linked and less or non- degraded regions resist the entropy driven volumetric expansion by pulling on the network. In spite of degradation, the hydrogel network remains covalently bound as long as there are enough non-degradable crosslinks to prevent de-gelation. As such, an equilibrium strain is eventually reached that balances the entropic and elastic energies. In the case of a freely swelling gel, (i.e. not constrained to a substrate) this results in folding. The bending or folding of inhomogenous materials has long been known. Timoshenko first described the bending of a metal bilayer with two different thermal expansion coefficients in 1925. The difference in modulus of the metal bilayers resulted in uniaxial folding with a uniform curvature:

$$\frac{1}{\rho} = \frac{6(\sigma_2-\sigma_1)(1+m)^2}{\gamma(3(1-m)^2+(1+mn)(m^2+\frac{1}{mn}))} \quad \textbf{(7)}$$

$$n = \frac{E_1}{E_2} \quad \textbf{(8)}$$

$$m = \frac{\alpha_1}{\alpha_2} \quad \textbf{(9)}$$

where E_x are the elastic modulus terms, α_x are the respective layer thicknesses, γ is total thickness, σ is coefficient of expansion for each layer and ρ is radius of curvature.[26] In this case, the differences in elastic modulus described by the ratio, n, have little effect on radius of curvature. Instead, radius of curvature is affected most by the differences in actuation strain (for the case of hydrogels, this would be due to differences in swelling ratio) and the respective layer thicknesses. The Timoshenko equations have been adapted and used to describe folding for hydrogel bilayers.[89] Of note, important limitations of the equation as it pertains to our system are that (i) it describes a bilayer system, while our

system has a continuous crosslink density gradient formed from a previously swollen-equilibrated network and (ii) it describes uniaxial bending of rods as opposed to freely swelling sheets in both length and width axes. We will further discuss the second point as it pertains to folding geometries in Chapter 4. Here, we can use the Timoshenko equation as a starting point to understand what variables affect folding in the photodegradable hydrogel system. In this system, the actuation strain is due to the difference in crosslink density through the film depth that gives rise to differences in swelling immediately after degradation and mixing of the degraded network in water. The crosslink density gradient can be controlled by the following parameters:

i. ratio of degradable crosslinks to non-degradable crosslinks

ii. total polymer weight percent (starting crosslink density)

iii. light dose (irradiance and duration of exposure).

iv. ionic strength of solution

The difference in thickness for a bilayer from equation **(7)** does not directly translate for our photodegradable hydrogel system. However, if we were to theoretically divide the photodegraded hydrogel into two equal layers (prior to equilibration post-degradation), we can, for simplicity purposes, imagine a bilayer with averaged respective volumetric swelling, which will vary as a function of degraded network strands. Here, the molar absorptivity and concentration of photoabsorbing species affects the respective layer volume swelling ratios. With these parameters in mind, we systematically studied the effect of:

i. ratio of degradable crosslinks to non-degradable crosslinks

ii. light dose (irradiance and duration of exposure)

iii. molar absorptivity of different *o*-NB macromers and

iv. rate constant of degradation of different *o*-NB macromers

v. total polymer weight percent (starting crosslink density)

vi. total starting film thickness

vii. ionic strength of solution

on folding of previously equilibrated photodegradable hydrogel networks in aqueous solutions.

II. Proof of concept: Crosslink density gradient generates swelling gradient and folding in thin films post-polymerization

Partially photodegradable hydrogels were co-polymerized in PBS using photodegradable macromer (PDM) and PEG diacrylate (PEGDA). Thin films (150 μm thickness) were cast and mm-scale samples were punched using a square leather punch or a biopsy punch. The thin hydrogel sheet was equilibrated in PBS and then exposed to UV light (365 nm) from one side. The *o*-NB moieties strongly absorb UV light, attenuating its penetration through the gel thickness. This results in a degraded region closest to the light source. The degraded region can be visualized by the light yellow to orange-brown color change caused by the higher molar absorptivity of degraded *o*-NB moieties under visible light, as previously reported by Griffin et al.[37] The difference in crosslink density translates to a difference in swelling and creates a bending moment that folds the gel when it is equilibrated in water. A scheme is demonstrated in Figure 3.1 where the exposed side with lower crosslink density swells more than the opposite side and thus curves along the outside of the folded gel.

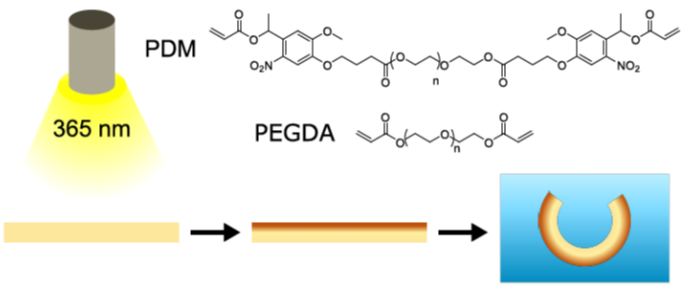

Figure 3.1 Schematic representation of photodegradable shape changing hydrogels. A flat hydrogel composed of photodegradable macromer (PDM) and PEG diacrylate (PEGDA) is exposed to long-wave UV light. The hydrogel degrades, releasing the acrylate moieties, causing a crosslink density decrease at the surface and less to no degradation at the opposite end due to light attenuation. The resulting difference in cross-link density leads to differential swelling which results in a bending moment upon immersion in water. Image reproduced with permission from Ref. 1.

III. Ratio of degradable to non-degradable strands effect on folding

To optimize the folding of tubular structures, we first studied the effect of gel composition on folding. We varied the ratio of the photodegradable macromer (PDM) to non-degradable PEG diacrylate (PEGDA) from 3:4 to 2:1, exposed the gels to UV light for 600 s at 20-100 mW/cm^2 (365 nm, 12-60 J/cm^2) and measured the inner cross sectional width of the folded gels during a 10 minute period (Figure 3.2). The initial folding was fast and typically reached its maximum 1-2 minutes after the samples were immersed in PBS. Increasing the PDM molar concentration resulted in more pronounced folding and a decreased inner cross-sectional width (Figure 3.2a-b). All the samples relaxed and unfolded to some extent during the next 10 minutes (Figure 3.2a,c). Whereas the folding is due to the fast initial diffusion of water into the degraded regions, the relaxation of the folded structure may be attributed to the slower diffusion of the fully degraded PDM linkers out of the gels. The gels with different ratios of PDM to PEGDA showed different types of folding. The 3:4 gels curled the least and were almost flat after 10 minutes. The 1:1 gels curled more than the 3:4 gels but exhibited no tube formation. The 1:1 gels also relaxed significantly with a maximum of 35% increase in the inner cross sectional width after 10 minutes. The 4:3 and the 2:1 gels both initially produced

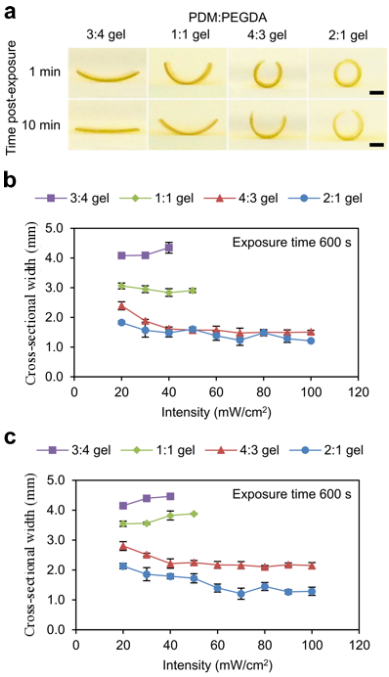

Figure 3.2 Folding of samples with different molar ratios of photodegradable macromer (PDM) to PEG diacrylate (PEGDA). Examples of gels with 3:4, 1:1, 4:3, or 2:1 molar ratio of PDM:PEGDA exposed to 40 mW/cm^2 UV light for 600 s (24 J/cm2) and imaged 1 and 10 min after UV exposure (a). Scale bars are 1 mm. Cross-sectional width of samples exposed to 20−100 mW/cm^2 UV light for 600 s (12−60 J/cm2) measured 1 min (b) or 10 min (c) after immersion in PBS. Data are shown as mean ± standard deviation (n = 3 samples). Image reproduced with permission from Ref. 1.

tubular structures, but the 4:3 gels unfolded to a higher degree with a maximum of 47% increase in the inner cross sectional width compared to 21% for the 2:1 gels. In general, the greater the PDM concentration, the greater the initial folding and the less relaxation under these exposure conditions.

IV. Evaluation of light dose effect on folding

Next, we studied the effect of exposure conditions on the folding and unfolding of the 2:1 PDM:PEGDA gels. The 2:1 condition was selected due to its greater amount of folding for all of the selected light exposures. The samples were exposed to 20-150 mW/cm^2 UV light for 600 s (12-90 J/cm^2) and the inner cross-sectional widths of the folded samples were measured over a 4-day period. Tube formation can be reproducibly controlled by the total light dose or the light intensity at a fixed exposure time. At the lower intensities or lower doses of light, there is no tube formation, but as intensity increases, first transient and then persistent tubular structures are produced (Figure 3.3a). The lower intensity limit for tube formation was 40 mW/cm^2 (24 J/cm^2), while no tubes were produced with the 20-30 mW/cm^2 intensities (12-18 J/cm^2). Between 40-150 mW/cm^2 (24-90 J/cm^2), tubes with a similar initial inner cross sectional width of 1.4 mm ± 0.1 mm were produced (Figure 3.3b). However, with intensities above 120 mW/cm^2 (72 J/cm^2), the gels were often damaged during the lift-off from the glass

slides on which they were exposed. This phenomenon could be attributed to erosion of the sample surface due to excess photodegradation. For this reason, the maximum intensity used for subsequent sample folding was set at 120 mW/cm^2.

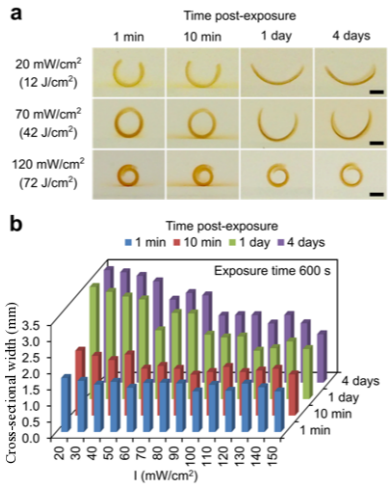

Figure 3.3 Light dose and time dependent folding of tubular structures. (a) Examples of 2:1 gels exposed to 20, 70 or 120 mW/cm^2 UV light for 600 s (12, 42 or 72 J/cm^2) and imaged 1 minute, 10 minutes, 1 day and 4 days after UV exposure. Scale bars are 1 mm. (b) Measured inner cross-sectional widths of tubular structures as a function of UV light dose and time post-exposure. Data shows mean for n = 3 samples. Image reproduced with permission from Ref. 1.

The relaxation and unfolding of samples over time is affected by the UV light intensity when the exposure time is kept constant (Figure 3.3b). The gels largely retained their folded shape over the first 10 minutes, with only a 5% average increase in diameter. After 24 h, however, significant light dose dependent unfolding was observed. The average increase in cross sectional width was 72% for samples exposed to the lower intensities of 20-80 mW/cm^2 (12-48 J/cm^2) and 28% for samples exposed to the higher intensities of 90-150 mW/cm^2 (54-90 J/cm^2) at a fixed exposure time of 600 s. Between day 1 and day 4, the sample cross sectional widths remained more stable with an average increase of 8%. The unfolding thus occurs within 1 day of the initial curling, after which the sample shapes remain largely unchanged. The tubular structures with smallest initial cross sectional widths retain their shape the best after the initial relaxation during the first day. By increasing the UV light intensity and therefore the total light dose, permanent tubular structures are produced.

V. Molar absorptivity and degradation rate effect on folding

Modeling: photodegradation for o-NB macromers with different molar absorptivity and degradation rates

The folding of thin film hydrogels was shown to result from a difference in swelling through the film volume. We further studied the effect of molar absorptivity, or light attenuation, on folding using a library of previously reported *o*-NB macromers. Previously, Griffin et al. reported a series of *o*-NB linkers with different molar absorptivity values and rates of photodegradation.[37] From this library, we synthesized the macromers with highest and lowest molar absorptivity values at 365 nm, namely the PEG conjugated 4-(4-(1-hydroxyethyl)-2-methoxy-5-nitrophenoxy) butanoic acid and the PEG conjugated 1,3-dihydroxymethyl-2-nitrobenzene (or the B and E macromers respectively as they were referred to in the manuscript). While the two *o*-NB macromers were reported to have very different absorptivity values, their kinetic rate constants of degradation were similar. This suggested that while the E group had a much lower molar absorptivity of 146.7 $M^{-1}cm^{-1}$ compared to 3500 $M^{-1}cm^{-1}$ for the B group, the E group had a much higher quantum yield. A third macromer was selected due to its high kinetic rate constant of degradation. The PEG conjugated 4-(3-(1-hydroxyethyl)-4-nitrophenoxy) butanoic acid (or D macromer) has a similar molar absorptivity as the B group at 365 nm and thus attenuates light similarly. However, it was reported to have 2.5× higher kinetic rate constant normalized to irradiance (k_{app}/I_0) compared to the B group (8.3 vs 3.3 $\times 10^4$ $cm^2/(mW \times s)$). We decided to further study the B, E and D macromers in order to compare the effects of light attenuation and kinetic rate constant on folding due to photodegradation.

With knowledge of the B, E and D group photodegradation constants, equations **(1)** and **(2)** could be used to determine photodegradation as a function of film depth. A statistical model that predicts the proportion of elastically active (intact) and dangling network strands was developed by Kasko and coworkers.[100] The model takes in to account the diffusion timescale of photoabsorbing species that are released from the network during the light exposure window. With these tools, we modeled hydrogels with 22.8 total polymer wt% at 1.7:1 molar ratio PDM:PEGDA. We chose these starting conditions based on data showing that more folding was observed with increasing B group macromer concentration up to 2:1 molar ratio of PDM:PEGDA. Additionally, we wanted to avoid erosion of the hydrogel due to photodegradation. With these starting conditions, we do not expect to observe photodegradation induced erosion since the reverse gel point, p_{rg}, is approximately 0.7 for chain polymerized fully photodegradable hydrogels with an N (number of crosslinking molecules per kinetic chain) of 20. Thus, if at least 30% of the chains are non-degradable PDA, then p_{rg} is 1 and the critical time to erosion:[101]

$$t_c = \frac{-\ln(1-p_{rg})}{k_{eff} I_0} \qquad \textbf{(10)}$$

is undefined. We thus selected a 1.7:1 molar ratio to add a 10% buffer for preventing erosion due to photodegradation, and modeled photodegradation at 365 nm as a function of depth for 150 μm gels for the different *o*-NB macromers. The light exposure conditions, molar absorptivity and rate constants used are listed in (Table 3.1). The normalized number of degraded and intact network strands was plotted as a function of depth for each condition.

Table 3.1 *o*-NB macromer molar absorptivity (ε), rate constant (*k*), and light dose used for determining fraction of degraded network strands as a function of depth

o-NB macromer	ε_{365} ($M^{-1}cm^{-1}$) (undegraded/degraded)	k_{365}/I_o ($cm^2/(mW\times s)$)	I_0 (mW/cm^2)	Time (s)	J_0 (J/cm^2)
B	3500/2637	3.3	5-100	600	3-60
E	146.7/507.7	2.6	5-100	600	3-60
D	2509/4061	8.3	5-100	600	3-60

We simulated photodegradation as an exposure event from one side of a thin hydrogel film and arbitrarily called it the top. The side opposite the exposure was called the bottom. Using the simulation, we divided a 150 μm gel into top and bottom halves (75 μm each) and calculated the ratio of the average number of intact network strands for each side (Figure 3.4). The intact strands are the elastically active network strands, which are inversely proportional to swelling ratio (equation **(4)**). We expect no folding when the ratio of intact strands between top and bottom (v_t/v_b) is equal to 1 and an increase in curvature with decreasing ratios. We see that for all light doses, the E gels have a 1:1 ratio of top:bottom intact network strands supporting what we would predict from the lower molar absorptivity value for the E gels. This suggests that the E gels will bulk degrade through the film depth at 365 nm and thus should not fold upon re-equilibration. Instead, the B gels have a quickly decreasing ratio of top:bottom intact strands as a function of light dose from 0.7 at 6 J/cm^2 to 0.4 at 42 J/cm^2. From experimental data with the B gels, we observed folding with similar gel conditions at irradiance values between 20-150 mW/cm^2 (12-90 J/cm^2) and tube formation at 24 J/cm^2 (40 mW/cm^2, 600 s exposure time). The D gels, having a similar absorptivity as the B gels, but with a higher rate constant, degrade faster. For an equal light dose at 6 J/cm^2, the D gels not only have

more degraded strands through the total volume, but they also have a smaller ratio of intact strands, v, between top and bottom. Our modeling results predict that the D gels reach maximum curvature at 18 J/cm^2 and then level off or experience decreased folding for increasing light dose as the bottom layer of the gel degrades more and more. Instead, v_t/v_b is higher for B gels at low light doses and continues to decrease at light doses beyond 18 J/cm^2. At 30 J/cm^2 the v_t/v_b levels off or starts to increase for the B group (Figure 3.4).

The relationship between change in modulus as a function of degradation is proportional to elastically active network strands (intact strands) normalized to the original number of active network strands where:[101]

$$\frac{G}{G_0} = \frac{v}{v_0} = \exp(-kt) \qquad (11)$$

Assuming that the top and bottom "layers" are free to swell as if they were independent of each other, we calculated the volume swelling ratio, Q_m, for the top and bottom sides using the number of intact strands (ignoring dangling strands at the moment) using equations **(5)**, **(6)** and (**11**). The undegraded volume swelling ratio, Q_0, was measured for each of the B, E and D gels as 10.8 ±0.4, 10 ±0.2 and 10.3 ±0.4 respectively. A plot of the volume swelling ratio between the top and bottom, Q_t/Q_b, demonstrates how the ratio increases faster for the D group than for the B group so that at 18 J/cm^2 Q_t/Q_b *is* 8% greater for D than B (Figure 3.4). However, for increasing light doses, Q_t/Q_b begins to decrease for the D group before it starts to do the same with the B group, again suggesting maximum curvature with the D gels at lower 365 nm light dose than for the B group.

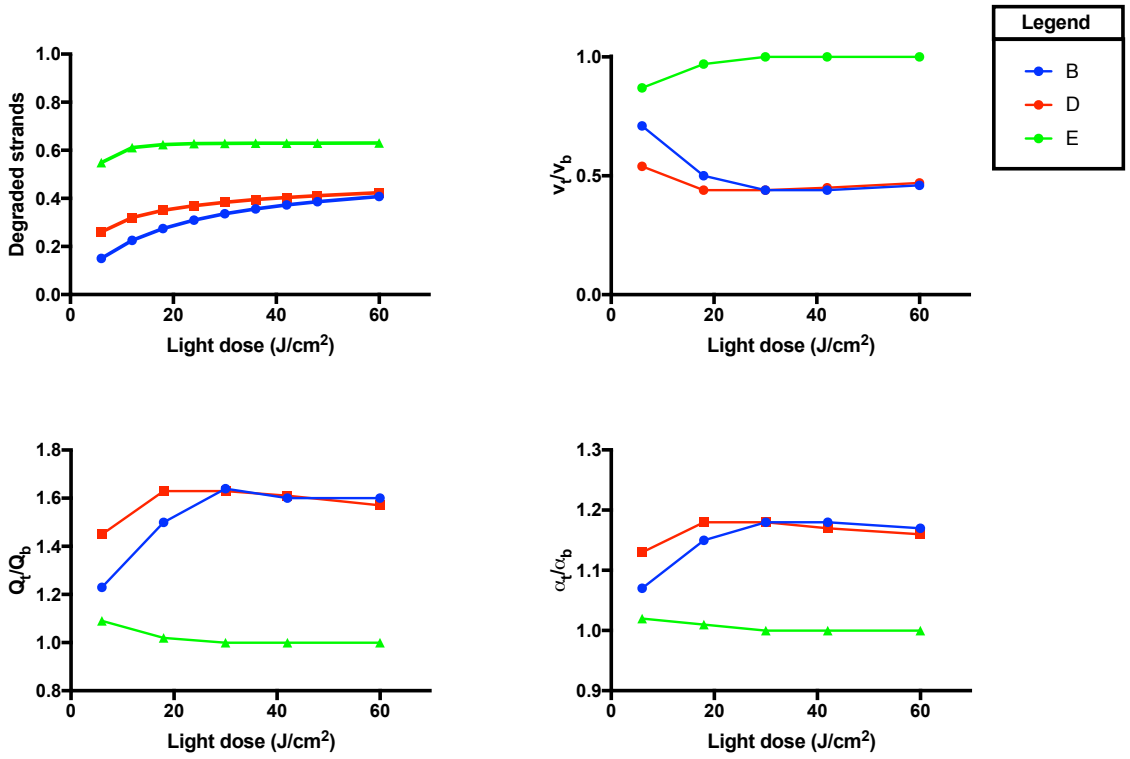

Figure 3.4. Degradation profile for optically thick (150 μm) partially degradable hydrogels using diffusion model to predict intact network strands following 365 nm exposures. The graph on the top left is an estimation of the degraded strands through the entire gel volume. The remaining three graphs are the top to bottom ratio intact network strands (top right), volume swelling (bottom left) and linear elongation (bottom right). The linear elongation α_t/α_b was calculated using $(Q_t/Q_b)^{1/3}$ assuming equal extension in each direction.

Empirical verification of photodegradation effect on self-folding for B, D and E o-NB macromer hydrogel films with different molar absorptivity and degradation rates

The B, E and D macromers were selected for comparison based on their molar absorptivity and kinetic rate constants of degradation. We hypothesized that little to no folding would be observed in E group hydrogels due to their low molar absorptivity at 365 nm and Q_t/Q_b values of approximately 1 for all light doses. Furthermore, we predicted that the D group would have maximum curvature at lower light intensities compared to the B group due to the D group having a 2.5× higher kinetic rate constant of degradation compared to the B group and a greater Q_t/Q_b at < 30 J/cm^2 (Figure 3.4).

We tested our hypotheses by preparing partially degradable hydrogels with the B, E and D macromers at 22.8 wt% and 1.7:1 molar ratio PDM:PEGDA. The hydrogels were cast at 150 μm thickness, equilibrated in PBS overnight and then exposed at 365 nm for 600 s at 30, 70 or 100 mW/cm^2 (18, 42 or 60 J/cm^2 respectively). Following exposure, 4 mm diameter discs were punched and immediately transferred to a PBS bath for equilibration. The gels were imaged 1 day after photodegradation to allow for equilibration.

Amount of folding as a function of light dose at 365 nm for B, D and E macromers

Folding was characterized by two measures. The first was termed the closure angle, measured by treating the inner edge of the gel as an arc. The closure angle was measured between opposing ends of the gel with the vertex at the point on the arc where the tangential slope was equal to zero (Figure 3.6). For perfectly flat gels the closure angle is 180° and for folded gels with overlapping opposing ends the closure angle is 0°. The radius of curvature was also calculated by fitting a circle to the inner arc, or bottom surface of the gel (opposite the exposed side).

As predicted, the E gels remained flat with approximately 180° closure angle for all of the light exposures. The D gels folded more than the B gels at the lowest light dose (Figure 3.5, closure angle), and they did not exhibit dose dependent folding (i.e., there was no change in closure angle or radius of curvature as a function of light dose). In contrast, the B gels had dose dependent folding with the smallest closure angle for the highest light dose at 60 J/cm^2 (Figure 3.5) and a significant difference between closure angles for all of the exposure conditions. These results are somewhat in agreement with the modeling results predicting maximum curvature for the D gels at 18 J/cm^2 and a small

increase in Q_t/Q_b for increasing light doses up to 60 J/cm^2, which should result in slightly less curvature (increased radius of curvature). The modeling of photodegradation through film depth also predicted the largest change in Q_t/Q_b for the B gels between 18-42 J/cm^2 with a modest increase in Q_t/Q_b at 60 J/cm^2 (from 42 J/cm^2). While we observed decreasing radius of curvature with increasing light dose between 18-60 J/cm^2 for the B gels, we observed the largest change in radius of curvature from 18 to 42 J/cm^2 and a more modest change from 42 to 60 J/cm^2.

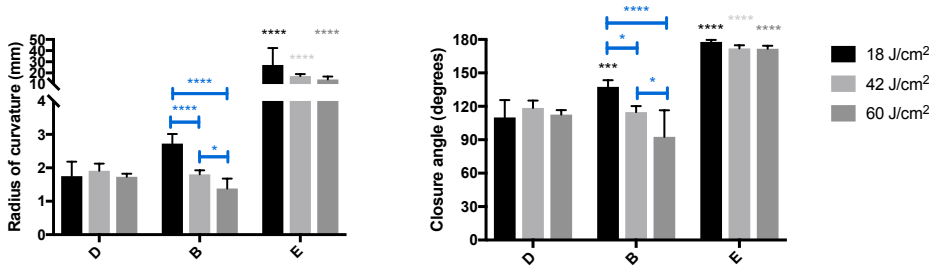

Figure 3.5 Radius of curvature (left) and closure angle (right) for D, B and E- macromer gels exposed at 18, 42 or 60 J/cm^2 (365 nm wavelength, 600 s exposures). The D and B group gels folded significantly more than the E-gels for all conditions. (The gray-scale stars denote significant difference as determined by t test compared to the D gel exposed at the same light dose. The B gels had significantly larger closure angle (less folding) than the respective D gel at 18 J/cm^2 but not at the higher light doses. The E gels had significantly higher closure angles compared to the D gels at all the light doses. The D-gels had similar folding for all light doses. Instead, the B group gels exhibited dose dependent folding with the most curling at the highest light dose. Intermediate and low light doses revealed significantly less folding as determined by radius of curvature and closure angle. (The blue stars denote significant difference as determined by t test between indicated exposure conditions for the B group gels). (* $p < 0.05$, *** $p < 0.001$, **** $p < 0.0001$, data are shown as mean ± standard deviation with n=8 samples for the D group and 7 samples for the B and E groups)

Actuation strain as determined by measuring top and bottom lengths for top-side UV exposure of B, E and D o-NB macromer hydrogels

Our results indicate that at 22.8 polymer wt% and for a matched starting thickness of 150 μm, the D and E gels experience light dose independent shape-change (for the range of light exposures tested). Instead, the B gels exhibit dose dependent folding. We know that folding results from a difference in swelling through the gel volume that is balanced by the network elasticity. With this in mind, we wanted to further characterize

the degradation profiles through the hydrogel films' depths and understand if there is a correlation with the amount of folding. From Flory's Principles of Polymer Chemistry,[51] the swelling of a crosslinked polymer network can be described by

$$Q_m = {\alpha_s}^3 \qquad \textbf{(12)}$$

where α_s is the linear elongation parameter describing the change in length of the polymer network in the swollen state for isotropic swelling.

Based on modeling of the degraded network strands as a function of gel depth for each of the macromers, we predicted that depending on the molar absorptivity of the samples at 365 nm exposures, the hydrogels would exhibit a range of swelling gradients through the gel thickness. Although it is difficult to empirically characterize crosslink density and swelling gradient profiles through the degraded gels' depth, we simplified our system by measuring the lengths of the two extreme conditions of our gels—i.e., the most degraded exposed side (referred to as top) and the opposite side (referred to as bottom). The ratio of top to bottom path lengths gives us indirect information about the swelling through the gel depth since

$$\frac{C_t}{C_b} \propto \frac{\alpha_{st}}{\alpha_{sb}} \qquad \textbf{(13)}$$

where C_t and C_b are equal to the top/exposed side and bottom/opposite side lengths of the gel respectively. For the case of photodegradable macromers with low molar absorptivity where light is transmitted through the depth of the gel, such as with the E group, we expect isotropic change in crosslink density and swelling. Therefore, we predicted that there should be a unit ratio between the length of the top and bottom edges and no folding. In other words, $C_t/C_b = 1$. For the other extreme case where the gels fold in to a tube and the ends meet, we expect the bottom (or inner) radius to be

$$r_b = \frac{C_b}{2\pi} \qquad \textbf{(14)}$$

In the case of *o*-NB macromers with high molar absorptivity, there is complete light attenuation through a sufficiently thick gel (i.e. little to no transmission through the opposite end) and thus little to no change in crosslink density. In this case, we predict that C_b should be approximately equal to the diameter of the flat gel disc before degradation, which is 4 mm in our case. Thus, we expect r_b is equal to 0.63 when the opposite ends of the gel meet to form a tube. The top circumference of the gel can similarly be calculated by

$$C_t = (r_b + \gamma)2\pi \qquad \textbf{(15)}$$

where γ is the gel thickness after equilibration in water following photodegradation. In this other extreme case

$$\frac{C_t}{C_b} = \frac{r_b + \gamma}{r_b} \qquad \textbf{(16)}$$

As expected, C_t/C_b for the E gels was approximately 1 for all exposure conditions (Figure 3.6). For the D gels, C_t/C_b was equal to 1.13 ± 0.01 for all the exposure conditions. This finding was somewhat expected considering that the radius of curvature and closure angle was also fairly constant as a function of light exposure. This is also in agreement with the modeling predictions suggesting maximum curvature at 18 J/cm^2 with little to no change in swelling ratio for increasing light dose up to 60 J/cm^2. These tell us that for both the D and E gels, all the light exposure conditions not only result in similar extent of folding (i.e. closure angle and inner radius of curvature) but also similar ratio of elongation parameters at either surfaces of the gels (exposed vs. opposite side). In contrast, the B gels exhibited dose dependent top to bottom swelling ratio, where we observe increasing C_t/C_b with decreasing radius of curvature (more folding). A plot of

C_t/C_b as a function of r_b demonstrates the monotonic trend for the D and E gels at the 3 exposure conditions (18, 42, and 60 J/cm^2) and a $1/r_b$ trend for the B gels (Figure 3.6). Surprisingly, a plot of C_t/C_b as a function of thickness for the B gels demonstrated an increasing trend with decreasing thickness.

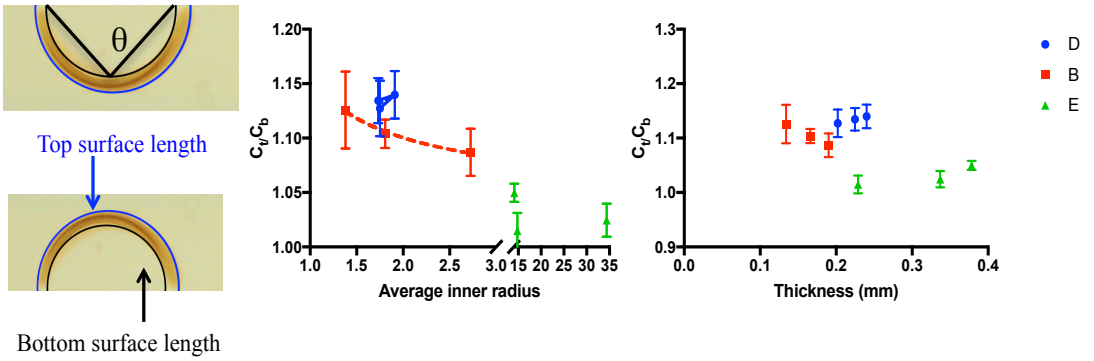

Figure 3.6. Swelling induced actuation strain for top surface exposed D, B and E hydrogels. Top left demonstrates how the closure angle was calculated to describe extent of folding. Bottom left delineates what we defined as the top surface, which is also the exposed side of the gel, and the bottom surface, which is the opposite side. The end-to-end path length of each gel surface was calculated to gain a better understanding of the differential swelling through the gel. The top to bottom length ratios as a function of inner radius were plotted (middle). The E group gels were flat for all exposure conditions and thus had unit ratio of C_t/C_b indicating homogenous swelling through the gel depth. The D gels had similar C_t/C_b for all three exposure conditions. However the B gels demonstrated increasing C_t/C_b with decreasing radius of curvature (i.e. more folding) indicating that not only did higher light doses yield more folding but that the more tightly folded gels had a bigger difference in swelling through the gel depth. Data are shown as mean ± standard deviation with n=4-9 samples per condition

In summary, we found that when comparing the three macromers with matched total polymer weight percent and 1.7:1 molar ratio of PDM:PEGDA, the B and D gels folded after 365 nm UV light exposures while the E gels did not. We further characterized the change in swelling through the gel thickness by measuring the length of the top and bottom sides of the gels and demonstrated that the E gels had a 1:1 ratio for all the exposure conditions, as expected, due to the E group's low molar absorptivity. For the D and B gels, the top:bottom length ratio was greater than 1 as expected due to their higher molar absorptivity values. However, with the D group, we observed no change in ratio as a function of exposure conditions. This agrees with the results for closure angle

and radius of curvature as a function of exposure as well as modeling predictions for v_t/v_b and Q_t/Q_b. In contrast, the B gels had increasing folding with increasing light dose and the top:bottom length ratio similarly increased with increasing light dose—substantiating that folding resulted from a difference in swelling through the gel depth.

VI. Molar absorptivity at different wavelengths can be used to selectively fold and unfold hydrogels

In the spirit of the modeling and experiments that were done to predict folding with the B, E and D gels, we predicted that folding and unfolding could be generated by exposing the B and D gels at different wavelengths. While the B and D gels both have high molar absorptivity values at 365 nm, there is a large decrease for both at 405 nm. The decrease is much more pronounced for the D gels (161 $M^{-1}cm^{-1}$) than for the B gels (845 $M^{-1}cm^{-1}$).[37]

The difference in absorbance between the degraded and the non-degraded *o*-NB molecules leads to a visible change in color upon photodegradation. We utilized this feature to experimentally verify the depth of degradation in optically thick, 1 mm gels, at 365 and 405 nm. At 365 nm, we observed an increase in "degradation depth" for the B gels at 42 J/cm^2 compared to 18 J/cm^2. However, in agreement with the folding experiments with the analogous thin films, the D group gels had the same degradation depth at 18 and 42 J/cm^2. Furthermore, at 405 nm, the B gels again appeared to attenuate light while the D group gels had degradation depths > 0.5 mm (Figure 3.7). These results suggest that the B gels attenuate light sufficiently at 405 nm to generate a crosslink density gradient while the D group gels experience more homogenous depth degradation. Based on these preliminary results, we decided to study the effect of differences in molar

absorptivity at 365 and 405 nm on step-wise folding—namely initial photodegradation induced folding followed by either unfolding or increased folding at an arbitrary user defined time point.

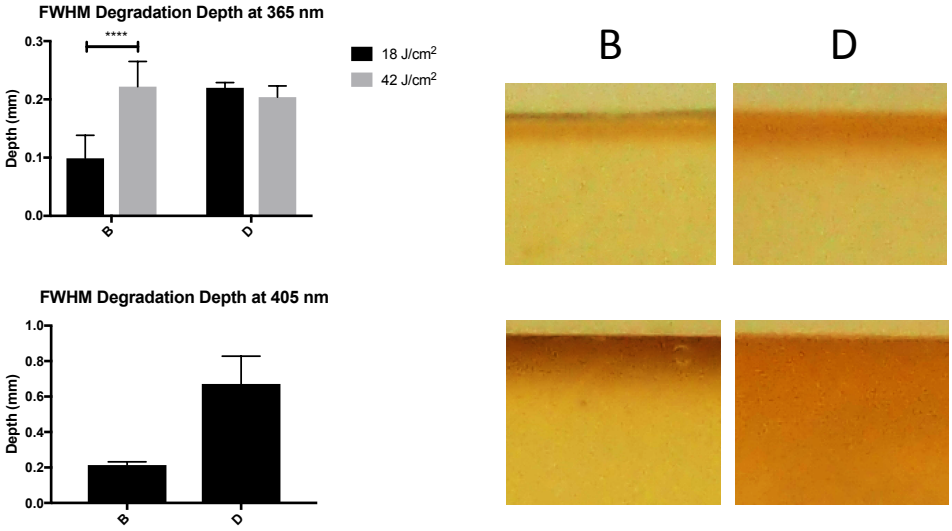

Figure 3.7 Degradation depth determined in thick samples for 365 (top) and 405 (bottom) nm light exposures. The degradation depth increased as a function of light dose for the B group hydrogels at 365 nm (top left) (**** denote p value <0.0001 as determined by t test, n=6). At 405 nm, the D group hydrogels experienced degradation depths >0.5 mm while the B group gels have a lower degradation depth of 0.2 mm (bottom left, n=6). The images on the right are cross-sections of hydrogels exposed at 365 (top right) and 405 (bottom right) nm light exposures. Data are shown as mean ± standard deviation.

Partially degradable B and D gels were polymerized using PDM and PEGDA at a 1:7:1 molar ratio. The hydrogels were folded in to containers by exposing a four-leaf clover with a mask in the center at 365 nm. The gels were equilibrated in PBS overnight and imaged after folding. The gels were then exposed at 405 nm in their folded, equilibrated state from either the top (opposite to 365 nm side exposure) or the bottom (same as 365 nm side exposure).

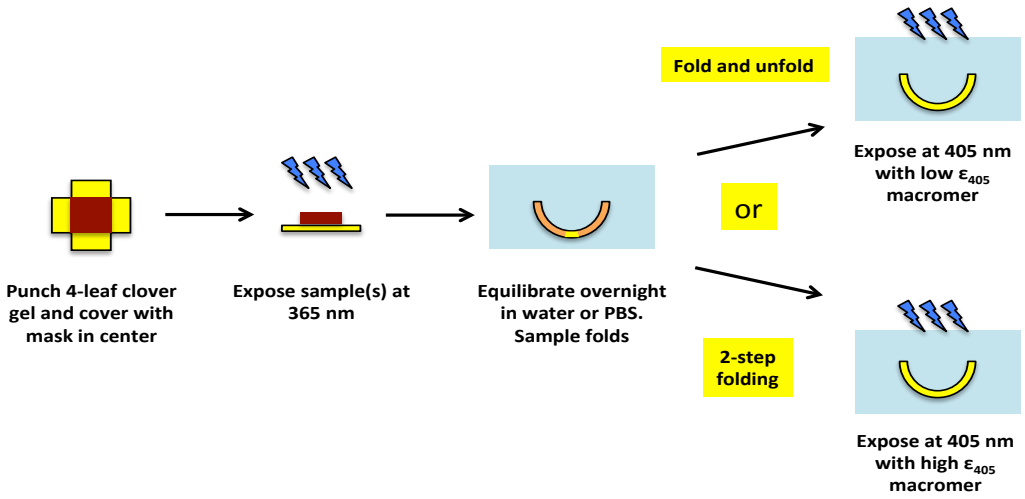

Figure 3.8. Schematic diagram of photodegradation induced change in curvature at two wavelengths. The hydrogels are first folded using 365 nm light. Next, hydrogels with high ε_{405} nm can be further curled with flood exposure to 405 nm light and hydrogels with low ε_{405} can be unfolded with flood 405 nm exposure

The B and D group hydrogels had a similar folding response after the initial exposure at 365 nm (Figure 3.9). However, the secondary 405 nm exposure resulted in very different curvature changes. The B gels had an increase in curvature whether they were exposed from the opposite or the same side as the initial 365 nm exposure. However, the D gels completely unfolded following the 405 nm exposures. These results further demonstrate how the differences in molar absorptivity of photodegradable macromers can be used to selectively tune step-wise folding or folding and un-folding at different wavelengths.

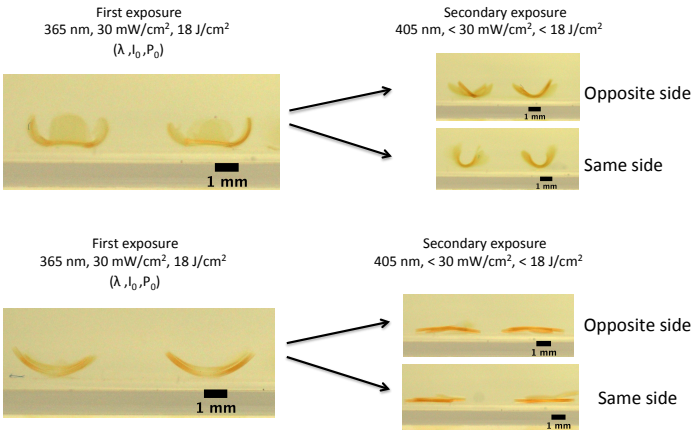

Figure 3.9. Sequential shape change at 365 nm and 405 nm. Two-step folding for B macromer hydrogels, which were first folded using 365 nm light. The secondary exposure at 405 nm from either the opposite or same side resulted in increased curling as the previously masked center region degraded. (top) Folding and unfolding for the D macromer hydrogels. The D gels were first folded using 365 nm light. The secondary exposure at 405 nm from either the opposite or same side as the first exposure resulted in unfolding. (bottom)

Optimization of folding for minimizing light dose

In order to decrease the light dose required for high amounts of folding, we further studied the D group *o*-NB gels since we observed more folding (lower closure angle and radius of curvature) at low light doses compared to the B group gels (Figure 3.5). We predicted that decreasing total polymer weight percent as well as decreasing film thickness would help optimize folding while decreasing light dose required.

VII. Crosslink-density effect: change in swelling and resulting folding for 22.8% and 17% D *o*-NB gels

We first modeled the ratio of intact strands for both 22.8 and 17 wt% (total polymer) conditions with 1.7:1 molar ratio PDM:PEGDA. As expected, for matched light dose exposure at 365 nm, the lower weight percent gels predicted more degradation through the depth of a 150 μm gel. In order to compare the two gel types for a range of exposure conditions, we integrated intact network strands for the top and bottom half of the simulated gel exposed from the top. We then calculated the top:bottom ratio (exposed:opposite side ratio). In Figure 3.10 we demonstrate that at the lowest light dose, 6 J/cm^2, the 17% gels have smaller top:bottom intact strand ratio, thus predicting a larger difference in swelling between the two halves of the gel at lower light exposures. However, for increasing light doses, v_t/v_b, increases much more quickly for 17% gels than for 22.8% gels. This is because degradation through the hydrogel depth is a function of the concentration of photoabsorbing species.

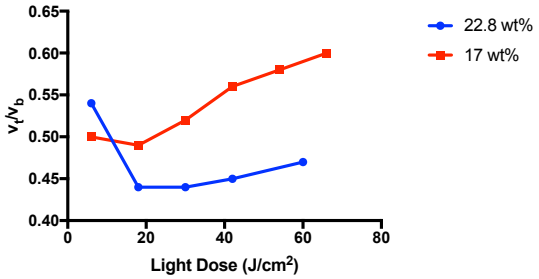

Figure 3.10. Modeling prediction of ratio of intact strands between the top (exposed) and bottom (opposite) sides for 22.8 and 17 wt% gels.

Because the lower weight percent gels also have lower overall concentration of *o*-NB, light penetrates the hydrogel depth faster, thus causing a faster decrease in v_b in the 17% gels than in the 22.8% gels. The faster decrease in v_b also causes a faster increase v_t/v_b.

Hydrogel films were prepared as previously described with 150 μm thickness using 1.7:1 molar ratio of D group *o*-NB PDM:PEGDA. We again measured little change in folding for the 22.8% gels as a function of light dose. Also, we again observed maximum curvature, or minimum closure angle and minimum radius of curvature at 18 J/cm^2. Unlike the 22.8% gels, the 17% gels had decreasing closure angle and radius of curvature with increasing light dose. These results did not agree with the modeling predictions, which suggested that the 17% gels should have decreased folding (or increasing radius of curvature) for increasing light doses beyond 6 J/cm^2.

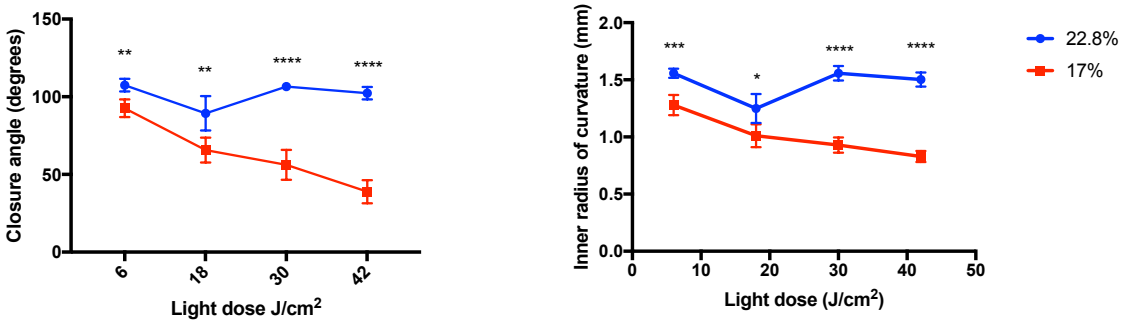

Figure 3.11. Total polymer weight percent effect on folding as a function of light dose. The 22.8 wt% gels exhibited similar folding as a function of light dose as they did in previous measurements and consistent with previous results, there was little change in curvature as a function of light dose. In contrast, the 17% gels had increased folding with increasing light dose. Stars denote p-value of t-test for difference between the two compositions for matched light exposure (* $p < 0.05$, ** $p < 0.01$, *** $p < 0.001$, **** $p < 0.0001$). Data are shown as mean ± standard deviation with n=3-10 samples per condition

Folding curvature has been shown to be affected by overall film thickness for bilayers where curvature increased with decreasing thickness.[26,102] Therefore, to ensure that the change in curvature was due to polymer content and not a change in thickness,

we measured the thickness of the photodegraded and equilibrated gels using images of the curled samples. There was a trend towards greater thickness for the 17% gels, as we would expect due to greater swelling; however the difference was not detectable using this measurement for the 6, 18 and 30 J/cm^2 light doses (Figure 3.12) There was a significant difference in thickness between 17% and 22.8% gels at 42 J/cm^2, however, since the trend was not consistent across increasing light dose, it was not clear what to make of the difference. Furthermore, since the 17% gels were thicker than the 22.8% gels, we can likely discount thickness being the cause for increased curvature in the 17% gels.

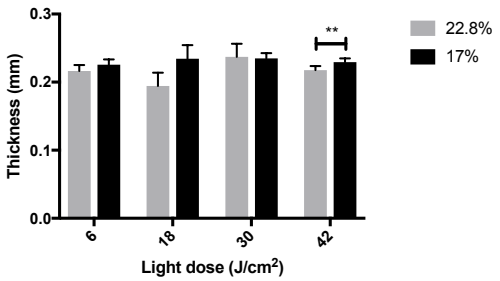

Figure 3.12. Change in thickness for 22.8% and 17% gels for range of light doses. Data are represented as means ± standard deviation with n=3-10 samples per condition. ** Indicate $p < 0.01$ as determined by t test.

VIII. Hydrogel thickness effect on shape-change

Finally, we modeled the ratio of top:bottom intact strands (v_t/v_b) for both 100 and 150 μm thick hydrogels with 22.8 wt% (total polymer) and 1.7:1 molar ratio PDM:PEGDA (Figure 3.13). The thinner gels predicted a greater percent degradation for equal light doses

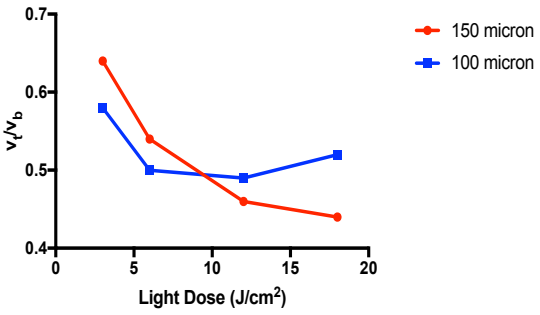

Figure 3.13 Ratio of top to bottom intact strands for 22.8 wt% partially degradable hydrogels of 150 and 100 micron thickness. While the thinner gels have a lower degradation ratio at the lowest light doses, the ratio begins to increase for increasing light dose beyond 12 J/cm^2 while the thicker gels reach a minimum at 18 J/cm^2

and reached a minimum v_t/v_b at a lower light dose of 6 J/cm^2 than the thicker gels which reached a minimum at 18 J/cm^2. However, the 150 μm gels predict a smaller v_t/v_b at 18 J/cm^2 than the 100 μm gels do at 6 J/cm^2.

In order to experimentally determine whether folding could be optimized for decreased light exposure, we prepared 22.8 wt% gels between either 100 or 150 μm spacers (height before equilibration). The gels were exposed using collimated 365 nm light and imaged following equilibration in PBS.

For the 100 μm gels, optimal folding was reached at the 6 J/cm^2 light dose (Figure 3.14), which is in close agreement with the modeling predictions for the ratio of top to bottom intact strands. The 150 μm gels had optimal folding at 18 J/cm^2, which again is in agreement with the modeling results. Interestingly, the gels experienced similar amounts of folding at the 18 J/cm^2 dose. The minimum closure angle and radius of curvature for the 100 μm gels was smaller than for the 150 μm gels. This demonstrates that although modeling the distribution of degraded strands through the film depth can help us predict approximately at what light doses we expect maximum curvature, it is not a good predictor for the amount of curvature. Furthermore, we note that there should be a minimum thickness, below which curvature does not increase for minimum light dose exposure. This thickness will depend on the molar absorptivity of the photolabile species as well as the minimum light dose that can be used. We expect that for 22.8% D group gels exposed to low light doses of about 0.5 J/cm^2 at 365 nm, the optimal minimum thickness would be approximately 20-40 μm based on modeling results (not shown).

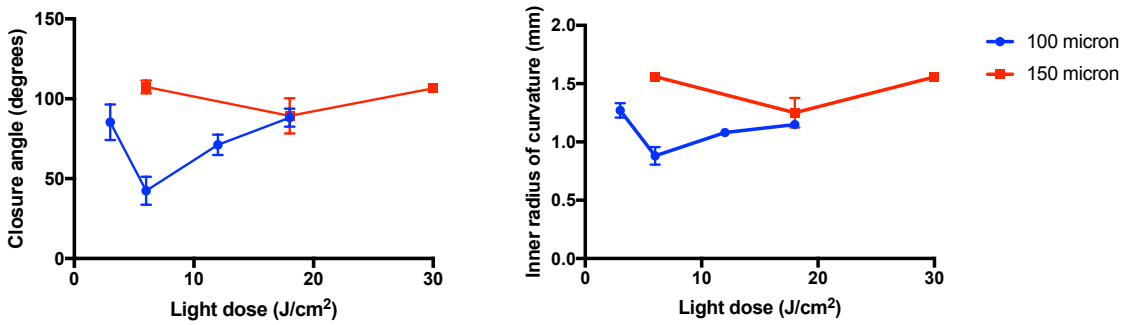

Figure 3.14 Comparison of film thickness effect on folding as a function of light dose. The 100 μm gels had maximum folding or minimum closure angle and radius of curvature at 6 J/cm^2 while the 150 μm gels experienced maximum curvature at 18 J/cm^2 (Data are shown as mean ± standard deviation with n=3-10 samples per condition).

IX. Ionic strength effect

Following a photodegradation event, the degraded *o*-NB molecule is released from the network and a carboxylic acid remains attached to the network at the cleavage site (Figure 3.15). Therefore, the degraded regions of the hydrogel, not only differ from the non-degraded regions in that the crosslink density is lower, but they are also anionic at physiological pH, when the carboxylic acid is deprotonated. Ionic hydrogels experience increased swelling due to the electrostatic repulsion from the fixed localized ionic charges. However, other ions in solution are free to diffuse through the gel and as such the sodium and potassium ions in PBS screen the fixed anionic charge on the carboxylic acids, analogous to Donnan membrane equilibrium.[103] The osmotic pressure arising from the difference in ion concentrations can be approximated by balancing the osmotic pressure from the ions attached to the network and the solution counterions with the polymer-solvent interaction and the elastic component of the network:

$$\frac{iv_{2m}}{v_u z_-} - v(c_s^* - c_s) = \left(\frac{1}{v_1}\right)[\ln(1 - v_{2m}) + v_{2m} + \chi_1 v_{2m}^2] + \left(\frac{v_e}{V_0}\right)\left(v_{2m}^{\frac{1}{3}} - \frac{v_{2m}}{2}\right) \quad \textbf{(17)}$$

where i is the number of electronic charges per polymer unit, v_u is the molar volume per charged unit (so that iv_{2m}/v_u is the concentration of fixed charges per unit volume), z_- is

the cation valence, v is the total number of mobile ions, c_s and c_s^* are the molar salt concentration within a polyelectrolyte and the surrounding medium respectively.[51] In the case where the concentration of mobile ions is very low, such as when distilled water (DI water) is the solution, the second term on the right side of equation **(17)** is negligible and the very high osmotic pressures in these cases will cause v_{2m} to be very small. In a good solvent and in our case when the valence is 1, we can also treat the last term in equation (**17**) as negligible and the equilibrium swelling can be simplified in to:

$$Q_m^{2/3} \cong \left(\frac{i}{z\_v_u}\right)/(v_e/V_0) \qquad \textbf{(18)}$$

We empirically compared the differences in swelling induced shape-change in PBS vs. distilled (DI) water by preparing partially degradable hydrogels of 100 μm thicknesses. The samples were exposed at 365 nm for 300 s at either 10 or 40 mW/cm^2. Squares of 10×10 mm were cut and equilibrated in PBS overnight. The folded samples were then imaged in both PBS and water following equilibration in each. We observed a 3 and 2 fold decrease in average cross-sectional width at 3 and 12 J/cm^2 respectively (Figure 3.16) suggesting a larger difference in the actuation strain in DI water compared to 1× PBS. The change in folding was reversible.

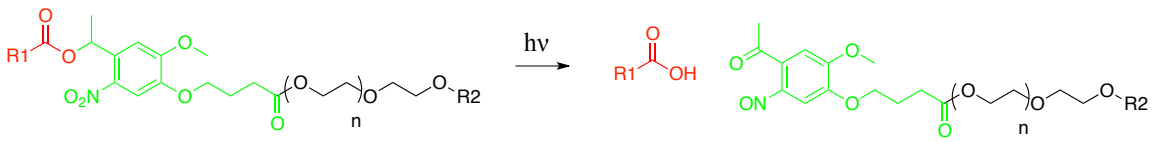

Figure 3.15 Schematic photodegradation reaction of *o*-NB conjugated to polymer network. Photodegradation of *o*-NB molecule results in nitroso-ketone (green) being released from the network and a carboxylic acid (red) dangling from the hydrogel network. The red structures represent the hydrogel network attached to *o*-NB benzylic position for photorelease. R1 also represents the hydrogel network. The green structures are the base photolabile *o*-NB molecule. The black structures are the PEG chain conjugated to the *o*-NB molecule on its non photolabile side and R2 represents the hydrogel network.

We suspected that there should be no difference in swelling in the two aqueous solutions for the non-degraded hydrogels whereas the degraded hydrogel could have a

difference in swelling due to the appearance of network-pendant carboxylic acid groups following photo-degradation. In order to further study this effect and simulate the anionic photodegraded hydrogels, we prepared PEG and PEG-acrylic acid hydrogels. The mass immediately after polymerization was measured in 1× PBS and for two days to equilibration. The gels were then equilibrated in DI water for two days and then changed back in to 1× PBS and again to DI water. We observed a constant mass for the PEG gels after 24 h in aqueous solution and regardless of the buffering state. Instead, the PEG-acrylic acid gels had a reversible mass increase in water compared to 1× PBS (Figure 3.17). The volume swelling ratio, Q, was calculated using the swollen gel mass in either 1× PBS or in water and the dry mass. There was a significant difference in swelling ratio for the PEG-acrylic acid gels in DI water compared to 1× PBS. There was no difference in swelling for the PEG gels in water vs. PBS and the PEG-acrylic acid gels had similar swelling compared to the PEG gels in PBS. Finally, we compared the effect of buffer ionic strength on Q for PEG-acrylic acid gels and observed a dose dependent decrease in swelling as the buffer salt concentration increased, further demonstrating the effect of charge screening due to mobile ion concentration.

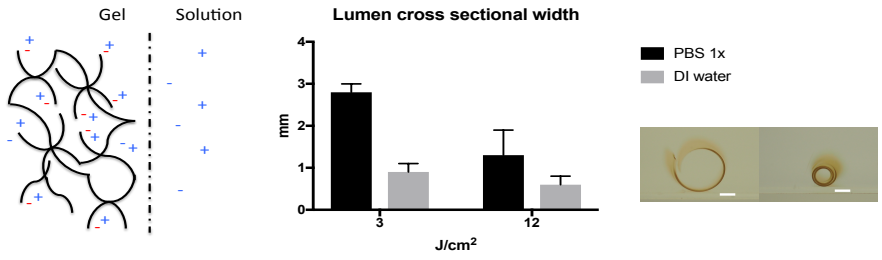

Figure 3.16 Charge screening in buffered aqueous solutions affects curvature of shape changed gels with pendant carboxylic acid groups. Schematic of anionic hydrogel behaving like a Donnan equilibrium membrane with red anions representing the network bound negative charges and the blue +/- representing the mobile ions from the buffered solution (left). The effect of 1× PBS vs. DI water on lumen width at 3 and 12 J/cm^2 light exposures (middle, data are shown as mean ± standard deviation, n=3 samples per condition). Image of the same hydrogel in 1× PBS (left) and DI water (right) with scale bar representing 1 mm in both images (right).

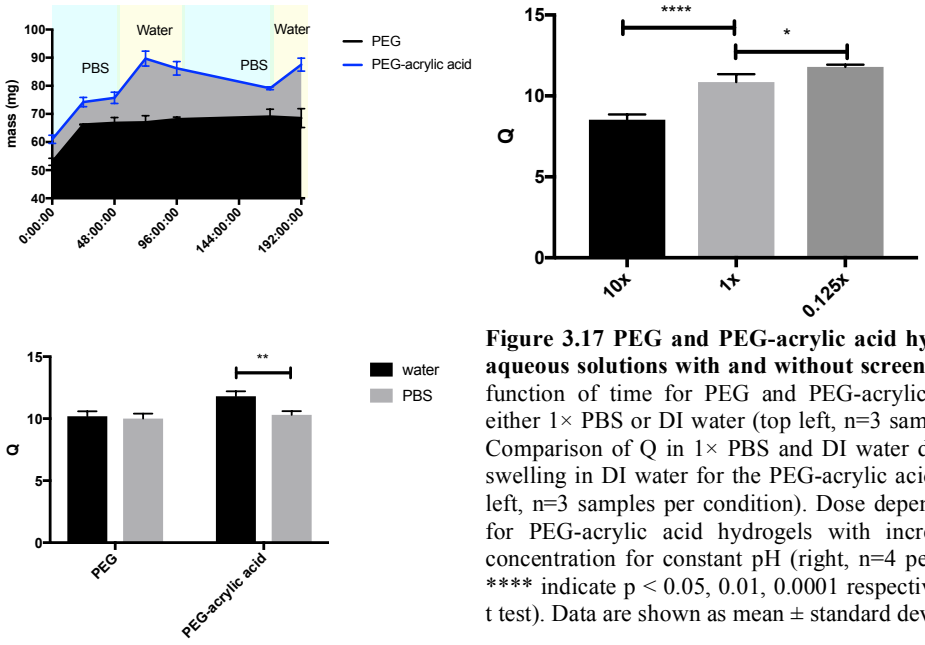

Figure 3.17 PEG and PEG-acrylic acid hydrogel swelling in aqueous solutions with and without screening ions. Mass as a function of time for PEG and PEG-acrylic acid hydrogels in either 1× PBS or DI water (top left, n=3 samples per condition). Comparison of Q in 1× PBS and DI water demonstrated higher swelling in DI water for the PEG-acrylic acid gels only (bottom left, n=3 samples per condition). Dose dependent decrease in Q for PEG-acrylic acid hydrogels with increasing PBS buffer concentration for constant pH (right, n=4 per condition). *, **, **** indicate $p < 0.05$, 0.01, 0.0001 respectively (determined by t test). Data are shown as mean ± standard deviation.

X. Summary

Taken together, the results from Chapter 3 demonstrate that we can use modeling of photodegradation as a function of film depth[100] and knowledge of polymer network swelling[51] to predict relative amounts of folding for photodegradable hydrogel films. The starting volume swelling ratios for the B, E and D *o*-NB group hydrogels (at 21.5 wt%) were about 11 (corresponding to a mesh size of approximately 58 Å; the modulus is approximately 20 kPa). Following photodegradation, at the highest 365 nm light exposure at 60 J/cm^2, we predicted that the exposed surface degrades to the full extent that it can (fraction of 0.37 intact network strands). If we assume that the exposed half of the gel can swell without being constrained by the higher crosslink side of the gel, we predict a volume swelling of 18-19 for this amount of photodegradation (corresponding to a mesh size of approximately 74 Å). However, the swelling will be limited, depending

on the elasticity of the opposite side of the hydrogel. We demonstrated in this chapter, how modulating the starting crosslink density and fraction of degradable to non-degradable network strands can change the amount of curvature. This knowledge can be used to guide future modulation experiments.

For cell and tissue culture applications, the hydrogel properties are often determined by the optimal substrate for the cells. For example, some cell types will prefer less or more highly cross-linked substrates.[59,104] With those constraints, we can tune film thickness and/or select the appropriate photodegradable macromer with desired absorptivity and degradation kinetics for desired folding actuation wavelength and light dose. In this chapter we demonstrate how we can adjust degradable:non-degradable polymer chain ratios, light dose and wavelength, total starting polymer weight percent, film thickness and/or select a photodegradable moiety for desired molar absorptivity and kinetic rate constant of degradation to tune light dose required for folding. In Chapter 4, we will discuss how folding geometry can be tuned to create shapes with positive, negative and mixed curvatures from an originally homogenous hydrogel.

XI. Experimental

Materials

Acetovanillone (Acros, 98%), potassium carbonate (Fisher, 99%), dimethylformamide (DMF) (Fisher > 99.8%), ethyl 4-bromobutyrate (Alfa Aesar, 98%), nitric acid (EMD Millipore, 70%), trifluoroacetic acid (Fisher, ≥99.5%), ethanol (Decon Laboratories, 200 proof), sodium borohydride (Acros, 98%), 1-(3-dimethylaminopropyl)-3-ethylcarbodiimide (Alfa Aesar, 98%), 4-(dimethylamino)pyridine (Alfa Aesar, 99%), poly(ethylene glycol) (PEG) 4000 (Mallinckrodt, 98%), ammonium persulfate (Amresco,

98%), tetramethylethylenediamine (TEMED) (OmniPur, 99%) were used as purchased. Dichloromethane (Fisher, ≥99.5%) was distilled from calcium hydride and stored over activated molecular sieves. Triethylamine (Fisher, 99%) was distilled under Ar and stored over potassium hydroxide pellets under Ar. Acryloyl chloride (Alfa Aesar, 98%) was distilled under Ar and stored under Ar in a dry, air-free flask.

Macromer Synthesis

The acrylated B, D and E *o*-NB moleculues (i.e. 4-(4-(1-(acryloyloxy)ethyl)-2-methoxy-5-nitrophenoxy)butanoic acid, 4-(3-(1-acrloyloxyethyl)-4-nitrophenoxy) butanoic acid, and 4-(3-(acryloyloxymethyl)-2-nitrobenzyloxy)-4-oxobutanoic acid were synthesized as described previously.[36-37] The PEG 3350 B group macromer (PEG 3350 4-(4-(1-(acryloyloxy)ethyl)-2-methoxy-5-nitrophenoxy)butanoate was synthesized by suspending 4-(4-(1-(acryloyloxy)ethyl)-2-methoxy-5-nitrophenoxy)butanoic acid (0.9 g, 2.54 mmol) in dichloromethane (61 ml) in a 250 ml round bottom flask. 1-(3-dimethylaminopropyl)-3-ethylcarbodiimide, 98% (447 µl, 2.54 mmol) and 4-(dimethylamino)pyridine, 99% (42 mg, 0.34 mmol) were reacted under Ar for 15-minutes. PEG 3350 (2.8 g, 0.85 mmol) was added and reacted under Ar overnight. The macromer solution was washed with concentrated salt-water and precipitated in chilled diethyl ether (290 ml). The precipitate was dried overnight by reduced pressure to yield a pale yellow powder (2.6 g, 76%). ^{1}H NMR ($CDCl_3$, ppm): δ=7.62 (s, 1.06H), 7.00 (s, 0.99H), 6.55 (m, 1.04H), 6.45 (d, 0.99H), 6.15 (m, 0.96H), 5.99 (d, 0.96H), 4.25 (t, 2.06H), 4.15 (t, 2.30H), 3.95 (s, 3.39H), 3.70-3.55 (m, 185.66H), 2.57 (t, 2.01H), 2.20 (m, 2.42H), 1.68 (d, 3.19H). PEG 4000 B group macromer (PEG 4000 4-(4-(1-(acryloyloxy)ethyl)-2-methoxy-5-nitrophenoxy)butanoate) was synthesized similarly, as

described in Ref. 1. The D group macromer (PEG 3350 4-(3-(1-acrloyloxyethyl)-4-nitrophenoxy) butanoate) was synthesized by suspending 4-(3-(1-acrloyloxyethyl)-4-nitrophenoxy) butanoic acid (0.9 g, 2.73 mmol) in dichloromethane (60 ml) in a 100 ml round bottom flask. 1-(3-dimethylaminopropyl)-3-ethylcarbodiimide, 98% (490 μl, 2.73 mmol) and 4-(dimethylamino)pyridine, 99% (45 mg, 0.36 mmol) were reacted under Ar for 15 minutes. PEG 3350 (3.0 g, 0.91 mmol) was added and reacted under Ar overnight. The macromer solution was washed with concentrated salt-water and precipitated in chilled diethyl ether (300 ml). The precipitate was dried overnight by reduced pressure to yield a pale yellow powder (2.8 g, 78%). ^{1}H NMR ($CDCl_3$, ppm) δ=8.11 (d, 1H), 7.05 (s, 0.99H), 6.86 (d, 1.04H), 6.49-6.52 (m, 2.00H), 6.21 (m, 0.98H), 5.94 (d, 0.98H), 4.25 (t, 2.12H), 4.18 (t, 2.37H), 3.25-3.10 (m, 179.71H), 2.62 (t, 2.06H), 2.17 (m, 2.66H), 1.60 (d, 3.14H). The E group macromer (PEG 3350 4-(3-(acryloyloxymethyl)-2-nitrobenzyloxy)-4-oxobutanoate) was synthesized by suspending 4-(3-(acryloyloxymethyl)-2-nitrobenzyloxy)-4-oxobutanoic acid (0.5 g, 1.61 mmol) in dichloromethane (36 ml) in a 100 ml round bottom flask. 1-(3-dimethylaminopropyl)-3-ethylcarbodiimide, 98% (290 μl, 1.61 mmol) and 4-(dimethylamino)pyridine, 99% (27 mg, 0.22 mmol) were reacted under Ar for 15 minutes. PEG 3350 (1.8 g, 0.54 mmol) was added and reacted under Ar overnight. The macromer solution was washed with concentrated salt-water and precipitated in chilled diethyl ether (180 ml). The precipitate was dried overnight by reduced pressure to yield a white powder (1.5 g, 69%). ^{1}H NMR ($CDCl_3$, ppm): δ=7.60 (m, 7.06H), 6.49 (d, 2.05H), 6.18 (m, 2.23H), 5.92 (d, 2.13H), 5.39 (s, 4.25H), 5.33 (s, 4.30H), 3.80-3.55 (m, 440.6H), 2.63 (s, 9.36H)

PEG diacrylate (PEGDA) was synthesized by suspending PEG 4000 (10 g, 2.5 mmol) in dichloromethane (50 mL). Triethylamine (1.7 mL, 12.5 mmol) was added under Ar. Acryloyl chloride (850 μL, 10 mmol) was diluted in dichloromethane (20 mL) and added to the PEG suspension dropwise. The reaction proceeded under Ar overnight. The solution was concentrated by rotary evaporation and acetone was added to precipitate triethylamine salts. The salts were filtered and the eluent was precipitated in 1 L chilled diethyl ether. The precipitate was dried overnight by reduced pressure to yield a white powder (9.5 g, 92%). ^{1}H NMR ($CDCl_3$, ppm): δ=6.50 (d, 2H), 6.20 (m, 2H), 5.82 (d, 2H), 4.25 (t, 4H), 3.70-3.55 (m, 320H).

Photodegradable hydrogel casting and UV degradation for effect of PDM:PEGDA ratio and light dose effects on folding

Partially photodegradable hydrogels were co-polymerized in 1× PBS using PEG 4000 B *o*-NB photodegradable macromer (PDM) and PEG 4000 diacrylate (PEGDA). The hydrogels were polymerized by radical polymerization using APS and TEMED. The pre-gel solution containing 21.5% (w/w) of PDM and PEGDA combined was quickly pipetted in between glass slides separated by No. 1 coverslip spacers (150 μm) and allowed to gel for 30 minutes. Samples were punched using a 4 mm × 4 mm square leather punch or a 4 mm diameter biopsy punch. The thin hydrogel sheet was equilibrated in PBS and then exposed to collimated UV light (365 nm) from one side. Following exposure, hydrogels were immediately transferred to a PBS bath for free swelling and imaging. The gels were imaged at 10 minutes and 1 day later. Images were captured using a digital camera (Olympus E-PL6).

Photodegradable hydrogel casting and UV degradation for effect of molar absorptivity and rate constant of degradation on folding

The respective PEG 3350 B, D or E- *o*-NB macromer (22.5 mg) was dissolved with PEGDA (10 mg) in PBS (95 μl). The solutions were centrifuged for 5 minutes at 8k RPM to remove air bubbles. Next 7.5 μl each of 1.0 M APS solution and 0.5 M TEMED solution were added for final concentrations of 50 and 25 mM respectively. The solutions were mixed well by vortexing and 45 μl droplets were pipet on to glass slides between 150 μm spacers. A coverslip was placed on top of the solution resulting in 150 μm tall thin films before equilibration in PBS. The solutions were allowed 15 minutes to gel and then transferred to 6-well plates with about 8 ml PBS per well. The PBS was exchanged 3× and then placed on a shaker plate overnight. The following day, the solution was changed 2 more times before proceeding with the exposures.

The hydrogels were partially degraded using long-wave UV light exposures (365 nm) for 600 s. Thin films of up to 20 mm width were exposed in PBS on a glass slide covered with a 25 mm x 25 mm coverslip at 30, 70, or 100 mW/cm^2 (18, 42, or 60 J/cm^2 respectively). Following exposure, 4 mm diameter discs were punched and immediately transferred to a PBS bath for free swelling and imaging. The gels were also imaged 1 day later. For each condition 4-8 samples were imaged and measured. Images were captured using a macro lens (Micro-Nikkor 55 mm f/2.8) attached to a digital camera (Olympus E-PL6).

Equilibrium volume swelling ratio for different macromer (B, E and D) hydrogels

Partially degradable PEG *o*-NB gels were prepared using the PEG 3350 B, E and D *o*-NB macromers. Hydrogels were prepared using a 2:1 molar ratio of *o*-NB to PEG

3350 diacrylate at 21.5 total polymer wt%. The macromers were dissolved in PBS and 1.0 M APS and 0.5 M TEMED were added resulting in final concentrations of 100 and 50 mM respectively. The hydrogels were cast in poly(dimethylsiloxane) (PDMS) molds of 5 mm diameter and 3 mm height. In order to ensure even heights, the molds were overfilled and then pressed between glass slides. The gels were polymerized at ambient conditions (23 °C) for 15 minutes.

For the swell ratio calculations, the mass of individual hydrogels was measured immediately after releasing from molds, at 3 h, 24 h, 48 h, and 72 h. The gels were freeze-dried after 72 h and the dry mass was measured. Because the gels were swollen in PBS, the salt mass was accounted for, by taking the water weight to be the difference between the swollen and the dry weight and knowing that 1x PBS has salt concentration of 10.22 mg/ml. The mass swelling ratio, q was calculated:

$$q = M_s/M_d = (W_s - W_d)/W_d \quad \textbf{(19)}$$

where M_s and M_d are the solvent (water) and dry polymer masses respectively and W_s and W_d are the swollen and dry network weights. The volumetric swelling ratio (Q_m) was then calculated using:

$$Q_m = 1 + q\,(\rho_2/\rho_1) \quad \textbf{(20)}$$

and a polymer density value (ρ_2) of 1.12 g/ml for PEG and water density (ρ_1) of 1.00 g/ml.

Degradation depth determined by change in contrast of degraded o-NB

The degraded *o*-NB products have a difference in absorptivity compared to the non-degraded group. Because of this, there is a change in color for all three groups upon photodegradation. We utilized this feature to determine the depth of degradation in

optically thick, 1 mm gels. Hydrogels were prepared with the B, E and D groups at 22.8 wt% as described for the folding experiments except that 1 mm spacers were used to prepare 1 mm thick gels. The hydrogels were equilibrated overnight in PBS and then exposed from the top at 365 nm or 405 nm. The 365 nm exposures were done at 30 and 70 mW/cm^2 for 600 s (18 and 42 J/cm^2 exposures respectively). The 405 nm exposure was done at 30 mW/cm^2 for 600 s. The gels were then washed in PBS for at least 3 days to allow the degraded chains to diffuse out of the gel. Cross-sections were then imaged with a macro lens (Micro-Nikkor 55 mm f/2.8) attached to a digital camera (Olympus E-PL6). A plot of the linear grayscale intensity values was plotted for 3 line segments on each gel (2 gels per condition) using Fiji[105]. The FWHM was calculated to determine the "degradation depth".

Photodegradable hydrogels for comparing total polymer weight percent effect on folding as a function of a range of light doses at 365 nm

The 22.8% gels were prepared using the PEG 3350 D *o*-NB macromer (22.5 mg) dissolved with PEG 4000 diacrylate (PEGDA) (10 mg) in PBS (95 μl). The solutions were centrifuged at 8k RPM for 5 minutes to remove air bubbles. Next 7.5 μl each of the 1.0 M APS solution and 0.5 M TEMED solution were added for final concentrations of 50 and 25 mM respectively. The solutions were mixed by vortexing and 45 μl droplets were pipet on to glass slides between 150 μm spacers. A coverslip was placed on top of the solution resulting in 150 μm thickness films (before equilibration in PBS). The 17% gels were prepared by dissolving 16.8 mg D *o*-NB macromer with 7.5 mg PEGDA in PBS (95 μl). The same APS and TEMED concentrations were used as for the 22.8% gels. Thin hydrogel films were equilibrated overnight and exposed the following day for 600 s

using 365 nm light for a range of irradiance values between 6-42 J/cm^2. Following exposure, 4 mm diameter discs were punched and immediately transferred to a PBS bath for free swelling and imaging. The gels were imaged 1 day later. For each condition, between 3 to 10 samples were imaged and measured. Images were captured using a macro lens (Micro-Nikkor 55 mm f/2.8) attached to a digital camera (Olympus E-PL6).

Photodegradable hydrogels for comparing thickness effect on folding as a function of a range of light doses at 365 nm

Partially degradable 22.8 wt% gels were prepared using the D *o*-NB macromer (22.5 mg) dissolved with PEG 4000 diacrylate (PEGDA) (10 mg) in PBS (95 μl). The solutions were centrifuged at 8k RPM for 5 minutes to remove air bubbles. Next 7.5 μl each of 1.0 M APS solution and 0.5 M TEMED solution were added for final concentrations of 50 and 25 mM respectively. The solutions were mixed well by vortexing and 45 μl droplets were pipet on to glass slides between either 100 or 150 μm spacers. A cover glass was placed on top of the solution resulting in 100 or 150 μm tall thin films respectively before equilibration in PBS. Thin hydrogel films were equilibrated overnight and exposed the following day using 365 nm light for 600 s. Following exposure, 4 mm diameter discs were punched and immediately transferred to a PBS bath for free swelling and imaging. The gels were imaged 1 day later. For each condition, between 3 to 10 samples were imaged and measured. Images were captured using a macro lens (Micro-Nikkor 55 mm f/2.8) attached to a digital camera (Olympus E-PL6).

Ionic strength effect on swelling and shape-change

The 21.5% gels were prepared using the B *o*-NB macromer (21 mg) dissolved with PEG 4000 diacrylate (PEGDA) (9.4 mg) in PBS (95 μl). The solutions were centrifuged at 8k RPM for 5 minutes to remove air bubbles. Next 7.5 μl each of 1.0 M APS solution and 0.5 M TEMED solution were added for final concentrations of 50 and 25 mM respectively. The solutions were mixed well by vortexing and pipet between two glass slides sandwiching 100 μm spacers. The solution was allowed 15 minutes to polymerize and then equilibrated in PBS overnight.

The hydrogels were partially degraded using long-wave UV light exposures (365 nm) for 300 s. Thin films of up to 20 mm width were exposed in PBS on a glass slide covered with a 25 mm x 25 mm glass coverslip at 10 or 40 mW/cm^2 (3 or 12 J/cm^2 respectively). Following exposure, 10×10 mm squares were punched and immediately transferred to a PBS bath for free swelling. The gels were imaged 1 day later in both 1× PBS and DI water. Three samples were imaged per condition. The cross-sectional width was determined by measuring the widest width of the folded gel's inner lumen.

Ionic strength effect on swelling for PEG and PEG-acrylic acid hydrogels

We prepared PEG and PEG-acrylic hydrogels using PEG 4000 diacrylate (PEGDA). The PEG gels were prepared at 15% w/w in 1× PBS using 25 and 12.5 mM APS and TEMED respectively. Specifically, 33.8 mg PEGDA was dissolved in 179.8 μl 1× PBS, pH=7.4 (referred to as PBS from here on). Then 5.7 μl of 0.5 M TEMED was added to the PEG solution and mixed by vortexing, followed by addition of equal volume of 1.0 M APS. The solution was mixed well by pipetting repeatedly and then pipetting into 3 mm tall, 5 mm diameter PDMS molds. The PEG-acrylic acid gels were prepared

by dissolving 33.8 mg PEGDA in 167.3 μl PBS. Next, an acrylic acid (AA) solution was prepared by dissolving 144 μl AA in 356 μl PBS (288 μl/ml) and 1 μl of the AA solution was added to the PEGDA solution in PBS (giving 83% PEGDA acrylates and 17% AA acrylates in solution.) To polymerize the PEG-acrylic acid gels, 11.4 μl of 1.0 M APS and 0.5 M TEMED each were added to final concentrations of 50 and 25 mM respectively. The macromer was also polymerized in 3 mm tall, 5 mm diameter PDMS molds. The PEG and PEG-acrylic acid gels were polymerized for 15 minutes and then equilibrated in PBS overnight.

The mass immediately after the 15 minutes polymerization time was measured and after 24 and 48 hours in PBS. After 48 hours in PBS, the gels were switched over to DI water (pH 7), and washed 3× with water. The following day (72 h), the mass was measured and again at 96 h. Then after 48 h in water, the gels were switched back to PBS and washed 3×. The mass was measured the 3 days later (168 h). Finally, the gels were switched back to DI water and washed 3×. The mass was measured the following day (192 h). Following the last DI water measurement, the gels were freeze dried and the dry mass was measured to calculate the volume swelling ratio, Q (n=3 per condition).

PEG-acrylic acid gels (n=4) were prepared for swelling measurements in different ionic strength buffers the same way as above. The equilibrated mass was measured in 10×, 1× and 0.125× PBS buffer (pH=7.4). The dry mass was measured for the freeze-dried gels. Next the volume swelling ratio, Q, was calculated using equation **(20)** (accounting for the higher density of the 10× buffer of 1.1 compared to 1.0 for the 1× and 0.125× PBS buffers.)

Image analysis

Images were analyzed using GIMP 2.8 software to measure the inner cross-sectional width of at least 3 samples per condition. A Matlab GUI was developed to calculate the radius of curvature, inner and outer arc path lengths (C_b and C_t) and closure angle. To measure the radius of curvature of the inner surface, several points (> 9) were selected in the image along the inner surface of the gel. The points were then fit to a circle function and the circle radius was reported. To determine C_b and C_t of the curved gel, > 9 points were selected along the inner and outer surfaces, respectively, and fit to spline functions. The arc lengths between the two end points of the fitted spline functions were subsequently calculated. Using a spline function to fit the surfaces, rather than fitting to a circle, gave more accurate results for the arc length calculation. The closure angle was calculated by treating the inner edge of the gel as an arc. Three points were selected at the left most edge, the vertex (at the point on the arc where the tangential slope was equal to zero) and the right most edge of the inner surface (or top) of the gel. For perfectly flat gels the closure angle is 180° and for folded gels with overlapping opposing ends the closure angle is 0°. For all parameters, averages and standard deviations were calculated using Excel (Microsoft®). The values were used to compare conditions using t test, where indicated. T tests were run using GraphPad Prism Version 7.0. Two conditions were compared individually, without assuming equal standard deviations. Significant p values were further investigated and calculated using two-stage step-up method of Benjamini, Krieger and Yekutieli.

Modeling degradation

Extent of photodegradation was calculated using a model developed by Norris et al.,[100] which accounts for the diffusion of degraded photoabsorbing species through a hydrogel network bounded on the top and bottom surfaces (Neumann condition). The fraction of intact network strands was calculated using MATLAB and previously determined values for kinetic rate and molar absorptivity.[37]

Chapter 4

Patterning arbitrary curvatures and shapes for mimicking tissue geometries observed during morphogenesis and development

I. Control over folding geometry and curvatures for mimicking tissue geometries

We reported parameters for tuning the amount of photodegradable hydrogel bending in Chapter 3. We next sought to study the bending direction of 2D sheets with different geometries as well as to demonstrate control over arbitrary curvatures by using different photomasks to pattern in-plane swelling differences. The objective of this chapter is to demonstrate the creation of biologically relevant 3D shapes, with control over mean and Gaussian curvatures, using photodegradable hydrogels.

II. Developable surfaces: Hollow cylindrical shapes

Straight hollow tubes

Hollow tubes are ubiquitous in our tissue architecture as well as in nature. In our own bodies, blood vessels are formed of hollow tubes, allowing flow of nutrients, gas exchange and waste removal. Our digestive tract is also made up of hollow organs connected by a series of hollow tubes. Other solid organs, such as skeletal muscle, often exhibit tubular morphologies. Transport of nutrients and gas exchange remains a challenge for tissue engineering, limiting the size of engineered solid tissues to less than 2 mm in the absence of vasculature.[106] Folding of thin film cell laden sheets to form hollow tubes enables the patterning of macro scale tissue-like structures into tubes, and other more complex geometries with 3D shape complexity, while permitting diffusion through < 1 mm distances. We thus sought to further characterize folding of 2D

rectangular hydrogel films in to hollow tubular shapes for potential tissue engineering applications.

In an effort to better predict folding morphologies of tubes derived from 2D rectangular sheets, we started off by determining the folding axis of thin sheets with different length: width (L:W) ratios. Photodegradable hydrogel films were prepared at 100 μm thickness and equilibrated overnight in PBS. The sheets were exposed at 365 nm from one side to generate a crosslink density gradient through the film depth. Following photodegradation, 10:1, 10:2.5, 10:5, and 10:10 mm:mm (L:W) ratio rectangles were cut. For the highest aspect ratio rectangles—10:1 and 10:2.5—we only observed short axis folding (Figure 4.1). At the 10:5 aspect ratio we observed a mixture of folding patterns. Most samples folded along the short axis, and fewer gels exhibited long-axis and diagonal folding (Figure 4.1). These results are in agreement with Smela and co-workers, who demonstrated that short-axis folding is the more energetically favorable folding direction for bilayers that can undergo free swelling immediately following actuation.[107] They demonstrated (mathematically and empirically) that given sufficiently high actuation strains in bilayers, the curvature along the long side of rectangles increases faster than it does on the short side. This results in preferential

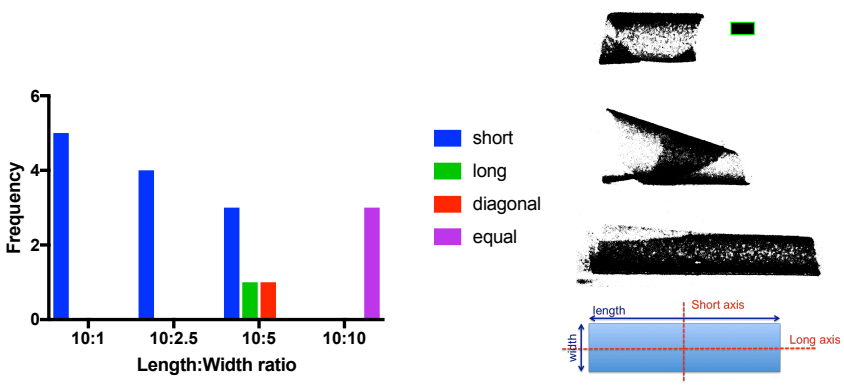

Figure 4.1 Aspect ratio effect on folding axis. The graph on the left represents the observed frequency of folding axis. The images on the right represent short, diagonal and long axis rolling (from top to bottom) observed with 10:5 aspect ratio gels. The scale bar is 1 mm. The schematic on the bottom right defines the folding axis terminology.

folding along the short-axis as actuation strain and (L:W) aspect ratio increase. Unlike the metal bilayer rods described by Timoshenko,[26] which only undergo uniaxial folding, thin films such as the hydrogels we describe here are free to bend in two dimensions. Therefore, under free swelling conditions, thin films will initially have dual curvature along both the x and y directions[108] forming a spherical[109] or lenticular shape[110] with positive Gaussian curvatures. At a critical actuation strain, biaxial bending becomes too costly due to the large amount of stretching required to generate positive Gaussian curvatures and uniaxial folding becomes more favorable.[111] Since the total length of the curled edge is greater for short- than for long-axis folding, at both increasing actuation strains and L:W ratios, the bi-directional bending gel transitions to a single curvature, typically along the short-axis. However, in the case of non-free swelling, when there is adhesion of the polymer film to an underlying substrate or in the case of anisotropic materials, different folding scenarios are observed such as those described by Ionov and coworkers.[13,112] Furthermore, we found that the folding axis, or rather the 2D sheet dimensions had no effect on the resulting mean curvatures. In the case of bilayers, the curvature has been shown to depend on the actuation strain, bilayer thickness and moduli but not the 2D sheet dimensions.[102,113]

In order to determine the effect of actuation strain on folding axis, we selected the intermediate aspect ratio (10:5 L:W) films and exposed them to a range of light doses. In Chapter 3 we demonstrated that the light dose affects the amount of curvature (which is a function of actuation strain) by affecting the depth of degradation through the hydrogel film. Intermediate aspect ratio films were exposed to 10, 20, or 40 mW/cm^2 light at 365 nm for 300 s (corresponding to 3, 6, or 12 J/cm^2 energies). In agreement with the

mathematical modeling predictions from Smela and co-workers, we observed a greater variety in folding patterns at the lowest actuation strain (3 J/cm^2) compared to the intermediate actuation strain (6 J/cm^2). Furthermore, we observed the greatest amount of long axis folding at the lowest light dose (Figure 4.2 top left). This result is in agreement with the predictions of Smela and colleagues, which suggest that at lower actuation strains, there is less difference in biaxial curvature compared to at high actuation strains. This results in less discrimination between long or short-axis folding so that once the critical bending moment is generated, the transitional curvature along the x- and y-directions differs little and there is more equal probability of either short or long axis folding. Instead, at high actuation strains, the curvature along the longer side increases markedly faster than along the shorter side resulting in preferential short-axis folding. However, at the highest light dose, 12 J/cm^2, we observed an increase in mixture of folding directions compared to the intermediate light dose. These observations may suggest that the maximum actuation strain occurred at < 12 J/cm^2, and higher light doses led to too much degradation and thus lower actuation strains. However, if this were the case, we would expect smaller curvatures and greater cross-sectional width for the 3 and 12 J/cm^2 light doses compared to 6 J/cm^2, which was not the case. Instead, we observed similar cross-sectional widths for all three light doses in PBS (Figure 4.2 bottom right) and decreasing cross-sectional width with increasing light dose in water (Figure 4.2 bottom left). We thus conclude that the light dose does not have a clear effect on folding direction with these hydrogels. This may be because the light dose does not directly affect the actuation strain. Instead, light dose has an effect on the final gradient distribution of degraded network strands through the gel and the resulting equilibrated

thickness. The degraded network gradient and resulting swelling differences are difficult to quantify and may affect the resulting actuation strain and folding direction.

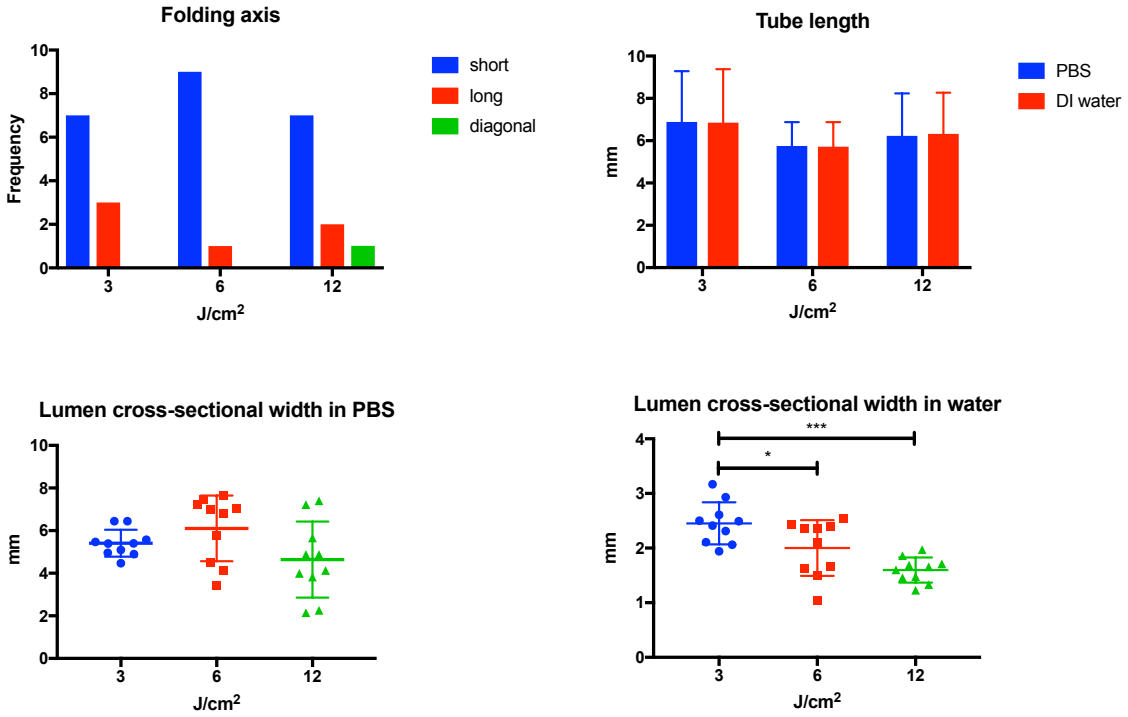

Figure 4.2 Effect of light dose on rectangular sheet folding. The top left graph represents the number of hydrogels that folded along the short, long or diagonal direction. The top left graph demonstrated the measured tube length at different light doses in PBS and DI water. The lumen cross-sectional width and length were also measured from images of the folded gels in PBS and DI water. The graphs on the bottom demonstrate the lumen cross-sectional width for increasing light dose as measured in PBS (left) and DI water (right) (n=10 per light dose condition, same sample was measured in PBS and DI water).

Next, we empirically determined whether patterning isotropic parallel beams along the long axis of rectangular hydrogels could predispose long vs.

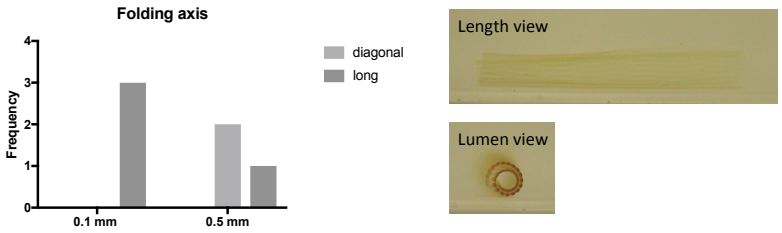

Figure 4.3 Folding direction for rectangular sheets patterned using parallel striped photomasks along the long axis promotes long axis folding. Thin parallel stripes of width less than hydrogel thickness are most effective at promoting long axis folding (left). Length and lumen view images of 100 μm thick rectangular sheet patterned from one side through 100 μm binary stripes (top right and bottom right respectively).

short axis folding. We again selected the intermediate aspect ratio (10:5 L:W) hydrogels to further explore folding axis. The samples were exposed to 20 mW/cm^2 light at 365 nm for 300 s (corresponding to 6 J/cm^2 energy) through a photomask with either 0.1 or 0.5 mm alternating opaque and transparent stripes aligned along the long axis of the rectangles. Following exposure, the samples were transferred to individual wells and imaged along the length and lumen views in both PBS and water after one day. The in-plane differential swelling along the long axis forced the 0.1 mm width striped gels to always bend along the long axis. The 0.5 mm striped gels folded along the long axis and diagonally (but never the short axis) (Figure 4.3, also see Figure 4.1 for illustration of folding axis). Samples exposed using the wide 0.5 mm stripes (width much greater than hydrogel thickness) had less folding and larger cross-sectional widths than samples exposed using thin stripes (width less than hydrogel thickness) (Figure 4.4). To consider only in-plane swelling effects on folding, we can approximate the folded gel sheet as a non-Euclidean plate with no swelling differential across the thickness, referring to the qualitative approximation of curvature by Wu et al[88] for radius of curvature. They predict radius of curvature by a minimization of the stretching and bending energies along the x-y plane, assuming that the bending energy is fully described by the high crosslink density regions and all the stretching energy is derived from the low crosslink density regions such that

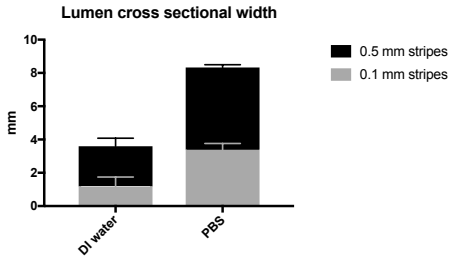

Figure 4.4 Lumen cross-sectional width for rectangular sheets patterned using parallel stripes along the sheets' long axis in water and PBS (n=3 samples per stripe width condition, same samples measured in PBS and DI water)

$$\rho^2 \approx \frac{w_s^2}{8\Delta f} + \gamma^2 \tilde{E} \frac{w_b}{8w_s}\left(\frac{1+\Delta f}{\Delta f^2}\right) \quad \textbf{(21)}$$

where w_s is the width of the more swollen, low crosslink density regions (photodegraded stripes in this case), w_b is the width of the bending, high crosslink density regions (non-degraded stripes), Δf is the difference in the linear extension of the two regions normalized to the low swelling region, γ is the sheet thickness and $\tilde{E}$ is the ratio of the moduli of high to low crosslink density regions. For this experiment we set values to those listed in Table 4.1.

Table 4.1. Values used to calculate change in curvature as a function of stripe width

w_s	Stretching region width	0.1 or 0.5 mm
w_b	Bending region width	0.1 or 0.5 mm
f_s	Linear extension due to swelling for stretching region	14.3^1/3 = 2.43 mm
f_b	Linear extension due to swelling for bending region	10.8^1/3 = 2.21 mm
Δf	$(f_s - f_b)/ f_b$	0.10 mm
γ	Sheet thickness	0.12 mm
$\tilde{E}$	Ratio of the elastic moduli for bending and stretching regions	1.59

We used an average value for the swelling of the degraded regions calculated using the average number of intact network strands through the hydrogel thickness to predict Δf and $\tilde{E}$. With these values, we can approximate the radius and diameter of the gels patterned with the 0.5 mm stripes to be 1.4× greater than for the 0.1 mm stripes. A plot of the predicted diameter as a function of stripe or bar width demonstrates that the curvature resulting from purely in-plane swelling differential remains fairly constant for $w_s = w_b \leq \gamma$ (Figure 4.5).

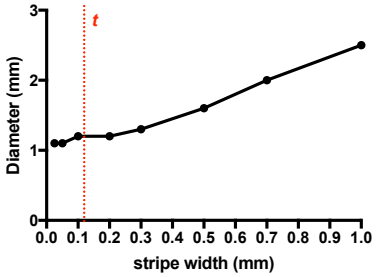

Figure 4.5 Calculated folded diameter as a function of stripe width. The effect of stripe width relative to gel thickness, *t* is demonstrated where diameter is fairly constant for stripe width ≤ t

In fact, the diameter only starts to appreciably increase when $w_s = w_b \geq 5\gamma$ suggesting that there is no benefit to using stripe widths less than the gel thickness, which in our case is typically between 100-200 μm.

Finally, we prepared "L-shaped" thin films with different leg aspect ratios to determine the folding direction for shapes with mixed aspect ratios. We again observed a preference for short axis bending for high aspect ratios. The L-shapes with high aspect ratio legs (e.g., 3.5:1, 5:1, 7.5:1), on either end, experienced helical folding along an angle oblique to the short axis (Figure 4.6 columns 3 & 4). The opposing swelling induced stretching along the leading x- and y-edges results in the opposite ends spiraling towards the vertex. Here, the bi-directional stress at the square vertex region generates diagonally oriented bending resulting in oblique bending direction at either of the legs as opposed to the predicted short axis rolling for a simple rectangle. This bending direction at the opposing ends permits a diagonally oriented curvature at the vertex. Thus, the differential swelling induced stress is relieved through bending at the vertex as opposed to along the edges alone. This obliquely oriented helical folding from both ends results in a dog-leg bend at the vertex, reminiscent of the sharp turns in transient looping morphogenesis such as in the heart (Figure 4.17) or intestine (Figure 4.14). Instead, asymmetric L-shapes with mixed low and high aspect ratio legs (e.g., 5:1 on one side and 2:1 on the other side) experienced helical folding oblique to the short axis along the high aspect ratio end, met by long axis folding on the low aspect ratio end. The resulting curved tube also had a dog-leg bend at the vertex (Figure 4.6 second row in columns 1 & 2). Furthermore, the small aspect ratio L-shapes (2:1) experienced mixed long and short-axis folding resulting in straight tubes where one tube wrapped around another (Figure

4.6 first row in columns 1 & 2). The same small aspect ratio L-shapes could instead be patterned with stripes oriented at oblique angles in order to return to uniaxial tubular bending (Figure 4.6 third row in columns 1 & 2).

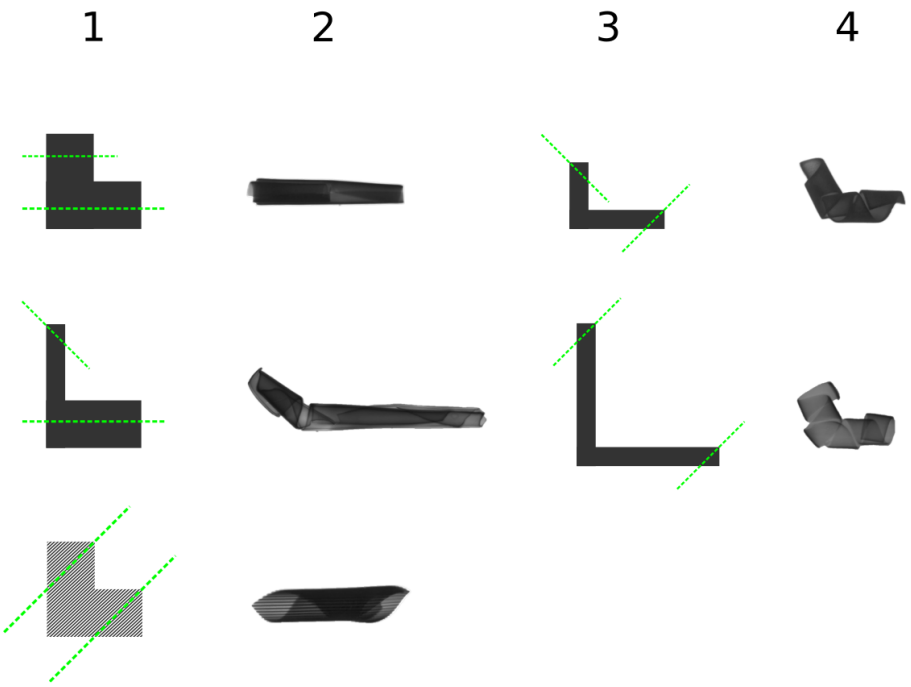

Figure 4.6 Differential swelling induced folding of L-shape gels with different aspect ratios. The shapes in columns 1 and 3 are schematic drawings. The resulting folding axes for the folded shapes in columns 2 and 4 are shown in green. From top to bottom the shapes in column 1 have: 10×5 mm (length×width) on either leg, 13×2 mm and 10×5 mm leg and 10×5 mm on either leg with stripes patterned parallel to the dashed green lines. From top to bottom the shapes in column 3 have: 7×2 mm and 10×2 mm legs, and 15×2 mm on either leg.

Helices

Helical looping of hollow tubular shapes can be observed in the small intestine, where looping extends the surface area while still allowing the intestine to fit in to the volume of the body cavity. This has the result of maximizing nutrient absorption.[114] Tabin and co-workers demonstrated that the development of the counterclockwise direction of the gut coiling results from left-right asymmetries in the dorsal mesentery (i.e., ECM volume, ECM stiffness and cell:cell adhesion asymmetries) using combined

embryonic tissue biometry and computational modeling.[4] They later demonstrated a reproducible looping pattern using an elastic rubber tube to mimic the small intestine and a soft latex sheet to mimic the mesentery. This demonstrated that gut looping could be reproduced using elastic polymeric materials under compression or tension respectively.[5] While this study was the first to demonstrate the biophysical basis for gut looping, there remains a paucity of studies demonstrating in vitro culture of intestinal and other complex shaped tissues in appropriate 3D morphologies, largely due to the absence of suitable scaffolds and standard tissue culture processes. One of the first examples of intestine endothelial cell culture in a 3D morphology came out of Mimetas from Vulto and co-workers when they cultured Caco-2 cells in leak-tight tubules on an Organ-on-a-Chip platform.[115] This was the first account of the recapitulation of both the integrity of leak-tight endothelial cells in tubular morphologies—reminiscent of small intestine tubes—as well as the sensitivity to detect drug-induced loss of barrier integrity that could not be detected using standard 2D cell culture techniques. With an appreciation for the relationship between the ECM on gut looping morphogenesis as well as evidence supporting the importance of reproducing 3D morphologies for recapitulating cell function in vitro, we sought to further study helical folding of photodegradable hydrogel sheets that can be used as cell culture scaffolds.

Shape changing hydrogels are attractive materials for cell culture due to their ability to mimic the ECM and to undergo large amounts of swelling in aqueous solutions. The use of in-plane swelling differences to generate looping hydrogels was reported by Kumacheva and co-workers.[88] The group used binary hydrogel sheets patterned at oblique angle to the long axis. The two polymers underwent differences in swelling in

response to ionic strength and temperature changes, resulting in transitions from flat 2D sheets to folded 3D looping helices. Because the sheets only experienced differences in in-plane swelling and not along the sheet thickness, the spirals had equal probability of clockwise or counter-clockwise looping or handedness. Folding resulted purely due to in-plane swelling differences that led to out of plane buckling and because the stripes were at an oblique angle relative to the strip length, looping resulted. The minimization of energy for the stretching and bending regions resulted in an approximation of the helix radius given in equation (**21**), which is primarily a function of the stripe widths, the differences in swelling between the binary hydrogel sections and the sheet thickness. Hydrogels with modulations in in-plane strain only are distinct from sheets with inhomogeneities through the sheet depth. Armon et al. studied the latter by describing the mechanics of *Bauhinia variegate* seedpod opening. They showed that two fibrous layers under tension at oblique angles result in helical bending until the pods eventually burst open and release their seeds.[77] They also created latex sheet bilayer analogs of the seedpods. The layers were stretched perpendicular to one another, glued together and then strips were cut at oblique angles. They demonstrated with both the seedpods and the latex analogs that the resulting shape depended on the width of the strips such that wide strips formed cylindrical helices (approaching a tubular configuration with zero Gaussian curvature) where as narrow strips adopted a twisted configuration (non-zero Gaussian curvature). They demonstrated that there was a critical width at which the radius of the helix approached 0 and there was pure twisting. The dimensionless width was calculated as $\widetilde{w} = w\sqrt{\frac{\kappa_0}{\gamma}}$ where w is the strip width, κ_0 is the curvature and γ is strip thickness. The critical width was found to be $\widetilde{w} < w_{crit} \approx 2.5$. Furthermore, because the stretching

energy scales like $\gamma w(\kappa_0 w)^4$ and the bending energy scales like $\gamma^3 w\kappa_0^2$, in this case, we qualitatively expect stretching dominated shape-change for large *w* and bending dominated twisting for small *w*. While Armon et al. demonstrated that differences in 2D sheet geometry affected looping morphology of bilayers with obliquely oriented stresses; they could not modulate the in-plane strain in their system. We thus became interested in interrogating the effect of 2D sheet geometry on helical looping in our photodegradable hydrogel system. We hypothesized that we could generate helical looping by photopatterning in-plane modulations—similar to the Kumacheva group system[87,88]—in our photodegradable hydrogels.

Using PEG *o*-NB photodegradable hydrogels, we demonstrate the ability to fold flat sheets into helices by using photomasks with binary stripes oriented at an angle relative to the long axis of rectangular sheets. This resulted in patterning of in-plane swelling differences along the x-y plane of 100 μm thick hydrogels. Due to the high light attenuation coefficient of the B group (defined in Ref. [37] and Chapter 3) at 365 nm, our system is distinct from the Kumacheva group's, which had no differences in swelling through the sheet thickness. We expected that the resulting helical looping hydrogels would have characteristic shape features including number of turns (*N*), pitch (*p*) and lumen cross-sectional width that could be controlled using combined in-plane and out-of-plane swelling differences (Figure 4.7).

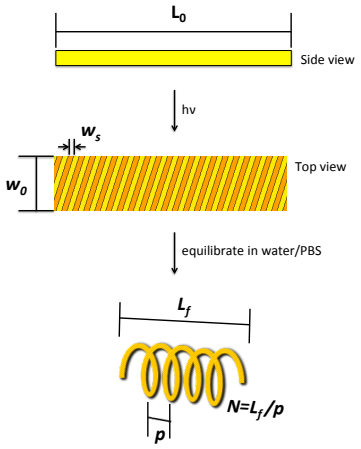

Figure 4.7 Photopatterning rectangular sheets with stripes at oblique angle to long axis results in helical folding following equilibration in aqueous solutions.

Hydrogel sheets were prepared with different

lengths and length:width (L:W) ratios to study the effect of planar sheet geometries on folding. Sheets were prepared at 10, 15, or 20 mm lengths with 10:1, 4:1, or 2:1 L:W ratios. The sheets were patterned using binary 0.5 mm wide stripes at a 60° angle relative to the long axis. Following photodegradation using 365 nm light at 9 J/cm^2, the gels were cut to the respective dimensions and then equilibrated in water.

We found that N was not affected by the L:W ratio but it was affected by the length—with an increase in N with increasing length (Figure 4.8 top left). Furthermore, the helix pitch, p, decreased with increasing L:W ratio and remained fairly constant for different length sheets (Figure 4.8, top right). Therefore, for constant L:W ratio, the pitch remains fairly constant, yet the number of turns increases as a function of flat 2D rectangular length, L_0 (defined in Figure 4.7). These results suggest that the 3D folded helix length, L_f behaves differently depending on the L:W ratio. A plot of L_f as a function of L:W ratio demonstrates a rapid decrease for increasing ratios. To determine whether the change in L_f is independent of the flat 2D length before folding, L_0, we normalized L_f

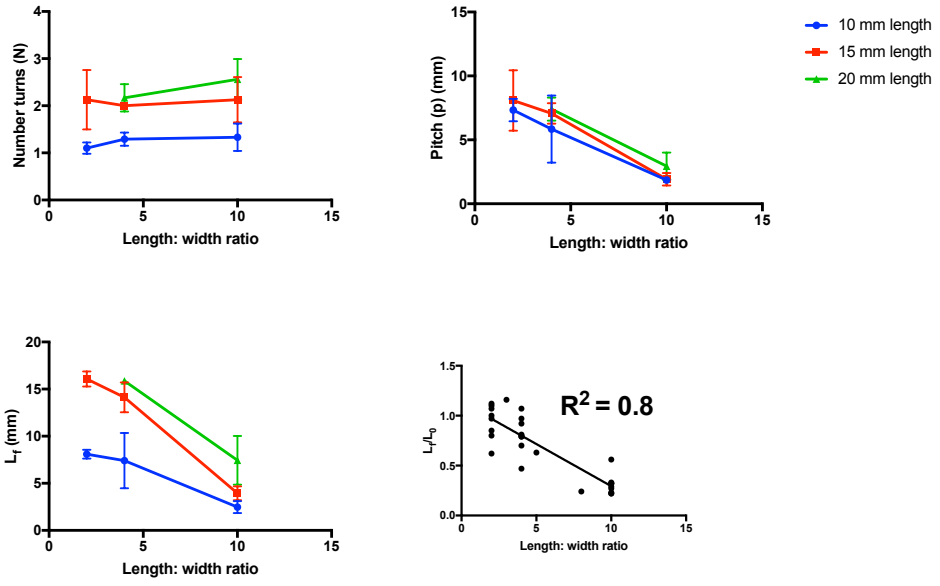

Figure 4.8 Helix characterization parameters *N*, *p* and L_f as a function of length: width ratio (top left, top right and bottom left respectively, n=3-4 samples per condition). The legend in top right applies to left graphs as well.

to L_0 and plotted it as a function of the L:W ratio. We can see the tendency towards short axis folding for the high aspect ratio (10:1) gels where the L_f/L_0 seems to converge for all three starting lengths, L_0. The values start to diverge more so at lower aspect ratios. These results agree with our no-stripe, or flood irradiation, data where the high aspect ratio rectangles had the strongest tendency to fold along the short axis.

Here we observe this again for rectangles patterned with parallel stripes at an oblique angle. The folding direction approached short axis folding for the high aspect ratio gels. The lower aspect ratio (4:1 and 2:1) gels tended to approach diagonal to long-axis rolling. For a given length, L_0, the binary change in swelling across the (longer) x-axis was constant regardless of the L:W ratio. However, with increasing L:W ratio, the differential swelling along the (shorter) y-axis decreased due to the smaller relative width. There fore, high aspect ratio gel folding was dominated by x-axis curvature due to (i) a greater curvature in the long x-axis compared to the short y-axis actuated by differences in swelling through the depth of the gel as described by Smela and co-workers[107] and (ii) more binary swelling modulations patterned along the x-axis compared to the y-axis. As the aspect ratio decreased, the swelling differences patterned along the y-axis increased, leading to increasing elongation and curvature in the y-axis relative to the x-axis. However, the film geometries that we used were such that the critical width from Armon et al., $w_{crit} \approx 2.5$, predicting pure bending and zero radius of curvature[77] was not reached—our minimum $\tilde{w}$ was approximately 3. Accordingly, we did not observe this type of folding in water. A separate analysis of 15 mm length by 1.5 mm width gels exposed to decreased photodegradation (365 nm, 6 J/cm^2) realized the bending dominated twisting phenotype in PBS but not in water. If we recall from Armon et al.,

increased thickness, decreased width and bending dominated shape-change favor twisting as opposed to cylindrical helices. Since in water, the degraded hydrogels swell more than in PBS, we retain stretching dominated cylindrical helices for the same rectangular sheet. While in PBS, we realize the critical bending dominated regime (Figure 4.9).

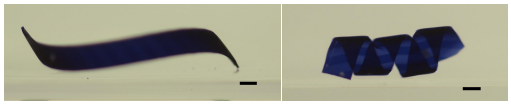

Figure 4.9. High aspect ratio sheet either twisting or helical looping in PBS or water. Rectangular sheet folding in to twisted (left) or cylindrical (right) helix in PBS or water respectively. The scale bars are 1 mm.

We next further analyzed the different aspect ratio groups to determine whether we could predict folded helix length, L_f, as a function of the stripe width, w_s, and number of stripes, n_s, along the x-axis. We treated the helices like folded polymer chains with number of stripes and stripe width being analogous to number and length of Kuhn segments[116,117] respectively. We plotted the L_f as a function of the number of stripes along the x-axis for each of the three aspect ratios. With the exception of one outlier, the 1:10 gels scaled approximately as $L_f = w_s n_s^{0.6}$. Instead the 1:4 gels scaled approximately as $L_f = w_s n_s^{0.9}$ and the 1:2 gels scaled as $L_f = w_s n_s^{1.0}$ (Figure 4.10). Thus, with decreasing aspect ratio, the L_f approached L_0. The high aspect ratio gels did not have purely short axis folding and stripes patterned at oblique angles always led to helical looping such that $L_f > w_0$.

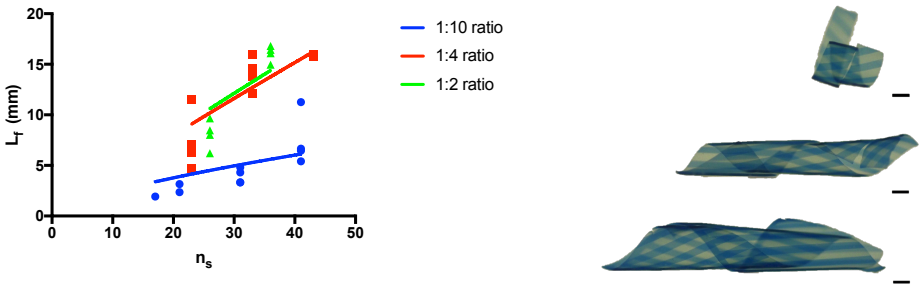

Figure 4.10. Modulation of folded length L_f as a function of the number of stripes across the long axis (x-axis) for different aspect ratio gels of 10, 15 and 20 mm lengths and 0.5 mm stripe widths. The 1:10 gels are dominated by short axis folding such that the increase in L_f with increasing length is much slower than for lower aspect ratio gels where the folding progressively tends towards long axis folding (left). Images of 15 mm length gels with 1:10, 1:4 and 1:2 aspect ratios from top to bottom (right). Scale bars are 1 mm.

Next we looked at the effect of the 2D sheet geometry dimensions on the folded 3D cross-sectional width. Similar to the observations with the flood irradiation (no x-y patterning), the cross-sectional width did not change appreciably as a function of L:W ratio when the samples were grouped by length or as a function of width when the samples were grouped by aspect ratio (Figure 4.11). Thus, the change in 2D sheet geometry did not affect actuation strain or radius of curvature in agreement with previous accounts.[113]

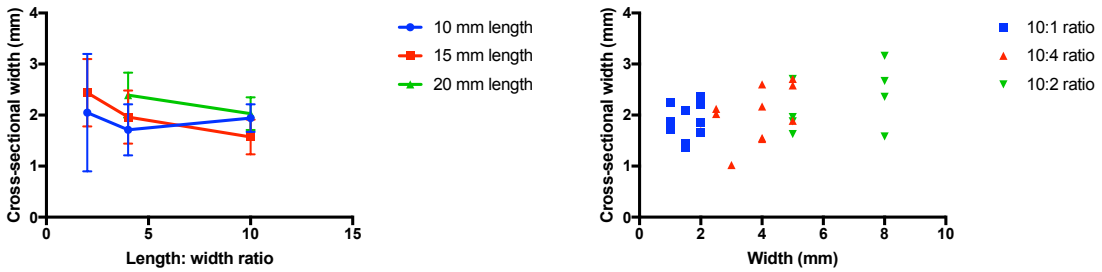

Figure 4.11 Lumen cross-sectional width as a function of length: width ratio or width. Averages are reported from 3-4 samples per condition with standard deviation error bars (left). The cross-sectional width remained fairly constant as a function of width (right).

Based on these results, we compiled a series of parameters to further test in order to better characterize 3D folding resulting from photodegradation. We previously observed a clear preference for looping handedness since all gels patterned at 60° angles relative to rectangle sheet long axis experienced clockwise looping. Furthermore, *N* was strongly affected by the 2D sheet length and not the L:W ratio, while the dominant folding axis and resulting *p* were both modulated depending on the L:W ratio. Furthermore, Kumacheva and colleagues demonstrated that modulating the stripe width affected the resulting 3D looping geometries. We therefore further studied the effect of stripe angle (± 60°) on helix handedness and the effect of stripe width for constant 2D sheet geometries to elucidate their isolated effects on 3D folding parameters (i.e. *N, p,* L_f and cross-sectional width).

Shape changing systems with swelling differences patterned in-plane (i.e. x-y direction) only, do not offer control over chirality or bending direction. Thus, there is an equally probable chance of clockwise or counterclockwise bending or twisting. Therefore the hydrogels reported by Wu et al. that were patterned with binary stripes with differences in swelling along the x-y direction only had both clockwise and counterclockwise looping.[88] Instead, Wei et al. described hydrogel sheets with polymer stripes with differences in swelling photopolymerized along the x-y direction and a bilayer with swelling differences along the z-direction. The combination of in-plane and through depth actuation strategies allowed for the design of reconfigurable shape-change and a wide array of folding directions that were not possible to achieve with either strategy alone.[118] Furthermore the combined in-plane and out-of-plane swelling actuated folding hydrogels exhibited control over chirality depending on the stripe angle with

respect to the long axis of the sheet. Similarly, our photodegradable hydrogels can be fabricated to exhibit both in-plane and out-of-plane swelling differences to actuate control over folding direction. We demonstrated this by patterning 15:1.5 mm (L:W) rectangular sheets with stripes oriented at ±60° relative to the sheets' long axis. The stripe width was 0.5 mm and the sheets were all patterned at 365 nm and 9 J/cm^2. Samples patterned at 60° relative to the sheets' long axis always underwent clockwise looping while samples patterned at -60°, always underwent counterclockwise looping (Figure 4.12). These results are in agreement with previously reported bilayers.[77,118]

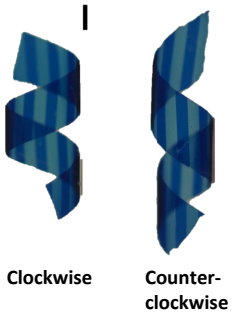

Figure 4.12 Demonstration of clockwise and counter-clockwise helix looping for ± 60° angle stripes relative to the long axis respectively. The scale bar is 1 mm

Wu et al. also studied the effect of stripe width on small-scale modulations in swelling differences in hybrid hydrogel sheets in the absence of differences in actuation strain along the z-axis.[88] They demonstrated the ability to modulate helix radius of curvature by changing binary polymer stripe widths. In a similar spirit, we again prepared 15:1.5 mm (L:W) rectangular sheets and patterned them at 365 nm and 9 J/cm^2 through binary stripes with widths of 0.5, 0.1 or 0.05 mm. We observed decreasing lumen cross-sectional width with decreasing stripe width. Furthermore, similar to the results with stripes patterned parallel to the long axis, there was more bending (and lower cross-sectional width) when samples were equilibrated in DI water compared to PBS. The difference was significant ($p < 0.05$) for the 0.5 and 0.1 mm stripes (Figure 4.13, top left). We observed no effect of solution ionic strength on the L_f. There was also no effect of stripe width on L_f. However, there was a trend towards decreasing N with increasing ionic

strength (i.e. PBS vs. DI water) and increasing *N* as stripe width decreased (Figure 4.13, top right). We thus see that *N* and lumen cross-sectional width respectively increase and decrease as a function of increasing actuation strain. We demonstrated this using both different ionic strength solutions as well as by modulating in-plane stripe width. We expect that light dose could also be used to modulate *N* and cross-sectional width. Instead, L_f did not change as a function of ionic strength or stripe width. We previously observed that modulating sheet geometry (L:W ratio) affected L_f due to preference for folding axis depending on the aspect ratio. Finally, the pitch was also modulated by changes in stripe width. Since the L_f did not change in DI water vs. PBS, while the *N* did, the pitch could be reversibly controlled in different buffer concentrations.

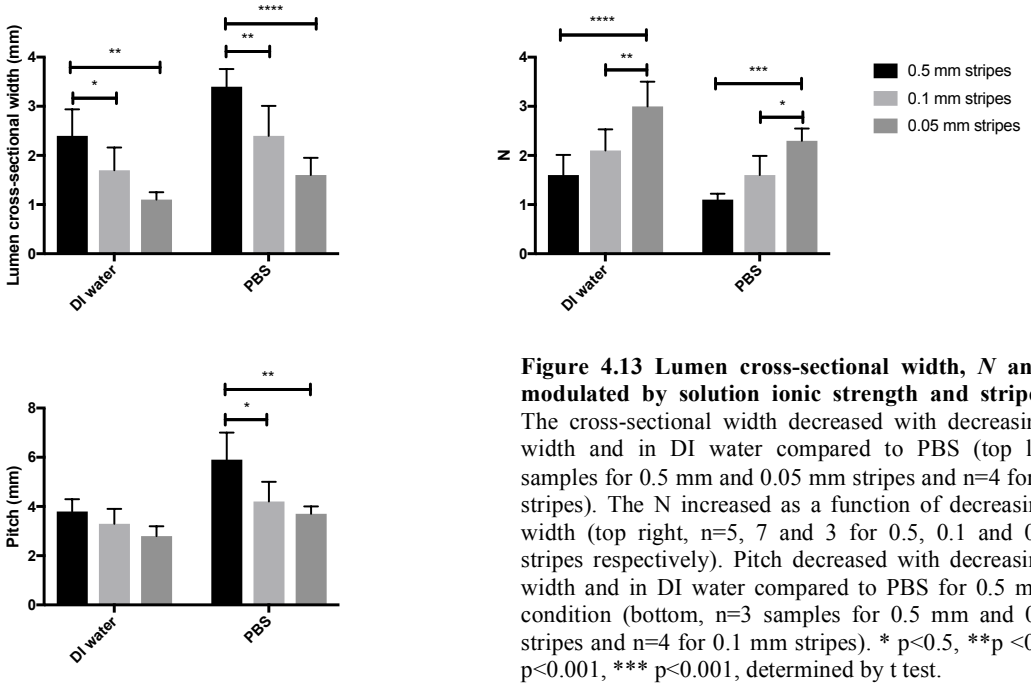

Figure 4.13 Lumen cross-sectional width, *N* and *p* are modulated by solution ionic strength and stripe width. The cross-sectional width decreased with decreasing stripe width and in DI water compared to PBS (top left, n=3 samples for 0.5 mm and 0.05 mm stripes and n=4 for 0.1 mm stripes). The N increased as a function of decreasing stripe width (top right, n=5, 7 and 3 for 0.5, 0.1 and 0.05 mm stripes respectively). Pitch decreased with decreasing stripe width and in DI water compared to PBS for 0.5 mm stripe condition (bottom, n=3 samples for 0.5 mm and 0.05 mm stripes and n=4 for 0.1 mm stripes). * p<0.5, **p <0.01, *** p<0.001, *** p<0.001, determined by t test.

Finally, we demonstrate the flexibility with which to pattern helices of arbitrary handedness or to ascribe inside-out looping on-demand, within the same sheet using the photodegradable system. The same design principles that were previously described were

used to predictably pattern originally flat, 2D sheets. We first demonstrate transitioning from clockwise to counterclockwise helix handedness by patterning rectangular sheets with 0.1 mm binary stripes. Stripes were oriented at +/- 60° angles from the longitudinal axis with mirror reflection symmetry on the left and right halves of the rectangular sheet respectively. The sheet thus folded with clockwise and counter clockwise helical looping on the left and right sides of the sheet respectively, in agreement with our previous observations with uniform patterning direction (Figure 4.12a). These shapes can mimic change in looping direction of the small intestine, for example, as depicted in Figure 4.14a with an image reconstruction of the looping direction transitioning from clockwise to counterclockwise directions. We next used the same angled binary stripes to pattern rectangular sheets from the top of the sheet on the left and the bottom of the sheet on the right half (Figure 4.14b). The 3D folded shape resulted in inside out turning as the more swollen, degraded "top" side formed the outer surface of the helix on the left, and transitioned in to the inner surface of the helix on the right side in the region where the bottom side had been UV-exposed. Such shapes are again relevant for small intestine tissue models. For example, patterning of left-right asymmetries has been shown to play a role in the looping of the small intestine during development. Asymmetric differences in mesenchymal cell compaction of the dorsal mesentery and changes in the respective neighboring epithelium morphology, from columnar to cuboidal, result in morphogenic changes of the developing intestine. Transcription factors, Pitx2 Isl1 and Tbx18, have been shown to play a role in cellular organization changes[3,8] yet less is understood about the effect of biomechanics on genetic and protein level expression. However, Kurpios et al. demonstrated that asymmetric changes in ECM stiffness and/or in combination with

changes in cell: cell adhesion, generate similar morphogenic changes in gut looping as altering transcription factor presentation in silico.[4] The modeling experiments were supported by histological staining showing left-right asymmetries in presence of swelling components, namely hyaluronic acid in the ECM, as well as asymmetries in cell-cell adhesion molecule expression, namely N-cadherin. Shape changing photodegradable hydrogels could serve as additional resources with which to perform in vitro experiments to study the effect of left-right asymmetries on cell-cell adhesion and other morphological or molecular changes. In this regard, the photodegradable scaffold acts as the extracellular matrix, mimicking asymmetries in compaction or stretching depending on whether cells are on the less or more swollen sides respectively. The ability to pattern both conditions in one sample allows for the experimental and control conditions to be

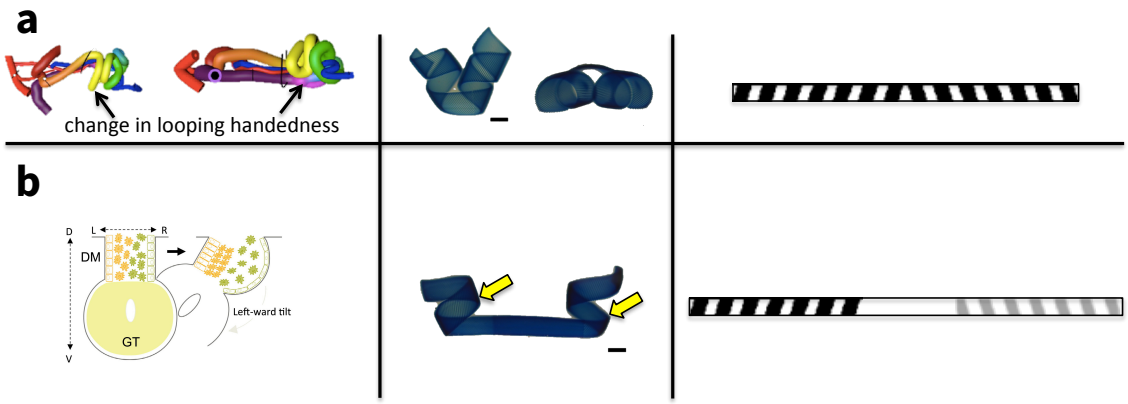

Figure 4.14 Mixed helical folding for generating biomimetic shapes. (a) The helical looping of the small intestine transitions between counterclockwise and clockwise looping directions (left image was modified and reproduced from Ref. 9—article distributed under the terms of Creative Commons by 4.0 https://creativecommons.org/licenses/by/4.0/). Hydrogels were folded in to helices that similarly transition from clockwise to counterclockwise looping (middle) using a photomask with binary stripes at +/- 60° relative to the longitudinal axis (right, stripes are not drawn to scale for visualization purposes). (b) Gut tube (GT) looping direction is encoded by left-right (L, R respectively) extracellular matrix and cell-cell adhesion asymmetries in the attached dorsal mesentery (DM) during development (left image was reproduced with permission from Ref. 8. Left and right sided looping direction was patterned within the same gel. Yellow arrows indicate where inside out turning initiates (middle). The looping directions were encoded by patterning the left half of the gel with oblique angled binary stripes from the top and from the bottom on the right half (right, the black and white stripes indicate top side exposure, while the gray and white indicate bottom side exposure). The scale bars in the middle images represent 1 mm for the respective middle images.

patterned in a single sample, reducing the issue of sample-to-sample variability between hydrogels.

III. Non-zero Gaussian Curvature (Non-developable surfaces):

A folded 3D sheet can be characterized by its principal curvatures (or axes of curvature), κ_1 and κ_2, at each point. The size and direction of the principal curvatures define the local mean and Gaussian curvatures, $H = 1/2(\kappa_1 + \kappa_2)$ and $K = \kappa_1\kappa_2$ respectively. The hollow tubular structures described in the previous section all had approximately zero Gaussian curvature since one of the principal curvatures was approximately zero. In this section, we describe non-developable shapes with negative Gaussian curvatures such that the direction of the two principal curvatures is opposite.

Negative Gaussian curvature is commonly found in nature and can be frequently observed in plants—such as seed pods[77] and flower petals[89]— as well as lipid bilayers,[119] and tissues with complex, mixed curvatures such as bone.[120] Upon identifying negative Gaussian curvatures in nature, we naturally next ask ourselves how they are formed and if we can re-create them using similar physical principles. Gartner et al. described generation of negative *K* by patterning sheets of extracellular matrix mimics with fibroblasts. The fibroblasts exerted traction forces on the sheets resulting in local compaction. Because the sheets were free floating, the compaction led to curving of the sheets. By patterning anisotropic regions of fibroblasts on two opposing sides of the sheet, opposing curvature directions were generated in free floating sheets.[32] In this

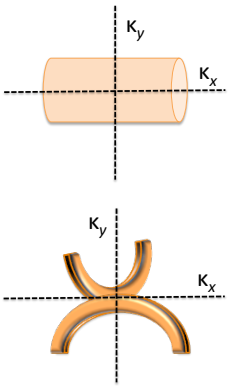

Figure 4.15 Mean and Gaussian curvatures. Tube with zero Gaussian curvature and non-zero mean curvature (top) Saddle splay with negative Gaussian curvature and zero mean curvature (bottom).

example, the negative *K* resulted from externally induced compression forces as opposed to swelling differences, which are more commonly seen in folding and unfolding events in plants. A corresponding example modeled and elegantly implemented by the Lewis group[89] demonstrated exquisite control over curvatures. They did so by patterning bilayers of fibrils in hydrogel matrices. When the fibrils were patterned at opposite oblique angles, the bilayers swelled in opposite directions, resulting in negative *K*—demonstrated in saddle splay shapes or twisted helices for example. Using these systems as an inspiration, we sought to demonstrate similar control over negative *K* in our photodegradable hydrogel films.

As a proof of concept, we first demonstrated shape-change of flat 4 mm diameter hydrogel sheets into folded saddle-splay shapes. Unlike the rectangular sheets with unequal edge dimensions that we previously described, circular discs have no predictable folding axis due to their inherent isotropy. Therefore, the folding axis is random in the absence of anisotropic patterning. We demonstrated control over folding direction by photopatterning hydrogel discs using a single opaque mask stripe down the center of the gel. The resulting folding axis is parallel to the stripe. The masked region down the center has a higher crosslink density than the surrounding gel on the exposed side. The stripe thus acts as a stiff hinge, or elbow, forcing the surrounding coplanar regions of the gel to extend away from it. As the degraded regions swell more compared to the stiffer center stripe, the exposed sides on either end of the stripe bend out of plane from the hinge. We used this control over folding direction, to form saddle splay shapes by exposing flat hydrogel discs to 365 nm light through a 0.5 mm wide photomask stripe down the center on one side (top) and expose the gel from the opposite side using the same light dose

through a photomask down the middle oriented perpendicular to the top side (Figure 4.16). The resulting equilibrated gels had negative Gaussian curvature and approximately zero mean curvature. We exposed films at low and high light doses (4.5 or 18 J/cm^2 on each side) and found no change in mean or Gaussian curvature as a function of light dose. Furthermore, there was no change in curvature one day after folding, suggesting that the saddle splay shapes contain residual stress that prevents them from relaxing. These hydrogels are distinct from the tubular shapes previously described in that they are degraded from the top and bottom. The tubular shapes have a stretching and bending region from the exposed and opposite sides respectively. However, in the case of the saddle splay shapes (demonstrated in Figure 4.17b), both sides are degraded. The swelling for the top and bottom volumes of the gel is relatively similar compared to the one sided exposures. Therefore, both the top and the bottom serve as "stretching" sides with an in-plane central stiffer hinge region that encodes the bending direction.

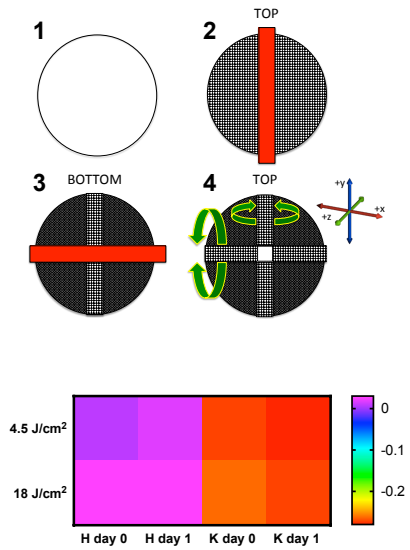

Figure 4.16 Generation of saddle splay shapes from thin flat sheets. (Top) We start with a homogenous hydrogel sheet (1) that is exposed to UV light from the top with an opaque mask down the center (2). The sheet is then exposed from the bottom with a mask placed down the middle, perpendicular to the first mask (3). The resulting degraded gel folds along the +xz and –yz axes (4). The dense grids represent twice-exposed regions, the less dense grids represent once exposed regions and the white regions represent non-degraded regions. (Bottom) Hydrogels were exposed at 4.5 or 18 J/cm^2 on each side and the mean and Gaussian curvatures (H and K respectively) were calculated from front and side view images (values reported are averaged from 4 samples per condition, the same samples were measured at day 0 and day 1). The units for H and K are mm^{-1} and mm^{-2} respectively.

Rather than degrading most of the gel—favoring stretching, and preserving stiffer hinge regions—we also demonstrate that we can generate soft hinges in "stiff" sheets.

The hydrogel discs are exposed to UV light using an opaque photomask with a clear stripe down the center, thus generating a flexible hinge surrounded by non-degraded polymer with lower swelling. We again photodegraded the top and bottom surfaces with the masks oriented perpendicular to one another. Because the majority of the surface area is stiff compared to the hinges, the disc is constrained from large length-scale stretching and folds sharply at one of the hinges, resulting in a generalized V-shape. Proximal to the more swollen, photodegraded hinges, there is localized out-of-plane bulging, resulting in small-scale opposing curvatures (Figure 4.17d). Therefore, we demonstrate that in initially flat hydrogel discs, soft hinges could be encoded to produce localized bulging (or protrusions) in a disc with generalized curvature. These distinct patterning tools give us flexibility over on-demand shape prescription over a range of length scales.

We turn to heart development to illustrate a biologically relevant example of carefully timed evolution of curvatures over a range of length scales. Drawing analogy to our originally flat sheets, the cells that are fated to develop into heart tissue are derived from a thin layer of cells within the mesoderm of the gastrulation embryo.[10,121] The cell layer extends laterally and cranially forming what is termed the cardiac crescent—the name deriving from its crescent shape (Figure 4.17c). The transformation from the cardiac crescent to the formation of the four-chambered heart results from an interplay between both genetic and environmental factors.[122] Biomechanical factors such as the stress and strain that cells undergo during tissue growth (i.e., due to hyperplasia, hypertrophy, and extracellular matrix expansion) and the effect of the extracellular matrix stiffness on cell differentiation and tissue geometries play a major role in this transformation. The shape transformation, or morphogenesis, occurs overall size scales

spanning several orders of magnitude because changes occur locally (i.e. at the cellular or subcellular level) and globally (e.g. looping and septation).[122] Modeling changes in curvature during heart development thus requires the ability to modulate curvatures over several length scales. For example, the interventricular groove between the right and left ventricle generates a saddle splay surface with a generalized curvature over the 100's of micron to mm length scale (Figure 4.17a),[10] reminiscent of the saddle splay surfaces with stiff hinges (Figure 4.17b). Alternatively, an instance of localized saddle splay shape occurs during early heart development when following formation of the cardiac crescent, the region fated to become the atrioventricular canal bulges away from the crescent shaped myocardium, cranial to the developing gut (Figure 4.17c).[10] Several groups have studied the relationship between cardiac morphogenesis and gene and molecular expression or cell differentiation.[121,123-126] Furthermore, defects in timing of shape patterning may lead to disease or even fatality.[127] There remains much to be understood about human heart development due to the difficulties of studying developmental biology in human embryos. Therefore, there is thus far a paucity of knowledge regarding the effect of shape transformations on gene and protein expression and vice versa. The photodegradable cell culture scaffold allows, for the first time, the ability to apply on demand shape transformation—including negative Gaussian curvatures over a range of size scales that are relevant within the context of human heart development. This system presents the opportunity to study the effect of carefully timed shape-change events on human fetal cell differentiation and gene expression in vitro. These are some examples of the kinds of developmental biology questions that we hope can be interrogated using photodegradable hydrogels for on-demand shape transformation.

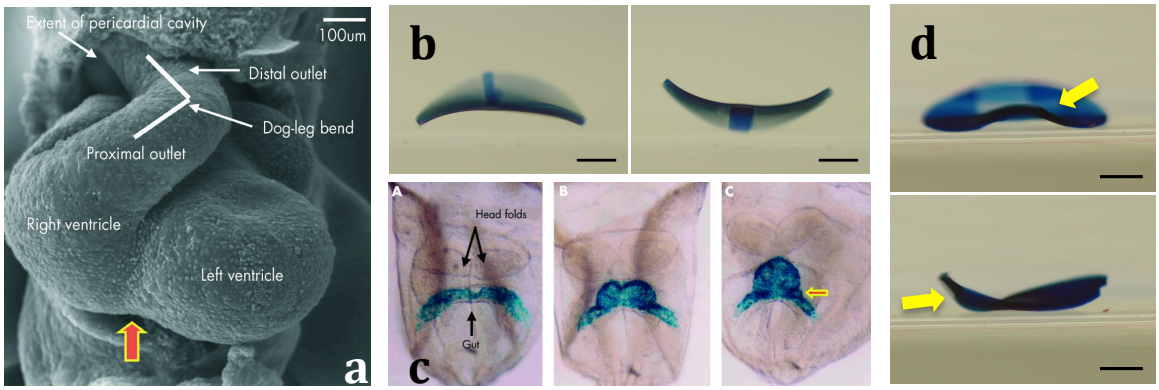

Figure 4.17 Saddle splay curvatures during heart development and biomimetic hydrogel films. (a) The opposing curvature directions in the interventricular groove of the developing mouse heart indicated by the red arrow divides the left and right ventricles generating large scale curvatures (Reproduced with permission from Ref. 10.) (b) Saddle splay shapes formed by patterning stiff hinges in soft surrounding hydrogel matrix similarly result in generalized large scale curvatures. Images are taken from front and side view of the same gel. (c) Mouse embryo progressing from 7.5 to 8 days after fertilization (panels A-C). The myocardium was labeled blue with a reporter transgene. The yellow arrow in panel C points out the bulging region destined for the atrioventricular canal where localized negative Gaussian curvature is generated. (Reproduced with permission from Ref. 10.) (d) Shapes with bulging morphologies formed by patterning soft hinges on opposite surfaces of hydrogel discs. The yellow arrows highlight the bulge formation where the hinges meet the stiffer surrounding matrix reminiscent of the curvatures in panel c. The scale bars in (b) and (d) are 1 mm.

IV. Rippled sheets with mixed curvatures:

We further explored combined top and bottom UV-light exposures to generate non-developable shapes beyond saddle splay shapes. We patterned rectangular sheets using anisotropic patterns on one surface and isotropic patterns on the opposing surface to generate ribbed or wavy sheets (Figure 4.18a,c). These ribbed sheets mimic tissue surfaces such as that of the dorsal mesentery[9] (Figure 4.18b), or the folded interface between cerebral white matter and the cortex.[128-130] We show that anisotropic stripe patterning, at varying angles, on one side only, recovers tubular folding, with striped ridges on the outer surface of the tube (Figure 4.18d). We previously showed that patterned stripes parallel to the longitudinal axis generated folding along the long axis of rectangular sheets. Instead, rectangular sheets with stripes patterned at anisotropic angular orientations on one side combined with parallel stripes on the opposite side generated ribbed surfaces with varying topographical features.

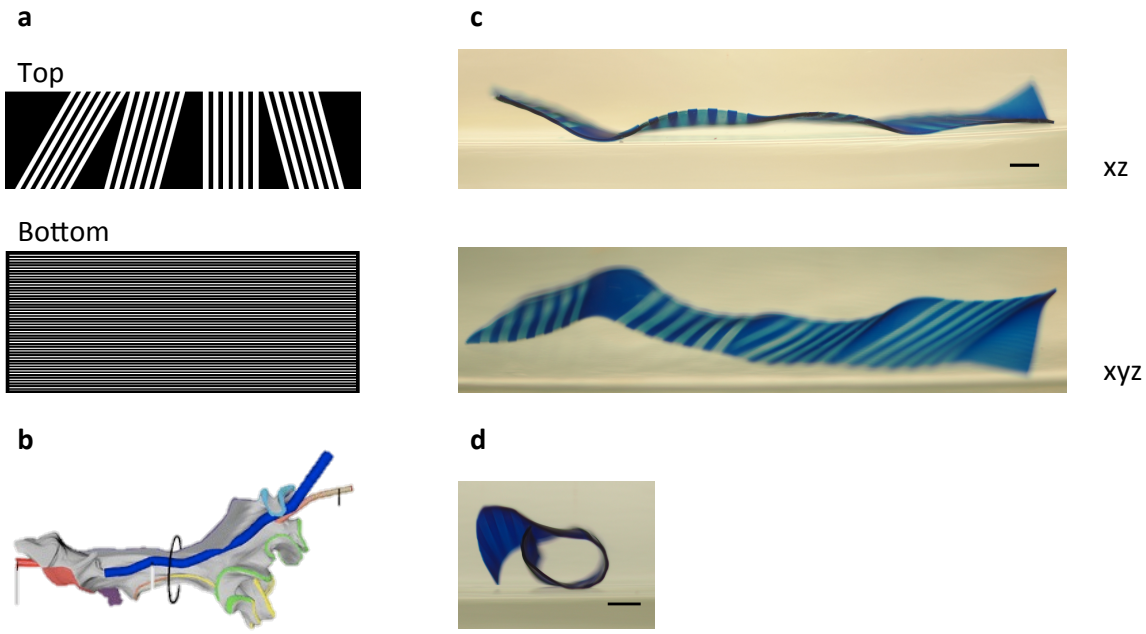

Figure 4.18 Flat sheets folded in to ribbed or wavy structures with arbitrary non-periodic topographical curvatures. The masks used to pattern sheets are demonstrated in (a) and the resulting folding is demonstrated in (c). This type of folding is reminiscent of the folding of the dorsal mesentery (b, image modified and reproduced from Ref. 9—article distributed under the terms of Creative Commons by 4.0 https://creativecommons.org/licenses/by/4.0/). Alternatively, sheets patterned from the top using the mask with stripes at alternating angles only, folds in to tube with ribbed stripes along the outer surface of the tube (d). Scale bar in c and d is 2 mm.

V. Combined micro-scale topographical patterning and macro-scale bending

Tissue morphogenesis arises due to mismatches in strain between neighboring tissues—often a cell layer and the adjacent extracellular matrix. These mismatched stresses occur over a range of size scales generating both global shape transformations,[131] such as the looping morphogenesis of the gut[3,5] and the heart, [122,132] or more locally on the cell (or small groups of cell) size scale.[32,133,134] In recent years, scientists have demonstrated micro and nano-scale control over surface topographies[135-137] and substrate stiffnesses[59,138] for guiding cell fate. Topographical patterning has been shown to improve in vitro muscle differentiation and beating synchrony in cardiomyocytes[139-141] and skeletal muscle.[142,143] While differences in stiffness have been measured for different muscle tissues[144] and substrate stiffness has been shown to affect cardiomyocyte maturation[145] and action potential propagation.[146] Photodegradable

hydrogels based on the *o*-NB PEG macromer were previously used to demonstrate patterning of positive (swollen) and negative (eroded) features on partially and fully degradable hydrogels respectively.[147] Xue et al. later demonstrated the ability to pattern positive and negative features in photodegradable hydrogels with control over the surface modulus, as characterized by AFM.[11]

Inspired by these findings, we sought to generate surface patterned features on photodegradable hydrogel films. We used striped photomasks with 50-100 μm widths to match sizes that have been shown to be relevant for skeletal muscle patterning.[148] However, the feature size can easily be tuned to match the particular application. Of note, Wong et al. demonstrated the use of single photon light excitation to pattern features down to 10 μm in the x-y direction.[147] Theoretically, the feature size is limited by the diffraction limit of light,[149] so that for 365 nm light, we are limited to feature sizes of about 200 nm. Using the 50-100 μm feature masks, we demonstrate that pattern fidelity is maintained as confirmed by transmission and fluorescence microscopy (Figure 4.19). Use of low light dose—controlled by reducing the exposure time and the irradiance—limits the degradation to the surface of the gel. The degradation depth (calculated based on a modified version of the Beer-Lambert law that accounts for diffusion of degraded species)[100] is limited to less than 30 μm from the surface of photodegradable hydrogel films at 20 mW/cm^2, 60 s exposure (hydrogel composition defined in Experimental section). However, following degradation, those regions have reduced crosslink density relative to the non-exposed regions and should thus swell more. This height change due to swelling depends on the starting crosslink density and *o*-NB concentration but is expected to be on the sub-micron size scale based on similar

hydrogels reported by Xue et al.[11] We can use fluorescent dyes, such as trypan blue[150] or rhodamine B[151] (excitation for both at > 480 nm, which is well beyond the absorbance region of the *o*-NB), to resolve degraded and non-degraded regions due to the preferential partitioning of the fluorescent dyes to the non-degraded regions. Taking advantage of the dye partitioning, we empirically observed depth patterning of approximately 25 μm in cross-sections of surface degraded gels imaged using confocal microscopy (Figure 4.19). This is in close agreement with our modeling predictions for depth of degradation through the hydrogel (27.6 μm FWHM, corresponding to 73% intact network strands). These feature sizes, from 10^{-7} to 10^{-5} m, are reminiscent of microscale topographies generated during morphogenesis.

We next exposed surface patterned hydrogels from the opposite side using higher light doses (30 mW/cm^2, 600 s) to generate depth patterns capable of generating macro-scale folding of the thin films. We demonstrate that we can use flood irradiation to fold films in to tubes. The folding direction can be controlled such that the surface stripes align radially (Figure 4.20a, b) or laterally (Figure 4.20c, g) along the tube lumen by cutting high aspect ratio rectangles with the stripes aligned perpendicular or parallel to the long axis respectively. This methodology; however, limits folding to high aspect ratio sheets in order to predictably obtain short axis folding. Therefore, we also demonstrate that we can use striped photomasks to generate depth patterns in rectangles of arbitrary aspect ratios resulting in long axis folding with the surface stripes lining the

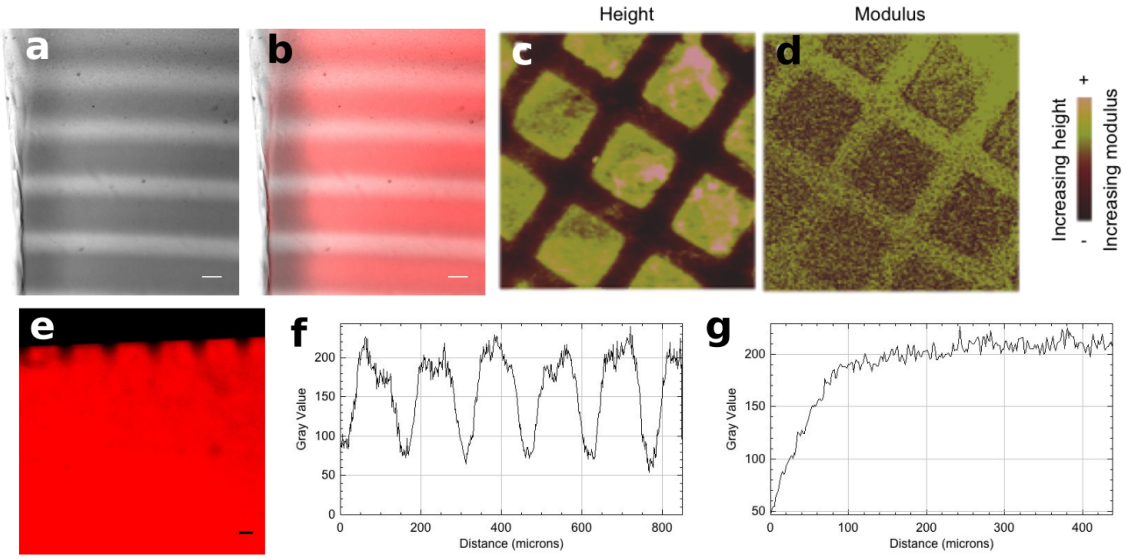

Figure 4.19 Topographical features patterned in photodegradable hydrogel films through photomasks with 100 μm opaque and 50 μm transparent stripes using short exposure times (365 nm, 20 mW/cm^2, 60 s). Phase contrast image of the patterned hdyrogel demonstrates x-y pattern fidelity with the degraded regions appearing brighter compared to non-degraded regions (a). Rhodamine B dye infused in the gels following photodegradation partitions into the non-degraded regions, to further demonstrate contrast between degraded and non-degraded regions (b). AFM images of photodegradable hydrogels exposed to 365 nm light through square grid photomasks. The square regions were exposed and the striped grid regions were masked. The exposed regions are swollen and raised relative to the non-exposed regions (c) and have a lower modulus (d). Images in (c) and (d) were reproduced and modified with permission from Ref. 11. Cross-sections of the surface patterned hydrogels imaged by confocal microscopy demonstrate topographical patterns where the dye preferentially partitions in to the non-degraded bulk of the hydrogel (e). Intensity profile along the surface features of the cross-section of the gel in (e) demonstrates pattern fidelity with the non-degraded regions measuring approximately 100 μm and the degraded dark regions, measuring approximately 50 μm (f). Intensity profile along the depth of the gel, through the degraded sections, demonstrate the degradation depth of 25 μm FWHM (g).

lumen of the tube (Figure 4.20d, e, f). In this case, the tube also has stripes lining the outer wall of the tube. Importantly, the fidelity of the distinct patterns is maintained at the respective surface as demonstrated in Figure 4.20 where in panel e, we demonstrate the x-y cross-section at the top surface of the gel and in panel d, we demonstrate an x-y cross-section at the bottom surface. The different patterns are clearly discernible. Furthermore in Figure 4.20c and g, we demonstrate that in the folded tubes with stripes patterned only on the top surface (along the inner lumen once the gel is folded), stripes are only discernible along one z-plane (panel g) and not on the bottom plane (panel c). Finally, in panel Figure 4.20a we demonstrate a radial cross-section view of a folded gel. The change in contrast along the outer surface of the folded gel demonstrates further

proof of the dye partitioning in to the non-degraded regions more so than the degraded regions. A plot of the intensity across the cross-section was used to calculate the depth of the low-contrast region. We measured a depth of 86 μm, which is in close agreement to the model prediction value of 83 μm.

We envision that this platform can be used to pattern cells seeded on surface patterned hydrogels. Unlike other shape-change systems, the cells can be cultured for several hours to days on the surface patterned gels—allowing time for alignment or differentiation. At an arbitrary time point, the opposite side light exposure can be used to induce tube formation (or other shape-change events of choice with the use of lateral patterning). This expands the toolbox of available substrates for in vitro shape-change applications, allowing for on-demand interrogation of shape transformation events in the presence of cells cultured on pre-patterned substrates.

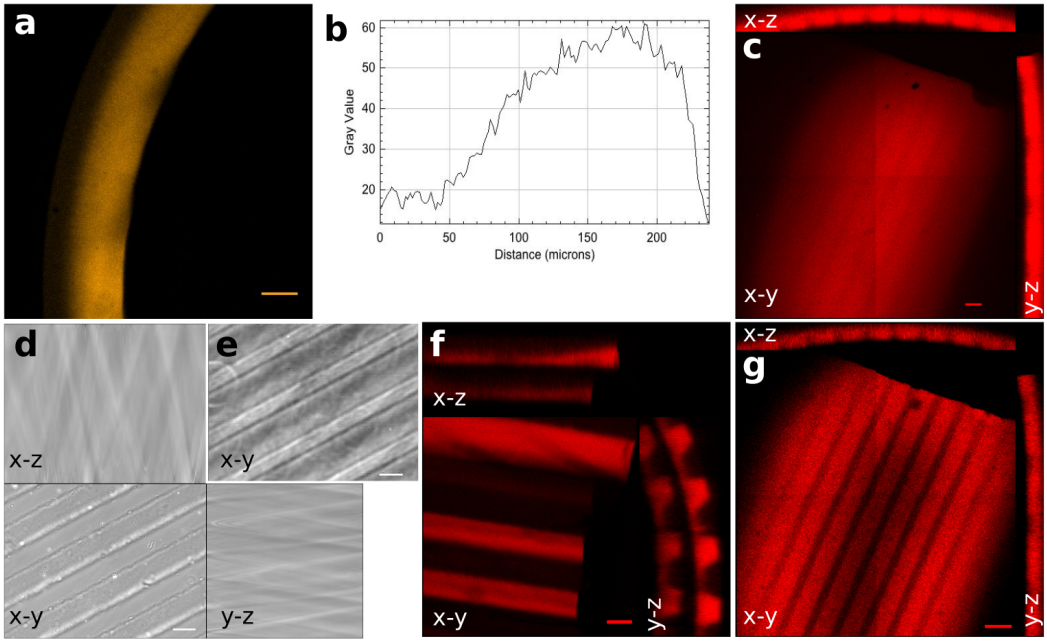

Figure 4.20 Top and bottom patterned hydrogels for topographical surface patterning and macro scale folding. The hydrogels were surface patterned using a striped photomask and low light dose (1.2 J/cm^2) at 365 nm. They were next degraded from the opposite side at high light dose (30 J/cm^2) at 365 nm. Rectangles were cut with the stripes aligned perpendicular to the long axis (a) or parallel to the long axis (c, g). The sheets with stripes aligned perpendicular to the long axis resulted in folded spirals with radially aligned stripes along the inner lumen wall. (a) is a confocal image of a radial view of the folded spiral. The depth of degradation for the high light dose exposure can be visualized in (a) with the darker region along the outer wall of the folded spiral. (b) is a plot of the intensity profile along the cross-section of folded gel in (a). Rectangles with stripes aligned parallel to the long axis folded with stripes aligned longitudinally along the inner lumen wall (g). The stripes are best visualized along the inner lumen wall plane since the stripe patterning was shallow as can be seen in the confocal image x-y view of panel (g) and the x-z view of either panel (c) or (g). The stripes are not visualized on the outter lumen wall as can be seen in x-y view of panel (c). Surface patterned rectangular sheets were also patterned with stripes on the opposite side to favor long axis folding regardless of the rectangular sheet aspect ratio orientation relative to the surface stripes. An example is demonstrated of a phase contrast image of surface stripes patterned using low light dose in (e) at the top surface of the gel and high light dose on the opposite side (bottom of the gel) demonstrated in (d). The pattern fidelity is maintained at either surface after the dual exposures. These samples folded in to tubes spiraling around themselves twice. The stripes on the outter wall of the tube are demonstrated in (f). All the scale bars are 100 μm.

VI. Summary

In this Chapter, we demonstrate the use of flat hydrogel sheet geometries and light patterning to generate different curvatures of interest for tissue engineering and morphogenesis. We demonstrate shapes with non-zero mean curvature and zero Gaussian curvatures (tubular shapes) for mimicking hollow tubes such as blood vessels and the intestine. The curvatures we generate are on the order of 0.3 to 1 mm^{-1}. These curvatures are within the range of size scales reported by Soffers et al. for developing human small

intestine.[9] We also demonstrate saddle splay shapes with negative Gaussian curvature and draw comparisons to heart development. Finally, sheets with mixed curvatures are demonstrated by combining top and bottom surface patterning. These shapes have characteristic micron scale topographical features as well as macro scale folding in to rippled sheets or tubes. The size of micron scale features in this system can be patterned to dimensions relevant for human cell contact guidance—nanometer to micron scale.[135-137]

VII. Experimental

Photodegradable hydrogel film polymerization

Partially degradable hydrogels were prepared at 21.5 wt%. PEG 4000 diacrylate (77 mg) was dissolved in 395.5 μl PBS. Next the B *o*-NB PEG 3350 macromer was dissolved in PBS (173 mg in 395.5 μl PBS). TEMED and APS stock solution were prepared at 0.5 and 1.0 M concentrations in PBS respectively. The pre-gel solution was prepared by mixing 60.8 μl PEG solution with 73.2 μl *o*-NB solution, 8 μl TEMED solution and 8 μl APS solution with vortexing in between additions. The solution was mixed well, pipet between glass slides with 100 μm spacers (unless indicated otherwise) and polymerized for 15 minutes. Following polymerization, the hydrogel films were equilibrated in PBS overnight.

Photomasks

Photomasks were prepared using DraftSight 2018 and printed by CAD/Art Services. Parallel bar striped masks were prepared with 0.1 or 0.5 mm stripes parallel to

the long axis. The stripes alternated between clear and opaque. Angled stripes were prepared with 0.5, 0.1 or 0.05 mm width stripes at 60° relative to the long axis.

Image analysis

Following UV exposure, folded samples were imaged in PBS or DI water (as indicated in the main text) and imaged with a macro lens (Micro-Nikkor 55 mm f/2.8) attached to a digital camera (Olympus E-PL6). Black silicon nitride balls of known diameter (McMaster Carr) were used as size references and imaged together with each sample. From the images, the maximum inner cross-sectional width and lengths were measured using GIMP 2.8 software. The saddle splay curvatures were measured by fitting an ellipse to the curved surface using FIJI.[105] FIJI was also used to evaluate the intensity profile along image cross-sections. From the intensity profile, the full width half maximum was measured to determine degradation depth.

Effect of L:W ratio on bending axis

Photodegradable hydrogel films were photodegraded in a glass petri dish with a No. 1 25 mm × 25 mm glass coverslip on top and PBS surrounding the gel under the coverslip area. A collimated 365 nm light beam was used to expose the gels from one side (through the coverslip). The gels were exposed for 300 s at 40 mW/cm^2 (12 J/cm^2) and then rectangles were cut at 10:1, 10:2.5, 10:5, and 10:10 mm:mm (L:W) ratios. The samples were then transferred to individual wells in a 24-well plate and imaged the following day.

L-shape films were all exposed for 300 s at 20 mW/cm^2 with a No. 1 25×25 mm glass coverslip on top. L-shapes were cut at defined aspect ratios and equilibrated in water to allow the gels to spontaneously lift from the glass substrate and shape-change.

Effect of light dose on bending axis of rectangular sheets

Photodegradable hydrogel films were photodegraded in a glass petri dish with a No. 1 25 mm × 25 mm glass coverslip on top and PBS surrounding the gel under the coverslip area. A collimated 365 nm light beam was used to expose the gels from one side. The gels were exposed for 300 s at 10, 20, or 40 mW/cm^2 (3, 6, or 12 J/cm^2). Following exposure samples were cut at 10:5 mm (L:W) using a blade. The samples were then equilibrated in PBS and allowed to lift and free float. They were then transferred to individual wells in well plates and imaged the following day in PBS and DI water using a macro lens. Ten samples were analyzed per condition.

Effect of patterning stripes parallel to rectangular sheet long axis on bending axis

Photodegradable hydrogel films were photodegraded in a glass petri dish with either 0.5 or 0.1 mm stripe width parallel bar photomask placed directly on the hydrogel. A collimated 365 nm light beam was used to expose the gels from one side. The gels were exposed for 300 s at 20 mW/cm^2 (6 J/cm^2). Following exposure samples were cut at 10:5 mm (L: W) using a blade. The samples were then swollen in PBS and allowed to lift and free float. They were then transferred to individual wells in well plates and imaged the following day in PBS and DI water using a macro lens. At least 3 samples were analyzed per condition.

Effect of patterning stripes at oblique angle to long axis of rectangular sheet on helix looping shape-change

Modulation of rectangle aspect ratio

Partially degradable hydrogels were prepared at 21.5 wt%. PEG 4k diacrylate (77 mg) was dissolved in 395.5 μl PBS. Next the B *o*-NB PEG macromer (PEG 3350 spacer) was dissolved in PBS (173 mg in 395.5 μl PBS). TEMED and APS stock solution were prepared at 0.5 and 2.8 M concentrations in PBS respectively. The pre-gel solution was prepared by mixing 60.8 μl PEG solution with 73.2 μl *o*-NB solution, 8 μl TEMED solution, and 8 μl APS solution with vortexing in between additions for a final APS/TEMED concentration of 0.149 and 0.027 M respectively.

Samples were exposed in a glass petri dish using photomasks with 0.5 mm stripes oriented at 60° relative to the long axis placed directly on the hydrogel. A collimated light beam (365 nm) was used to expose the gels from one side. The gels were exposed for 300 s at 30 mW/cm^2 (9 J/cm^2). Following exposure, samples were cut at 10:1, 10:4 or 10:2 (L:W) aspect ratios for 10, 15 or 20 mm lengths using a blade. The samples were then swollen in PBS and allowed to lift and free float. They were then transferred to individual wells in well plates. Next samples were stained with 0.1% Trypan blue and washed with water 3× until no more dye was being visibly released from the gels.

The following day samples were imaged in DI water with a macro lens (Micro-Nikkor 55 mm f/2.8) attached to a digital camera (Olympus E-PL6). Black silicon nitride balls of known diameter (McMaster-Carr) were used as size references and imaged together with each sample. At least 3 samples were analyzed per condition. The number of turns (N) was determined by counting quarter turns from one end of the helix to the

opposite end. The end-to-end distance of the helix (L_f) was determined using GIMP 2.8 software. The pitch (p) was calculated by L_f/N. The width and length (L_0) were measured using a ruler on the physical gel laying flat on a glass dish. A power series was fit to the plots of L_f vs. n_s, where $L_f = w_s n_s^x$ and w_s was fixed at the stripe width of 0.5 mm.

Modulation of patterned stripe direction and width

Photodegradable hydrogel films were exposed in a glass petri dish with photomasks with 0.5, 0.1, or 0.05 mm stripes oriented at +/- 60° relative to the long axis (as indicated in main text) placed directly on the hydrogel. A collimated 365 nm light beam was used to expose the gels from one side for 300 s at 30 mW/cm^2 or 20 mW/cm^2 (9 J/cm^2 or 6 J/cm^2) (as indicated in the main text). Following exposure samples were cut at approximately 15:1.5 mm (L:W) using a blade. The samples were then equilibrated in PBS and allowed to lift and free float. They were later transferred to individual wells in well plates. Next samples were stained with 0.1% Trypan blue and washed with water 3× until no more dye was being visibly released from the gels.

The following day samples were imaged in DI water with a macro lens (Micro-Nikkor 55 mm f/2.8) attached to a digital camera (Olympus E-PL6). At least 3 samples were analyzed per condition. The N, L_f and p were calculated. For all parameters, averages and standard deviations were calculated using Excel (Microsoft®). The values were used to compare indicated conditions using t test. T tests were run using GraphPad Prism Version 7.0. Two conditions were compared individually, without assuming equal standard deviations. Significant p values were further investigated and calculated using two-stage step-up method of Benjamini, Krieger and Yekutieli.

Saddle splay shapes

Photodegradable hydrogel films were prepared as described in the hydrogel preparation section, but using the D *o*-NB macromer instead of the B group and at 150 μm thickness. Discs were punched from a sheet using a 4 mm diameter biopsy punch. The discs were placed on a 75 mm × 25 mm No. 1 coverslip and covered with a No. 1 25 mm × 25 mm coverslip and PBS surrounding the gel.

For the stiff hinge embedded in soft matrix shapes, a 0.5 mm width mask was placed covering the middle of the disc. The samples were then exposed from the top using 365 nm collimated light beam, at either 25 or 95 mW/cm^2, for 180 s. The gel in the coverslip sandwich construct was then flipped over and exposed from the opposite side with a 0.5 mm width mask placed down the center of the disc, oriented perpendicular to the opposite side. The second light exposure was repeated using the same conditions as the first side. Following the dual side light exposure, samples were equilibrated in DI water. Four samples were analyzed per condition. The flexible hinge samples were instead generated using opaque photomasks with a clear 0.5 mm stripe aligned down the center of the disc.

Samples were stained with 0.1% Trypan blue for imaging purposes and washed with water 3× until no more dye was being visibly released from the gels.

Rippled sheets with mixed curvatures

Photodegradable hydrogel films were prepared as described in the hydrogel preparation section, but using the D *o*-NB macromer instead of the B group and at 150 μm thickness. Sheets were placed on a 75 mm × 25 mm No. 1 glass coverslip and covered with a No. 1 25 mm × 25 mm coverslip and PBS surrounding the gel. A

photomask with 0.5 mm wide binary stripes oriented at 60, 75, 90, and -75° angles from the longitudinal axis. The hydrogels were exposed using a 365 nm collimated light beam at 20 mW/cm^2 for 150 s. The gel in the coverslip sandwich construct was then flipped over and exposed from the opposite side through a photomask with 0.1 mm wide binary stripes oriented parallel to the longitudinal axis using the same light exposure conditions. Following photodegradation, rectangular sheets were cut and allowed to equilibrate in DI water. Samples were stained with 0.1% Trypan blue for imaging purposes and washed with water 3× until no more dye was being visibly released from the gels.

Combined surface and depth patterning for multi-scale shape-change

Photodegradable hydrogel films were prepared as described in the hydrogel preparation section, using either the D or the B *o*-NB macromer. Samples for surface patterning only were prepared at 500 μm thickness to facilitate cross-sectional sample preparation. Those samples were exposed through photomasks with 50 μm transparent and 100 μm opaque binary stripes placed directly on the gel using a collimated 365 nm light beam at 20 mW/cm^2, for 60 s. The gels were equilibrated in PBS overnight and then dyed using an aqueous 0.1% Rhodamine-B solution. The surface features were imaged using an inverted microscope the following day (Axiovert Observer Z1, Zeiss). Cross-sections were cut and placed in glass bottom wells for imaging. The cross-sections were embedded in 2% agar in order to impede the diffusion of the dye from the hydrogel while maintaining hydrogel in swollen state. Cross-sections of surface patterned and non-degraded (control samples) were imaged using a laser scanning confocal microscope (Zeiss LSM 780). Tubes with stripes lining the lumen wall were prepared using 150 μm thickness films. The gels were surface patterned as described above. Following

equilibration, the films were exposed from the opposite side using a 365 nm collimated light beam at 30 mW/cm^2 for 600 s. Samples were cut such that the surface stripes were aligned parallel or perpendicular to the long axis of 10:1 (L:W) rectangular sheets for generating tubes with transverse or radially aligned stripes respectively. Alternatively, photomasks with 0.1 mm binary stripes were patterned on the side opposite to the first, low light-dose exposure. The mask was placed on a glass coverslip covering the gel and aligned such that the stripes were parallel to the previously patterned stripes. The twice exposed samples were equilibrated in water overnight and allowed to fold in to tubular shapes. Following equilibration, they were dyed with trypan-blue or rhodamine-B. Folded tubes were then placed in individual glass bottom wells for imaging and encapsulated in 2% agar to prevent samples from moving during imaging. Folded samples were also imaged using confocal microscopy in radial or transverse orientations as indicated in the main text. Confocal imaging was done with EC Plan-Neofluar 10×/0.30 M27 objective mounted on a laser scanning microscope (Zeiss LSM 780) at the UCLA BSCRC Microscopy Core imaging facility.

Chapter 5

SHAPE CHANGING GELS FOR CELL AND TISSUE CULTURE

I. Shape-change in the presence of cells

In the previous sections we demonstrated control over the extent and timing of bending as well as the ability to control curvature direction to generate biomimetic shapes using photodegradable hydrogels. In the last chapter, we also sought to demonstrate the application of our shape-change hydrogels for tissue culture. The objective of this chapter is to demonstrate that the photodegradable shape changing hydrogels can support seeded and encapsulated mammalian cell culture. The shape-change can be actuated at a time point of choice in order to pattern flat 2D cell laden sheets in to shapes with 3D curvatures that are reminiscent of shapes observed in human anatomy.

II. Evaluation of seeded cell ability to maintain morphology and proliferate

We initially sought to demonstrate the compatibility of our shape-change materials and process with cells seeded on sheets. We seeded C2C12 cells on initially flat photodegradable gels prepared using the acetovanillone derivative *o*-NB macromer (referred to as the B group in Chapter 3) first reported by Anseth and co-workers.[36] The flat hydrogels were exposed to 365 nm UV light on the side opposite cell seeding. The gels folded in to tubular shapes with cells occupying the inner surface. Due to the absorption of light by the *o*-NB moieties, the cells on the gel surface opposite the light source were only exposed to a small fraction of the incident UV light (< 1 mW/cm^2 or < 0.6 J/cm^2 for 600 s exposure time and 60 mW/cm^2 intensity). Kasko and co-workers previously demonstrated that 365 nm UV light at a dose of up to 5.25 J/cm^2 did not affect hMSC gene expression.[152] By increasing the light dose, increasingly tubular structures

were produced in the presence of cells (Figure 5.1) The folded gels retained their tubular shape throughout the culture period. Controlling the UV light dose can thus produce different degrees of folding. Much like the acellular samples, 150 μm thickness gels with seeded C2C12s folded into tubes when exposed to 365 nm UV light intensity of 40 mW/cm^2 (24 J/cm^2) or higher. The minimum measured tube diameter with C2C12s was approximately 1 mm (Figure 5.1a), which is in the same order of magnitude as muscle fascicle diameter (assuming 200 muscle fibers of 50 μm diameter per fascicle).[153,154] These results were the first account of UV light actuated shape-change of cell-laden sheets. We demonstrate that the shape-change process and material were compatible with C2C12s.

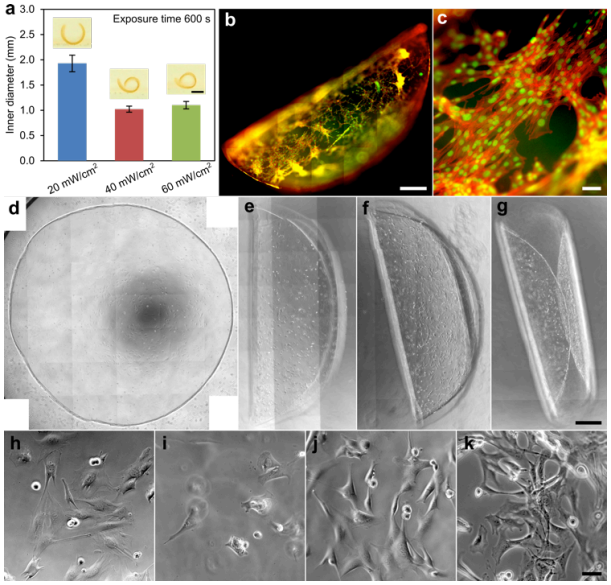

Figure 5.1 Folding of C2C12s seeded on photodegradable hydrogel films. (a) Example images and measured inner diameters of samples exposed to 20, 40 or 60 mW/cm^2 UV light for 600 s (12, 24 or 36 J/cm^2) with C2C12s on the inner surface. Scale bar is 1 mm. Data are shown as mean ± standard deviation (n = 2-5). Fluorescence image of a (b) folded tubular structure and (c) the corresponding close-up image. The cell nuclei are stained green and the actin cytoskeleton red using acridine orange and TRITC-phalloidin respectively. Phase contrast images of a sample (d) 1 day after C2C12 seeding (pre-exposure) and 2, 4 and 6 days after UV exposure (e-g). Corresponding close-up images are shown in (h-k). For both fluorescence and phase images, scale bars are 500 μm for full sample images and 50 μm for close-up images. Image reproduced with permission from Ref. 1.

III. Temporal control of bending

One of the important features of our photodegradable shape-change system is user directed temporal control over sample folding. That is, shape-change can be induced at any point after cell seeding. No other shape-change system reported thus far enables shape-change in preformed hydrogels using cell compatible light stimulus. Using long

wave UV light exposure, folding can be induced in the presence of cells at desired time points. We demonstrate this concept by exposing gels to 365 nm UV light 24 h and 72 h after C2C12 seeding (Figure 5.1). In both cases, the C2C12s seeded on the gels exhibit a fusiform or star-shaped morphology characteristic of undifferentiated C2C12s[155] both before and after UV exposure and folding. The fusiform morphology was further visualized by the staining of the actin cytoskeleton (Figure 5.1b, c). Samples exposed 24 h after seeding were approximately 40-50% confluent at the time of folding (Figure 5.1d, e). At 2 days after folding, the cells were less elongated (Figure 5.1e, i) than prior to exposure but regained their original morphology by 96 h after exposure (Figure 5.1f,j). By day 6, the cells were approximately 80-90% confluent and occupied most of the inner surface area of the folded tubular structures (Figure 5.1g, k). The modulus of the tube interior, which is not exposed to UV light, is expected to be similar to the bulk non-degraded gel. The measured average modulus of the non-degraded hydrogels was 23 kPa. This is in close agreement with the elastic modulus of differentiated C2C12s measured by Truskey and co-workers using atomic force microscopy.[144] In summary, we demonstrate ability for cells to undergo large changes in curvature at arbitrary time points of choice.

IV. Endothelialized tube formation with human aorta endothelial cells

Since endothelial cells naturally form a thin lining along the inner lumen of hollow tubular blood vessels, we applied the same model of folding sheets in to tubes using human aorta endothelial cells to line the lumen. The cells were seeded on photodegradable hydrogel films with RGD-binding peptide attached. When the cells were about 80-90% confluent (Figure 5.2a, b), the gels were exposed from the bottom, opposite the cell seeding side, and the sheets folded in to tubes. Since the gels are not

attached to the well plate, they are not perfectly flat and there are out-of-plane cells during imaging in the normal culture condition medium volume (Figure 5.2a). Figure 5.2b is a minimum intensity z-projection through the area depicted in Figure 5.2a, more accurately demonstrating cell spreading area on the flat hydrogels prior to folding. Following folding, the cells remained attached and spreading along the inner lumen of the folded tubes (Figure 5.2e, f). The out-of-plane cells are even more pronounced following folding due to the steep curvature of the tube. Thus a minimum intensity projection through Figure 5.2e area is demonstrated in Figure 5.2f to again give a better representation of the cell spreading along the inner lumen of the tube. The folded tubes had a cross-sectional width of 1.7 ± 0.1 mm (average ± standard deviation). The lengths ranged from 8-9 mm (Figure 5.2j, k).

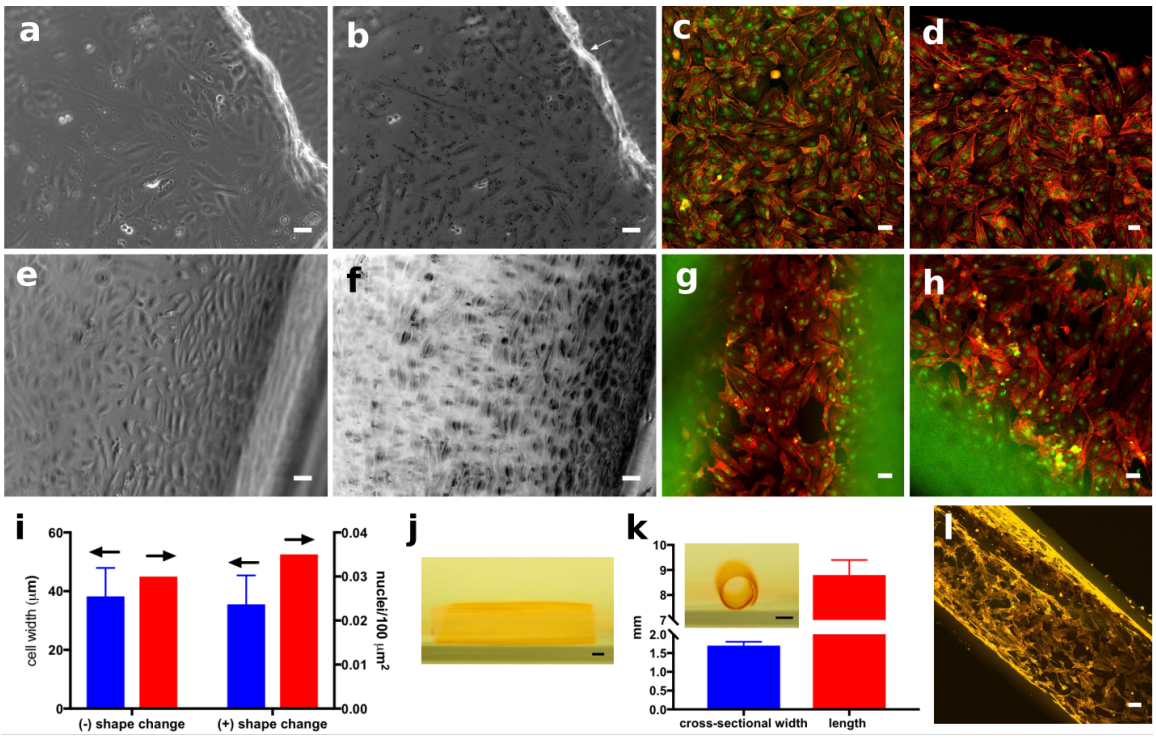

Figure 5.2 Human aorta endothelial cells (hAECs) seeded on shape changing hydrogels morphology and tube dimensions. Cells were imaged one day after seeding. A single z-plane image captures out-of-plane cells since the hydrogels were not perfectly flat on the well plate (a). A z-stack minimum intensity projectiondemonstrates that cells were about 80-90% confluent prior to shape change (b). The hAECs were imaged on shape-changed hydrogels at a single z-plane (e) as well as through a z-stack (minimum intensity z-projection in (f)). Two days after seeding, cells were fixed and stained for actin (red, rhodamine phalloidin) with nuclei counterstained (green, acridine orange) on flat (-) shape change hydrogels (c, d) and tubular (+) shape change hydrogels (g, h). In (i) the cell width (blue, left side axis) was approximately 40 μm for (-) and (+) shape change conditions. The cell density (red, right side axis) was 0.03 and 0.035 nuclei/100 μm^2 for the (-) shape change and (+) shape change conditions respectively. Tube length views (j) and lumen cross-sectional views (k-inset) were used to measure characteristic features of 5 gels (k). In (l) we demonstrate a minimum intensity z-projection of hAECs spreading in a tube (actin false colored yellow). The scale bars in a-h, l are 50 microns. The scale bars in j and k-inset are 1 mm.

HAECs were cultured for one day following folding, at which point they reached confluence in most regions (Figure 5.2g, h). The cells formed a cobblestone monolayer—typical of endovascular surface morphology of large vessels like the aorta—in some regions. However, on both flat hydrogels not exposed to UV light and folded gels exposed to UV light, there were regions of cells with more elongated or fusiform morphologies, reminiscent of endothelial cells exposed to laminar flow (Figure 5.2c, d correspond to the no UV, (-) shape-change, hydrogels and Figure 5.2g, h correspond to the UV exposed, (+) shape-change, condition). There were no substantial differences in

cell width or density (Figure 5.2i). However, actin stress fibers tended to be concentrated at the cell peripheries in the (-) shape-change condition, and more diffuse in the (+) shape-change conditions. Kolluru et al. also observed pronounced patterns of actin concentration at the periphery of endothelial cells. They found this to be the case both when nitric oxide synthase was inhibited with L-NAME and in static cell culture conditions compared to shear flow conditions, albeit to a lesser extent.[156] They went on to demonstrate that there is a relationship between nitric oxide production and cell migration under shear stress conditions. Shear stress stimulates nitric oxide production[157] and also plays a role in endothelium remodeling, such that cells exposed to physiological shear stress velocities underwent a 2-fold increase in migration.[156] Balaguru et al. similarly observed differences in actin distribution for endothelial cells exposed to normal shear stress in laminar flow—intended to simulate normal physiological conditions—compared to static conditions and disturbed flow—intended to simulate pathologic conditions.[158] They demonstrated that cells under static conditions and disturbed flow tended to have more concentrated actin in the cell peripheries compared to cells under normal laminar flow, which had more diffuse actin distribution. These results demonstrate that endothelial cells respond to flow mediated forces via cytoskeletal rearrangements.

Indeed, Chien's 2007 review eloquently describes a series of studies on endothelial cell mechanotransduction response to fluid shear stress as well as cyclic stretch.[159] He reported results from his own lab on the effect of cyclic stress on actin stress fibers in bovine aorta endothelial cells (BAECs), demonstrating that uniaxial stretching resulted in perpendicular fiber orientation while biaxial stretching resulted in more random fiber orientation.[160] Since both stretch[161,162] and flow induced[163,164] stress

have been shown to affect actin fiber orientation in endothelial cells, we sought to characterize cellular alignment in our system as well. A histogram of the Fourier component analysis for several images of nuclei and actin staining revealed the orientation angles for the two conditions. We found that the nuclei in the (-) shape-change condition were more aligned than the (+) shape-change condition—as determined by lower dispersion angles for Gaussian distribution fits of the histograms. However, differences in actin fiber orientation between the two groups were even more pronounced than for nuclei. The (+) shape-change group actin exhibited bimodal distributions with two peaks in the orientation angle histograms, while the (-) shape-change group was mono-modal. Furthermore, the dispersion angle was consistently smaller for the (-) shape-change group, implying more uniform directionality compared to (+) shape-change conditions (Table 5.1). The (+) shape condition is expected to expose cells to more anisotropic mechanical stress compared to the (-) shape-change condition. However, the confluent cell layer may have started to align locally due to interactions with neighboring cells. The folding mediated bending force may disrupt those cell-cell interactions by introducing an external stress. Building upon the theory suggesting that cells with disperse actin have increased migration capacity compared to cells with actin localized at the peripheries, the disruption in cell-cell interactions combined with increased migration capacity is predicted to have led to more gross disperse actin orientations. It remains to be seen if the (+) shape-change cell monolayer would eventually begin to align if left in culture longer following tube formation.

Table 5.1 Orientation analysis of hAECs cultured on flat or self-folded tubular hydrogels

Actin				Nucleus			
Dispersion angle	Modality	Goodness	Amount	Dispersion angle	Modality	Goodness	Amount
29.47	mono	0.90	0.76	23.83	mono	0.66	0.59
25.99	mono	0.72	0.66	23.83	mono	0.71	0.72
30.3	mono	0.82	0.67	30.22	mono	0.43	0.70
41.11	dual	0.70	0.71	36.9	mono	0.30	0.83
48.36	dual	0.58	0.43	15.67	dual	0.05	0.35
114.04	dual	0.50	1.00	20.17	dual	0.23	0.47

We demonstrate that following UV exposure, hAEC-laden hydrogels folded in to tubes with cells lining the entire lumen. A representative image of actin coverage is demonstrated in 3D projection confocal microscopy images in Figure 5.3. Furthermore, orthogonal projections demonstrate the cells growing in a monolayer such that spreading is limited to one z-plane (Figure 5.3d, e). Although the tubes demonstrated here are about 10 times smaller than human aorta diameters, we expect that the same system could be applied to other vascular endothelial cell types common in smaller mm scale vessels.

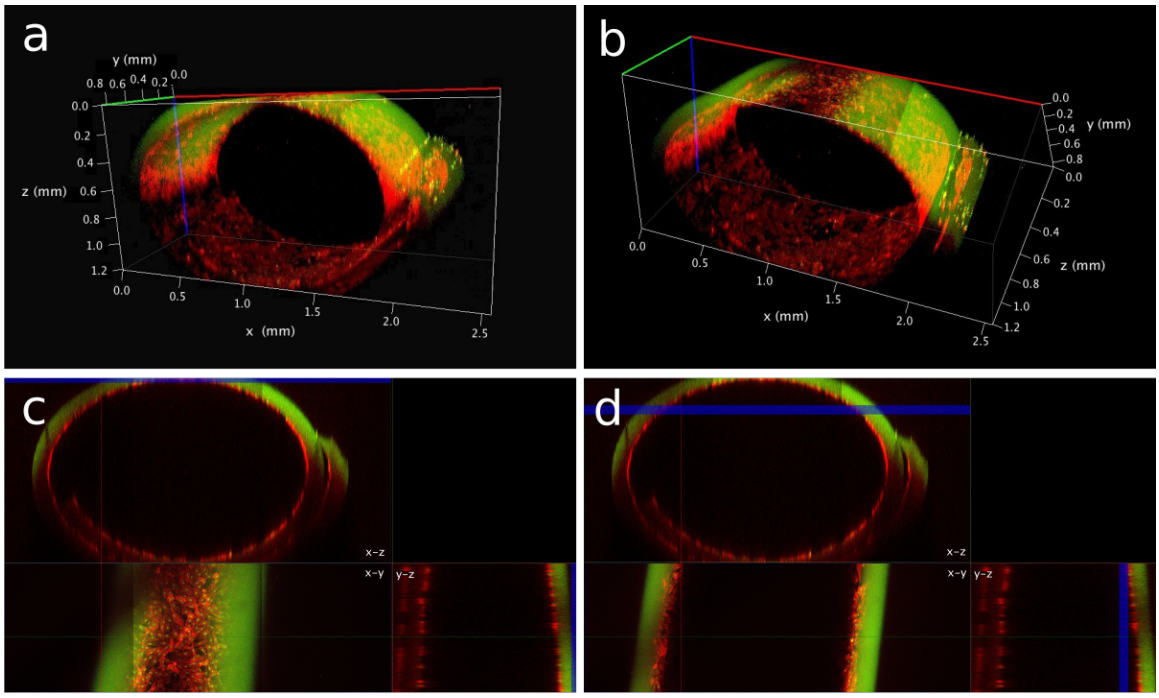

Figure 5.3 Confocal imaging of hAECs lining the inner lumen of self-folded hydrogel tubes. The cells were stained for actin (red, rhodamine-phalloidin) and nuclei were counter-stained (green, acridine orange). Three-dimensional projections at different angles are demonstrated in (a, b). The orthogonal sections in (c) and (d) are at different z-heights demonstrating that the cells form a monolayer on the hydrogel surface, reminiscent of blood vessels in vivo.

V. Shape-change in the presence of encapsulated cells

C2C12s in tubes

Our photodegradable shape changing system also enables cell encapsulation during gel formation due to the use of non-toxic macromers. As a proof of concept, we encapsulated C2C12s in photodegradable gels and used UV light to induce folding (Figure 5.4). The majority of C2C12s remain viable one hour following encapsulation and immediately after UV exposure and subsequent folding for the range of doses used (23-50 J/cm^2) (~60-70%, depending on how viability is assessed). We found cell viability to be compromised following encapsulation due to the polymerization conditions. This is due to the APS/TEMED radical initiators since the macromers do not affect cell viability as discussed in the Experimental section. In another study, Griffin et al. found > 90%

viability using a similar encapsulation protocol for human mesenchymal stem cells,[37] but it is difficult to compare viabilities from one study to another due to differences in polymer composition, and potential differences in sensitivity for different cell types. Mironi-Harpaz et al. compared crosslinking efficiency versus cytotoxicity to bovine aortic smooth muscle cells. The cells were encapsulated in PEG hydrogels using several photoinitators as well as APS/TEMED polymerization. Using 4× lower APS/TEMED concentrations than ours, they measured <20% cell viability compared to 90% for cells encapsulated in PEG hydrogels using the photoinitiator (2-hydroxy-1-[4-(hydroxyethoxy)phenyl]-2-methyl-1-propanone (Irgacure 2959, I2959; Ciba Specialty Chemicals, Basel, Switzerland).[165] The more common method of polymerizing PEGDA hydrogels using long wave UV initiators such as I2959 is not suitable for our application due to the limited absorbance of I2959 beyond 365 nm and the rapid degradation of the B *o*-NB group at 365 nm. However, the added benefit of incorporating spatiotemporal control over polymerization in addition to the already demonstrated spatiotemporal control over degradation encouraged us to seek out cell-friendly photoinitiators with absorbance in the visible region and outside of the wavelengths where the B group *o*-NB has significant absorbance. Thus, having demonstrated light actuated shape-change of cells encapsulated in hydrogels polymerized using APS and TEMED, we next sought to develop a system where we could take advantage of wavelength tuning to use light for both polymerization and photodegradation. We hypothesized that photopolymerization could help improve encapsulation viabilities and offer the added benefit of control over timing and 2D sheet patterning since the polymerization occurs upon photoexposure and masks can be used to pattern 2D shapes.

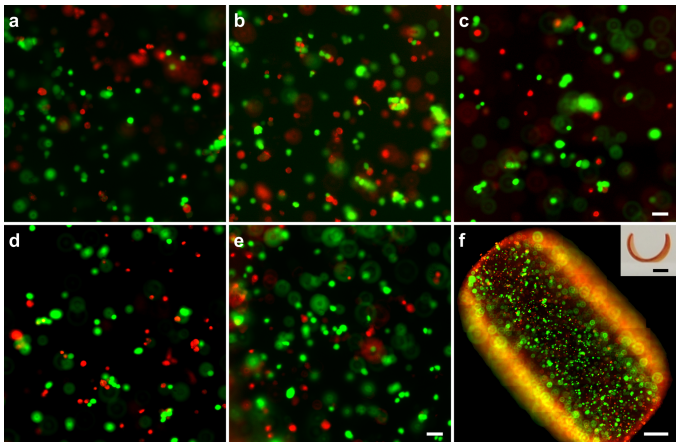

Figure 5.4 Cell encapsulation in photodegradable hydrogels. Cell viability was determined using Live-Dead™ fluorescence imaging (green indicates live and red indicates dead cells, which were stained with calcein AM and ethidium homodimer respectively) in (a) flat, non-degraded gels and folded gels exposed to (b) 84 mW/cm^2, (c) 74 mW/cm^2, (d) 62 mW/cm^2 or (e) 38 mW/cm^2 UV light for 600 s (365 nm, 50, 44, 37 or 23 J/cm^2 respectively). The scale bar in (c) and (e) is 100 μm and corresponds to the images in (a)-(e). In (f) is a tiled projection of a folded gel exposed to 74 mW/cm^2 UV light. The scale bar in (f) is 500 μm. The inset is an image of the folded gel in (f) with C2C12s encapsulated within. The inset scale bar is 1 mm. Image reproduced with permission from Ref. 1.

Visible light photopolymerization for encapsulation of C2C12s in photodegradable hydrogels

Several groups have discussed the use of lithium phenyl-2,4,6-trimethylbenzoylphosphinate (commonly referred to as LAP) as an alternative photoinitiator for cell encapsulation in hydrogels. While I2959 is commonly used due to its moderate water solubility and absorbance at 365 nm, its absorbance into the visible region is too low to make it useful for encapsulations at 400 nm and beyond. Anseth and coworkers demonstrated the use of LAP for photopolymerization of PEG-diacrylate hydrogels at 405 nm. Importantly, they demonstrated that low enough LAP concentrations and polymerization times at 405 nm could be used to achieve >95% survival rates of human neonatal fibroblasts 24 h after encapsulation.[166] Other groups later demonstrated the use of LAP to initiate crosslinking of hydrogels containing nitrobenzyl moieties at 405 nm followed by degradation using UV light. However, these studies were not in the presence of cells.[139,167] Anseth and co-workers more recently used

LAP to stiffen pre-degraded *o*-NB hydrogels in the presence of 2D seeded cells. The hydrogels contained *o*-NB moieties to enable the initial photodegradation, or softening step. The gels were then exposed to a LAP solution and visible light to subsequently stiffen the cell substrate.[168] However, to the best of our knowledge, no group has demonstrated LAP (or another photoinitiator for that matter) for photoencapsulation of mammalian cells in PEG *o*-NB hydrogels.

To this end, we encapsulated C2C12 mouse myoblasts and human fetal muscle (hFM) cells isolated from quadriceps in photodegradable gels using 1% LAP concentration. We found that we needed to use much higher photoinitiator concentrations compared to Anseth and co-workers[166] (1% vs. 0.06%) to achieve polymerization under similar 405 nm light exposure conditions. These differences are likely due to the unusually high chain transfer rate of nitro substituents on aromatic rings in free radical polymerizations.[169] We measured 98 ± 2% (n=4) and 87 ± 6% (n=5) viability for C2C12 and hFM cells (respectively) encapsulated in 21.5 wt% hydrogels at 24 h after encapsulation (Figure 5.5). However, the 21.5 wt% hydrogels were not suitable for photodegradation induced shape-change since they completely degraded following even modest UV light exposures as low as 6 J/cm^2. We thus also prepared 25 wt% hydrogels for C2C12 encapsulation and observed 86 ± 10% (n=5) viability after 24 h (Figure 5.5). Although the viability was compromised with the higher weight percent gels, the viabilities were still suitable to support cell proliferation and spreading for several days. While the cells were not able to degrade the PEG-based hydrogels, many cells settled to the bottom of the hydrogel precursor solution before the polymerization was complete. Those cells at the gel boundary interface were able to spread and to proliferate over

several days. The cells surrounded by polymer on all sides remained rounded. One day after encapsulation, a subset of gels was exposed to 365 nm light from one side to initiate shape-change. Viabilities were determined 5 days after encapsulation for (-) UV (flat) and (+) UV (folded, tubular) gels. We did not observe a significant difference in viability between the (-) UV and (+) UV conditions (e.g. 88 ± 9% (n=3) and 83 ± 8% (n=5) respectively, Figure 5.5). Furthermore, there was little change in viability for the (-) UV gels between 24 h and 5-day time points (86% at 24 h vs. 88% at 5 days).

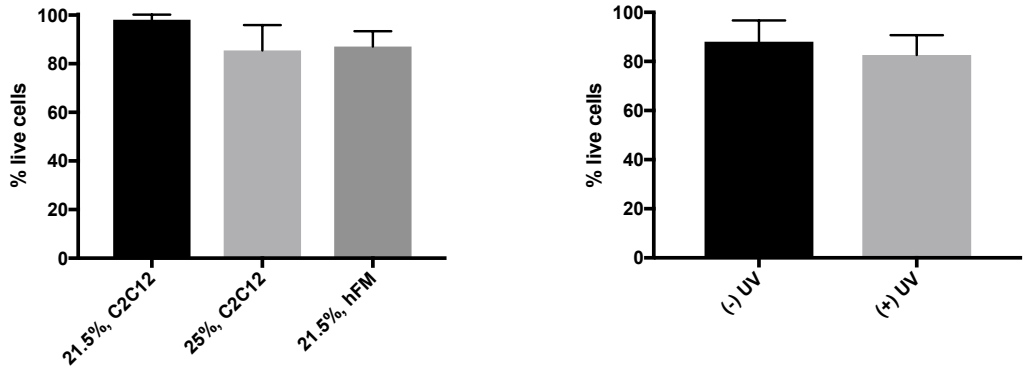

Figure 5.5 Cell encapsulation viabilities in photodegradable hydrogels using LAP initiator at 405 nm. C2C12 and hFM cells were encapsulated in 21.5 or 25 wt% hydrogels. The viabilities were determined after 24 h (left). A subset of 25 wt% gels was exposed to 365 nm light photodegradation ((+) UV) in order to initiate shape change while other gels were not exposed to UV light ((-) UV) 1 day after encapsulation. The viabilities of C2C12s encapsulated in the (-) UV and (+) UV samples was determined 5 days after encapsulation (n=3 and n=5 respectively). There was no appreciable difference in viability between the two conditions (right).

The encapsulation of cells in self-folding films has been previously demonstrated using hydrogel systems but not using photodegradation mediated folding. Gracias and co-workers reported self-folding PEGDA bilayers with encapsulated β-TC-6 insulin secreting cells.[7] The same bilayer system was used as an in vitro model for ductal carcinoma.[31] Ionov and co-workers have demonstrated the encapsulation of neural stem cells in gelatin/PHF-Q bilayers.[96] In both of these studies, folding was induced

immediately after immersion in water and could thus be induced only at the beginning of the cell culture. In contrast, our gel system allows cells encapsulated in flat equilibrated gels to be folded at a user defined time point. Our photodegradable self-folding system is, to the best of our knowledge, the first system that enables shape-change in the presence of both seeded and encapsulated cells at a time point of choice, making it possible to directly compare 2D and 3D cell culture environments. Furthermore, we also demonstrate for the first time radical initiated chain-growth photo-encapsulation combined with photodegradation in a hydrogel system. This approach could become a new tool in stem cell differentiation and developmental biology research, facilitating the in vitro investigation of processes that are sensitive to both physical and temporal stimuli.

C2C12s encapsulated in photodegradable hydrogels for light initiated tube formation

We further demonstrate the application of the photodegradable hydrogel system for tube formation of encapsulated C2C12 cells. Flat hydrogel films were folded in to tubes of approximately 1-2 mm diameter (Figure 5.6f) and 7-10 mm length (Figure 5.6e). As previously mentioned, although the cells are not capable of degrading the PEG-based hydrogel via enzymatic degradation, many cells settled to the bottom of the gel during the polymerization process. Gels were polymerized on glass slides with round coverslips placed on top using collimated 405 nm light transmitted through the coverslip side first. Following polymerization, the gels adhered to the coverslips. The gels on the coverslips were transferred to well plates so that the coverslip faced the bottom of the well plate and the gel side that was originally in contact with the glass slide faced the surrounding medium. Thus, the cells that settled to the bottoms of the gel (glass slide side) during the polymerization ended up at the gel-media interface in the well plates and were free to

spread and proliferate, becoming confluent in some regions (Figure 5.6c). We demonstrate the ability to initiate tube formation at 1 or 6 days after encapsulation (Figure 5.6b and a respectively). C2C12 actin, stained red, was imaged by confocal microscopy to demonstrate cells spreading along the surface of the folded films. An orthogonal projection of a folded tube demonstrates cells spreading along the curved gel surfaces. Acridine orange was used to counterstain the nuclei, however, we also observed significant background staining, due to partitioning of the acridine orange in to the hydrogel itself. This was evident due to the change in color of the gel to a darker orange following acridine orange staining. Therefore, the x-z and y-z projections in Figure 5.6c demonstrate the thickness of the hydrogel (green) with cells spreading along the surfaces of the hydrogel, which spiraled around itself twice. Although we previously demonstrated folding of hydrogel films with both C2C12 cell seeding and encapsulation, the cells remained in a myoblast state. This was evidenced by their fusiform or stellate morphologies in the seeding and rounded morphologies in the encapsulation experiments.[1] Here, we observed some cells starting to fuse and elongate in to multinucleated cells—characteristic of myotube formation[155]—in the absence of differentiation medium (Figure 5.6d and g).

In the future, an MMP degradable peptide could be incorporated in to the PEG-based hydrogels or the PEG be partially substituted with an enzymatically degradable scaffold, such as gelatin, in order to allow for the cells to spread within the 3D matrix as opposed to being limited to the gel surfaces. Furthermore, the cell encapsulation density could be increased or the cells could be cultured longer to allow for enhanced proliferation and myotube differentiation in a 3D folded tubular substrate. Finally,

photomasks could be used to photopolymerize several 2D hydrogel films in parallel using a wide 405 nm beam. This could increase parallel processing times and also opens the possibilities of patterning different 2D sheets for creating different 3D shapes upon UV light exposure.

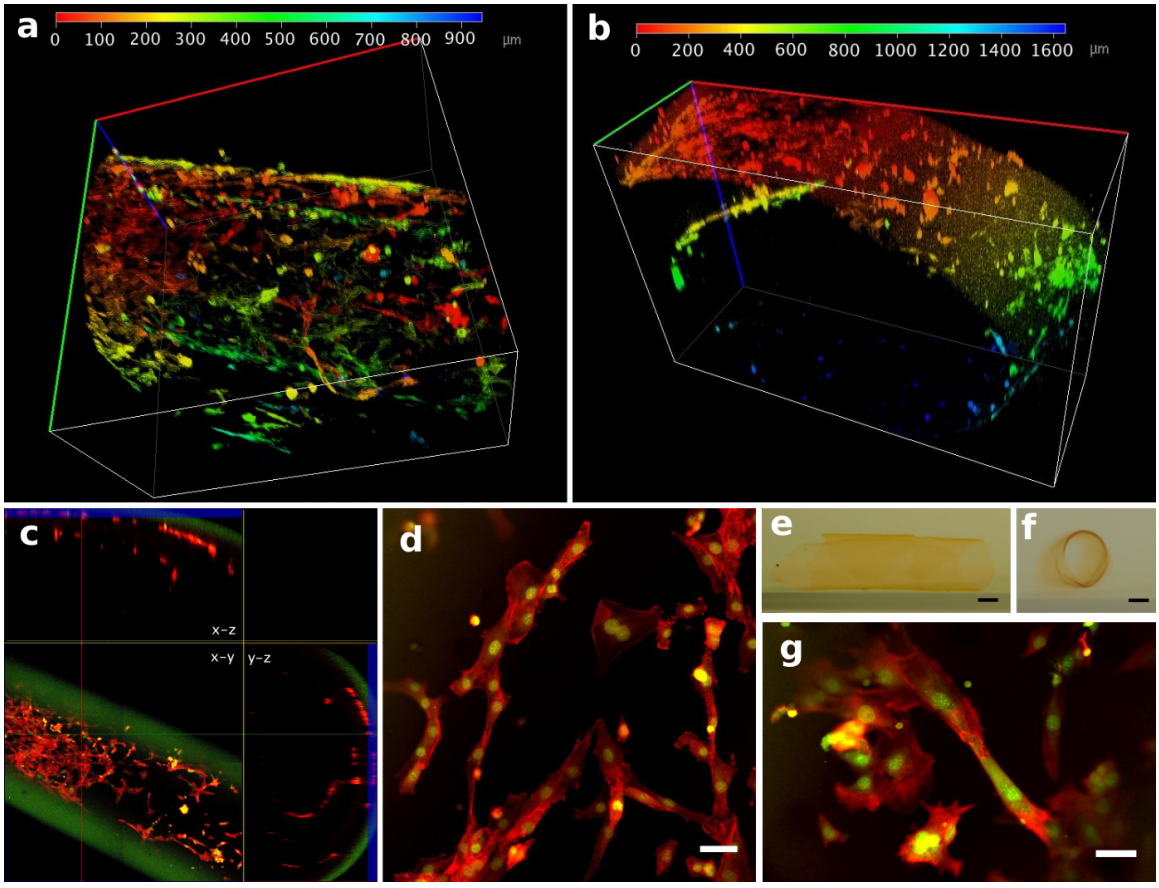

Figure 5.6 Confocal imaging of C2C12s encapsulated in photodegradable hydrogel films and folded in to tubes. The hydrogels were exposed to 365 nm light at 6 or 1 days after encapsulation ((a) and (b) respectively). The color bars depict the z-position of cells stained for actin using rhodamine phalloidin such that the red cells are at the top of the tube and the blue cells are at the opposite end. The red, green and blue axes lines represent the x, y and z-axes, respectively. Only the cells at the gel surface were able to spread. This is depicted in the orthogonal projection of a folded tube in (c). This tube spiraled around itself twice and the red stained cells are shown spreading at the inner surfaces of the folded film. The nuclei were stained with acridine orange (green), which also stains the hydrogel to some extent. The hydrogel thickness can thus be distinguished in the x-z and y-z projections with red stained cells spreading at the gel surfaces. The C2C12 myoblasts spread and started to fuse and form elongated multinucleated cells, characteristic of myotubes (d) and (g). The 3D folded tubes had inner diameters ranging from approximately 1-2 mm inner diameter (lumen view in (f)) and 7-10 mm in length (length view in (e)). The scale bars in (d) and (g) are 50 µm and 1 mm in (e) and (f).

VI. Incorporation of gelatin in shape-change gels for cell culture

Following successful encapsulation of C2C12s in shape changing photodegradable hydrogels, we sought to develop shape changing cell culture scaffolds that can be remodeled by the cells. The first of its kind shape changing scaffold actuated by long-wave UV light allows user-defined control over the timing of shape-change in the presence of cells. Because the PEG-based scaffold is inert, the cell-binding peptide RGD was incorporated to support cell adhesion. We reported both cell seeding and encapsulation on or in the photodegradable gels.[1] However, the cells were not free to spread in the encapsulated state because the PEG-based system is not enzymatically degradable on the time-scale of our experiments. This limited cell spreading to the surface of the folded PEG *o*-NB hydrogels, excluding the cells from spreading through the hydrogel network and forming dense myotubes.

Methacrylamide functionalized gelatin[170] (gelMA) has been shown to support cell encapsulation.[171,172] Importantly, gelatin contains native cells binding domains such as RGD, as well as MMP sensitive sites that cells can degrade to remodel the matrix. Furthermore, Tsang et al. co-polymerized the *o*-NB PEG-based macromer first reported by Anseth and co-workers[36] with gelMA and demonstrated that the photodegradable hydrogels supported 2D cell seeding.[139] We thus sought to generate photodegradable hydrogels incorporating gelMA for shape changing cell culture scaffolds.

Mixing gelMA and PEG at high concentrations requires surfactant

Tsang et al. reported the co-polymerization of gelatin and *o*-NB functionalized PEG macromer. However, they reported low polymer weight percent hydrogels (6% total) that were under 1 kPa and had a swelling ratio of almost 20 for gels with at least

50% *o*-NB by weight (relative to total polymer weight). These gels are not suitable for shape-change applications since the initial, non-degraded, swelling is too high and the modulus is too low to generate sufficient actuation strain for initiating folding following photodegradation. Increasing the polymer weight percent is non-trivial due to high molecular weight PEG's documented propensity for precipitating proteins.[173] We did preliminary measurements to determine the maximum PEG weight percent that could be mixed with 2% gelatin in PBS 1×. For PEGs of molecular weight 2000, 2900 and 3350, we found that we could add a maximum of 15%, 10% and 8% PEG respectively before the solution became cloudy and did not return to being optically transparent after several minutes of heating at 40°C. These results are in agreement with the theory that proteins are precipitated due to the large amounts of swelling that high molecular weight polymers, such as PEG, undergo. The swollen PEG molecules essentially exclude proteins so that they precipitate from solution.

Based on preliminary experiments of mixing gelatin with PEG, we prepared B *o*-NB macromer with PEG 2000 spacer (Alfa Aesar) using the same methods as reported previously.[1] However, we found that 2% gelMA with as low as 3% and up to 8% *o*-NB PEG 2000 macromer added generated cloudy hydrogels after polymerization with 1.5% LAP solution at 405 nm. The gels were cloudy by visual inspection and had distinct phase separation patterns that look like bubbles by phase contrast microscopy (Figure 5.7). Despite the cloudy appearance and poor mixing, we tested whether gels with the same compositions could support C2C12 cell adhesion and spreading. Gels were prepared under aseptic conditions and cells were seeded at 100,000 cells/cm^2. We found there to be poor attachment to both the 2% gelMA gels with 8% *o*-NB PEG and the 5%

gelMA gels with 5% *o*-NB PEG. There was good cell attachment and spreading on the 10% gelMA gels.

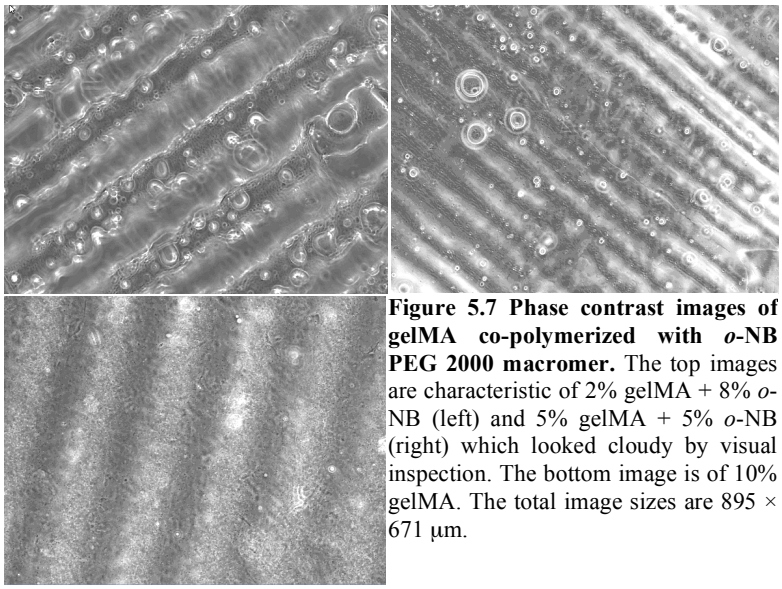

Figure 5.7 Phase contrast images of gelMA co-polymerized with *o*-NB PEG 2000 macromer. The top images are characteristic of 2% gelMA + 8% *o*-NB (left) and 5% gelMA + 5% *o*-NB (right) which looked cloudy by visual inspection. The bottom image is of 10% gelMA. The total image sizes are 895 × 671 μm.

Limited by the mixing of the gelMA and *o*-NB PEG macromers at high enough concentrations to form sufficiently highly crosslinked gels for shape-change, we turned to the use of surfactants to mix the macromers. Sodium dodecyl sulfate (SDS) is an ionic surfactant with amphiphilic properties that allow it to form micelles. We found that the gelMA and *o*-NB macromers could be dissolved in 25% SDS solutions, forming clear solutions. The macromers could also be polymerized using radical initiated chain-growth polymerization to form hydrogels. We next studied the effect of varying relative macromer compositions as well as light dose effect on self-folding.

GelMA and o-NB PEG copolymerized hydrogels shape-change after partial photodegradation. Folding can be tuned by modulating light dose and polymer composition

GelMA *o*-NB gels were co-polymerized at 2:3, 2:5 and 2:7 weight percent ratios (gelMA:*o*-NB) with total polymer content of 15 wt%. Hydrogels of each composition were exposed using collimated 365 nm light at 10, 30, or 50 mW/cm^2 for 600 s (e.g., 6,

18, or 30 J/cm^2). Discs of 4 mm diameter were punched from the partially degraded hydrogel sheet and imaged in PBS immediately after returning to solution and initiating shape-change as well as after 24 h. At least 3 samples were imaged per condition.

Immediately after shape-change, the 2:3 and 2:5 gels had similar amounts of folding for the low light doses compared to each other, yet diverged at the highest light dose, 30 J/cm^2 (Figure 5.8). There was no significant difference between any of the compositions initially for the lowest light dose. Furthermore, initially both the 2:3 and 2:5 gels experienced the most folding for the 18 J/cm^2 light dose, although there was only a significant difference between 2:3 and 2:7 ($p < 0.01$). The 2:7 gels imaged immediately after shape-change were the only group that had decreasing cross-sectional width (or increasing curvature) with increasing light doses, while the others tapered off or had experienced decreased curvature. These results suggest that the lower *o*-NB concentration gels do not attenuate light sufficiently so that the highest light dose generates degradation too far through the gel thickness. This is supported by the larger increase in cross-

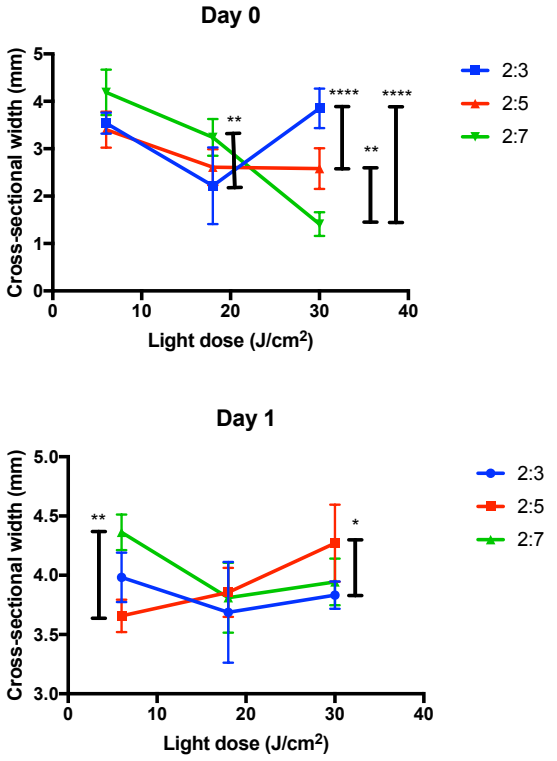

Figure 5.8 Cross-sectional width measurements of self-folded gelMA *o*-NB hydrogels for increasing o-NB concentration from 3% to 7% and increasing light dose. The legend indicates gelMA:*o*-NB macromer wt%:wt%. Samples were imaged at day 0 (immediately after folding, top graph) and day 1 (24 h, bottom graph). Values reported are averaged from at least 3 samples and error bars represent standard deviation. Two-way ANOVA comparison between different compositions gave significant p values for indicated comparisons where *, **, **** are $p < 0.05$, 0.01, 0.0001 respectively.

sectional width for the 2:3 gel for the highest light dose compared to the other two compositions.

All samples relaxed, or had increased cross-sectional width, to some extent after 24 h. The 2:7 gels exposed at 30 J/cm^2 experienced the greatest change in curvature from an average cross-sectional width of 1.4 to 3.9 mm between day 0 and day 1. The smallest cross-sectional width after 1 day was observed for the 2:5 gels at the lowest light dose, 6 J/cm^2. There was a significant difference between 2:5 and 2:7 at the lowest light dose ($p < 0.01$). Furthermore, we found the 2:5 gels to be reasonably robust to handle and transfer between different wells using a modified aspirating pipet. Instead, the 2:7 gels were soft and difficult to handle so that many samples were damaged. Because we are interested in minimizing the light dose required for actuating tube formation and often have to transfer gels for imaging or measurement purposes, we selected the 2:5 gel formulation to further study for optimizing the light-actuated folding.

Optimize folding for minimization of light dose by decreasing thickness

The 2:5 gelMA *o*-NB hydrogels were exposed at a range of 365 nm wavelength light doses from 20-50 mW/cm^2 (e.g., 12-30 J/cm^2). Hydrogels were prepared at 100 or 150 μm thickness to determine whether we could generate tubular structures following equilibration using thinner gels. Previously we observed that the 150 μm gels initially folded sufficiently to generate tubes immediately after shape-change, however, the gels were almost completely flattened after 24 h. Gels of 150 and 100 μm thickness were imaged immediately (day 0), after 24 h (day 1) and 15 days after photodegradation and shape-change. At least 4 samples were measured per condition.

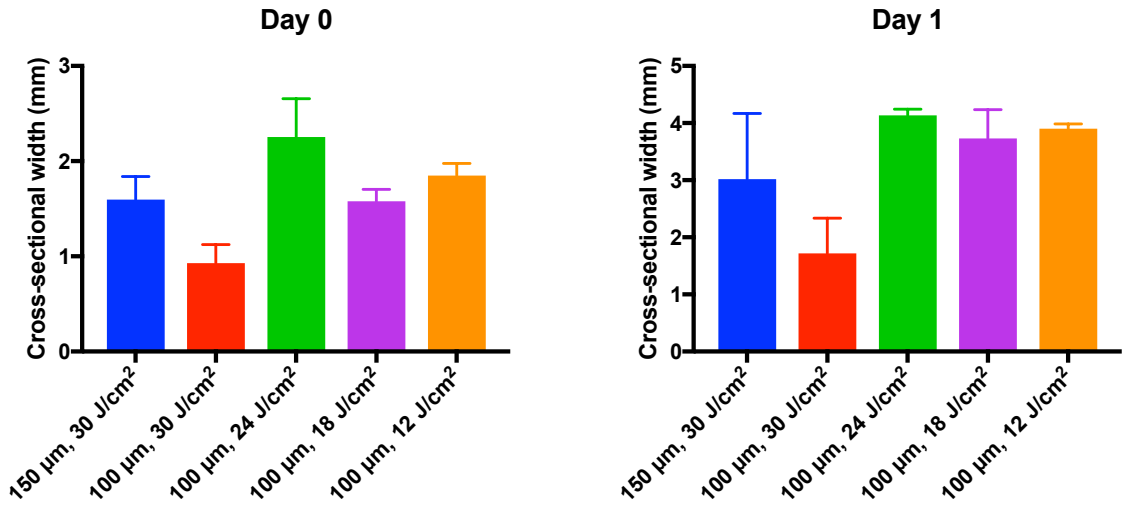

Figure 5.9 Comparison of gelMA *o*-NB folding for different thicknesses and 365 nm light exposures. The cross-sectional width was measured for gels in PBS at day 0 (immediately after shape change, left) and day 1 (24 h after shape change, right). Values are reported as average from at least 4 samples and error bars represent standard deviation)

Immediately after shape-change, the 100 μm thickness gels exposed at 30 J/cm^2 had the greatest extent of folding, and folded in to tubes. Instead, the 150 μm thickness gels exposed at the same light dose experienced less folding. Furthermore, 100 μm thickness gels exposed at lower light doses (18 or 12 J/cm^2) also experienced less folding (Figure 5.9, left). All the gels relaxed to some extent after 24 h (Figure 5.9, right). However, the 100 μm thickness gels exposed at 30 J/cm^2 experienced almost no change in curvature between day 1 and day 15. The 100 μm gels that were exposed at reduced light doses or the 150 μm gels exposed at 30 J/cm^2 largely relaxed and were almost flat by day 15 (Figure 5.10).

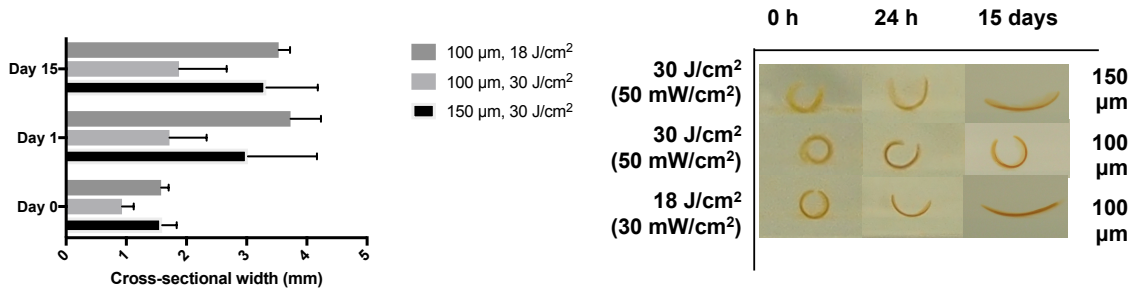

Figure 5.10 Change in cross-sectional width from day 0 to day 15. The 100 µm gels exposed at 30 J/cm^2 had the least change in cross-sectional width after 15 days. Values are reported as average from at least 3 samples and error bars represent standard deviation (left). The gels were imaged immediately after shape change, 24 h and 15 days (right).

Viability of cells seeded on gelMA o-NB hydrogels

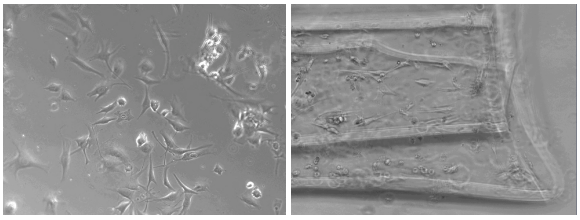

Figure 5.11 C2C12s spreading on gelMA *o*-NB gels polymerized in 25% SDS. The cells spread on (-) shape change gels (left) and (+) shape change gels 4 days after folding was actuated (right).

The purpose of incorporating gelMA in to the photodegradable hydrogels was for cell culture. Although having to add such high SDS content (25 wt%) in order to dissolve the macromers in PBS, precludes encapsulation, we tested the suitability of the scaffolds for cell seeding. C2C12s were seeded on a gelMA *o*-NB gel films. The cells spread and proliferated (Figure 5.11), eventually reaching confluence 5 days after seeding for the gels that were not exposed to UV light ((-) shape-change) demonstrating that the SDS was leached from the hydrogels prior to cell seeding so as to not hinder viability. The gelMA *o*-NB gels that were exposed to 365 nm light (30 J/cm^2), folded in to tubular shapes with C2C12s spreading along the lumen (Figure 5.11, right). Furthermore, cells continued to spread and proliferate and reached confluence 6 days after shape-change.

These results demonstrate that the gelMA *o*-NB system can be used for UV light actuated shape-change in the presence of seeded cells. Although we originally sought to

develop the gelMA *o*-NB system for encapsulation, the requirement of incorporating a strong surfactant, SDS, to mix the macromers precluded encapsulation since SDS is cytotoxic at high concentrations. In the future, the acrylated *o*-NB molecule could be conjugated to gelatin directly. This would eliminate the macromer mixing problem with gelatin and high molecular weight PEGs while imparting the benefits of gelatin (cells can remodel it and spread through the network as well as bind to the native RGD sites) as well as the *o*-NB (for photodegradation, shape-change component).

VII. Summary

In summary, we demonstrate that the photodegradable shape-change system supports cell culture for both 2D seeding and encapsulation. We first demonstrate that C2C12 myoblasts and hAECs can be seeded on initially flat photodegradable hydrogel films. We demonstrate that shape-change can be actuated using 365 nm UV light at a time point of choice. These gels folded in to tubular shapes with cells lining the inner lumen. The hAECs on tubular folded hydrogel films experienced changes in actin cytoskeleton rearrangement compared to cells cultured on flat hydrogel films. We also demonstrate that C2C12s can be encapsulated in PEG *o*-NB hydrogel films using APS/TEMED radical initiators or LAP photoinitiator at 405 nm wavelength light. Viabilities were improved with the LAP photoinitiator compared to APS/TEMED polymerization. Furthermore, we demonstrate for the first time, the photoencapsulation of mammalian cells in photodegradable hydrogel films—using 405 nm light—followed by photodegradation—using 365 nm light. Finally, we present in this chapter, a new material incorporating gelatin with the photodegradable *o*-NB PEG macromer for shape-change

applications. We demonstrate that the gelMA *o*-NB shape-change system can be used for cell seeding followed by shape-change in to tubes.

VIII. Experimental

Materials

Ac-GCGYGRGDSPG-NH_2 peptide (RGD) with N-terminal acetylation and C-terminal amidation was purchased from Genscript (1066.11 g/mol, > 95% purity).

PEG o-NB gels for C2C12 cell seeding

Self-folding hydrogels for cell seeding and encapsulation were prepared by first dissolving PEGDA (22.5 mg, 5.5 mmol) and B *o*-NB PDM (50.0 mg, 10.7 mmol) in PBS (200 μL). APS and TEMED stock solutions were made in PBS (1.25 M and 0.63 M respectively). The RGD-PEG solution was prepared by dissolving PEGDA (30.8 mg, 7.5 mmol) and RGD (8.0 mg, 7.5 mmol) in 200 μL PBS and pre-reacted by Michael addition for at least 30 minutes. All solutions were sterile filtered with 0.22 μm filter (Millex). Hydrogels were made with 21.5 wt% (w/w) and 2:1 PDM:PEGDA macromer. For 50 μL pre-gel solutions, 8 μL of RGD-PEG stock solution was added with no further purification.

The stock solutions of PDM:PEGDA and RGD-PEG were combined and vortexed for thorough mixing. APS and TEMED were added last at final concentrations of 25 and 12.5 mM respectively in order to initiate radical polymerization. The solution was polymerized between glass slides separated by No. 1 coverslip spacers (150 μm) and allowed to gel for 30 minutes under aseptic conditions. The gels were then released and equilibrated in CGM at 37°C and 5% CO_2 overnight. Once equilibrated, samples were

punched using a sterile 4 mm diameter biopsy punch and placed at the bottom of individual 96-wells. C2C12s were suspended in phenol-red free CGM. Phenol-red free CGM was made using base DMEM without phenol red or L-glutamine (HyClone), supplemented with L-Glutamine (Life Technologies), fetal bovine serum and penicillin-streptomycin. A suspension of 5000 cells/100 μL was seeded on top of hydrogels in 96-wells (15,625 cells/cm^2). The cells were allowed to settle on the hydrogels overnight before UV exposure.

PEG o-NB gels for hAEC seeding

Hydrogels were prepared similarly as for C2C12 seeding except that APS and TEMED stock solutions were prepared at 1.0 M and 0.5 M respectively and the final concentration in the pre-polymer solution was 0.1 and 0.05 M respectively. The pre-polymer solutions were polymerized between glass slides separated by 100 μm spacers for 15 minutes. Following polymerization, hydrogels were released from the glass slides and 8-9 mm length squares were cut and transferred to individual wells in sterile 24-well plates. The hydrogel films were equilibrated in sterile water and then disinfected with 70% ethanol for 30 minutes. They were next washed with water 3× and incubated in endothelial cell complete growth medium overnight. The following day, hAECs were suspended at 57,000 cells/ 300 μl endothelial cell growth medium and 300 μl of the cell suspension was added per well for 30,000 cells/cm^2. The cells were allowed to settle on the hydrogels overnight before UV exposure.

C2C12 cell encapsulation in PEG o-NB gels using APS and TEMED initiators

C2C12s were suspended in a solution of PDM:PEGDA (2:1 molar ratio) and RGD-PEG. Next, the APS was added and mixed well by pipetting up and down quickly

and then TEMED was added and mixed to obtain final concentrations of 32 and 16 mM respectively. The pre-polymer suspension was combined with cells (5×10^6 cells/mL), quickly pipetted between glass slides separated by No. 1 coverslip spacers (150 μm) and allowed to gel for 7.5 minutes under aseptic conditions. The polymerization time and APS and TEMED concentrations were optimized for C2C12 viability and in order to fabricate hydrogels in less than 15 minutes. The gels were then released and discs were quickly punched using a sterile 4 mm diameter biopsy punch. The discs were equilibrated in CGM for at least one hour. The gel discs were placed at the bottom of individual 96-wells and 100 μL phenol-red free CGM was added to each well. Flat gels were either: (a) imaged to determine cell viability with no UV exposure or (b) exposed to UV light in order to induce folding and then imaged to determine cell viability. In order to more specifically determine the effect of the UV light on the cells, viability was determined at the surface of the hydrogel closest to the UV light incidence (where the effect should be greatest).

Macromer toxicity determination

In order to determine macromer cytotoxicity, C2C12s were seeded on 96 well plates at 5,000 cells/cm^2. After allowing cells 3 hours to attach to the well plates, they were challenged with the macromer solution (i.e. PDM, PEGDA and RGD-PEG in DPBS) at the same concentrations used for C2C12 encapsulation (but omitting the radical initiating system APS/TEMED) for 7.5 minutes. Plated cell viability was determined using Live-Dead™ (Life Technologies) fluorescence imaging to be 93 ± 7.1% (n=6) compared to 100% for cells in either complete growth medium (n=3) alone or DPBS alone (n=3).

APS and TEMED toxicity determination

C2C12s were seeded on 96 well plates at 5,000 cells/cm^2. Cells were exposed to 5, 15, 30 or 50 mM APS or 2.5, 7.5, 15 or 25 mM TEMED for 1 minute. After 1 minute plated cell viability was determined using Live-Dead™ (Life Technologies) fluorescence imaging according to the manufacturer protocol. The viability for all APS conditions was 0%. The viability for 2.5, 7.5, 15 or 25 mM TEMED was > 90%, > 85%, > 80% or 0% respectively. These results suggest that the main cause of cytotoxicity were the radicals. The TEMED base initiator caused a moderate decrease in cell viability. However, it did not fully account for the decreased viabilities observed for C2C12 encapsulation using 32 and 16 mM APS and TEMED concentrations respectively.

C2C12 cell encapsulation PEG o-NB gels using LAP photoinitiator

A 1% LAP (Sigma Aldrich) solution was prepared by dissolving 10 mg in 990 μl phenol red free DMEM (HyClone). A PEG *o*-NB solution was prepared by dissolving PEGDA (89.2 mg, 22 mmol) and B *o*-NB PDM in 708 μl of 1% LAP solution. An RGD-PEG solution was prepared by dissolving RGD (11.7 mg, 11.0 mmol) and PEGDA (43.4 mg, 11 mmol) in 213 μl LAP solution. The RGD-PEG solution was pre-reacted by Michael addition for at least 30 minutes. All solutions were sterile filtered with a 0.22 μm filter (Millex). Hydrogels were made at 25 or 21.5 wt% (w/w) and 2:1 molar ratio PDM:PEGDA macromer. For 25 wt% hydrogels, 20 μl PEG *o*-NB solution and 3.4 μl RGD-PEG solution were mixed well by repeated pipetting. The 21.5 wt% hydrogels were prepared by mixing 17.2 μl PEG *o*-NB solution with 2.8 μl phenol red free DMEM and 3.4 μl RGD-PEG well.

For viability experiments, C2C12 or hFM cells were prepared for encapsulation by suspending 24,000 cells in complete growth medium in individual eppendorf tubes. The cells were centrifuged, the medium was aspirated and the pellet was next resuspended in 23.4 μl of the 21.5 or 25 wt% macromer suspension (for approximately 1×10^6 cells/ml). Then 10 μl were pipet on glass slides between 100 μm spacers. Then an 18 mm diameter coverslip was placed on top of the cell-macromer suspension. The solutions were exposed at 405 nm using an Omnicure 1000 mercury vapor lamp (EXFO) at 10 mW/cm^2 for 180 s. The coverslip was quickly lifted and the hydrogels adhered to the coverslip. The hydrogel on the coverslip was transferred to a 12-well plate with the glass side down with 1 ml complete growth medium. Following encapsulation, cells were incubated under normal growth conditions overnight.

For the 7-day C2C12 encapsulation experiments, cells were prepared for encapsulation by suspending 70,200 cells in complete growth medium in individual eppendorf tubes. The cells were centrifuged and the medium was aspirated and the cell pellet was resuspended in 23.4 μl of the 25 wt% macromer suspension (3×10^6 cells/ml). Hydrogels were next polymerized the same way as for the above viability experiments.

Viability determination using Live/Dead™

Cell viability was determined using mammalian Live-Dead™ assay (Life Technologies). The gels were washed with PBS with calcium and magnesium and incubated with 2 μM calcein AM and 4 μM ethidium homodimer-1 for at least 30 minutes at 37°C prior to imaging with a fluorescence microscope (10×, Axiovert Observer Z1, Zeiss). Live (green) and dead (red) cells were counted using the cell counter plugin in FIJI.

Photodegradation in presence of cells for inducing tube formation

C2C12s seeded with shape-change actuated at 1 or 3 days after seeding

Circular gel samples seeded with C2C12s were exposed to UV light at different time points to demonstrate folding in the presence of cells. Before and after exposures, samples were imaged with a phase contrast microscope (10×, Axiovert Observer Z1, Zeiss). The samples were exposed to 20, 40 or 60 mW/cm^2 UV light for 600 s in 96-wells with 100 μL of C2C12 phenol-red free CGM. After exposures, 50 μL of the medium was removed and replaced by 150 μL of fresh medium. The next day, the samples were transferred from 96-wells to 24-wells with 750 μL of medium, which was changed every three days. Samples were exposed either 1 or 3 days after C2C12 seeding and cultured for either 6 or 3 days after UV exposure, respectively. At the end point of the culture, which was 7 days after seeding, the actin cytoskeleton and cell nuclei of the C2C12s on the folded gels were stained. Before staining, the samples were imaged with a digital camera (Olympus E-PL6) to determine extent of folding.

hAECs seeded with shape-change actuated 1 day after seeding

Before and after exposures, samples were imaged with a phase contrast microscope (10×, Axiovert Observer Z1, Zeiss). One day after cell seeding, the endothelial cell growth medium was exchanged for 200 μl phenol red free medium supplemented with 1% penicillin-streptomycin. This volume was just enough to cover the top surface of the hydrogels, preventing them from floating up during the light exposure. The hydrogels were exposed through the bottom of the 24-well plate at 40 mW/cm^2 for 300 s (365 nm wavelength UV light). Folding in to tubes was initiated by adding 400 μl

endothelial cell growth medium. The medium was exchanged 3× (200 μl per wash) to remove degraded macromer. The following day cells were again imaged by phase microscopy prior to staining the actin cytoskeleton and nuclei. A subset of samples was also imaged with a macro lens (Micro-Nikkor 55 mm f/2.8) attached to a digital camera (Olympus E-PL6) to determine the extent of folding.

C2C12s encapsulated in photodegradable hydrogels using APS and TEMED followed by same day shape-change actuation

Samples were exposed in 96-wells to 38, 62, 74 or 84 mW/cm^2 UV light for 600 s. Immediately after exposure, gels that had not started folding were manually released from the well bottom. Cells encapsulated in both flat and folded gels were imaged using phase contrast microscopy (10×, Axiovert Observer Z1, Zeiss).

C2C12s photoencapsulation in photodegradable hydrogels followed by day 1 or 6 shape-change actuation

Samples were exposed to 365 nm wavelength light from the bottom of 12-well plates at 20 mW/cm^2 for 180 or 240 s. Prior to exposure, the complete growth medium was exchanged for 1 mL phenol red free medium supplemented with 1% penicillin-streptomycin. A subset of gels was exposed 1 day after encapsulation (n=5) and 7 gels were exposed 6 days after encapsulation. Immediately after exposure, gels that had not started folding were manually released from the well bottom with a disinfected spatula. Cells encapsulated in both flat and folded gels were imaged using phase contrast microscopy (10×, Axiovert Observer Z1, Zeiss).

Cell culture

C2C12 mouse myoblasts cells were obtained from the American Type Culture Collection (ATCC). The 2nd passage (P2) cells were thawed and expanded using a standard cell culture protocol according to ATCC's recommended culture methods. The cells were grown in complete growth medium (CGM) made up of high glucose DMEM (Corning) supplemented with 10% fetal bovine serum (Corning) and 1% Penicillin-Streptomycin (Life Technologies). The cells were collected from tissue culture flasks using Trypsin-EDTA (Corning) and used for either hydrogel seeding or encapsulation experiments at P2-P3.

Human fetal muscle cells were obtained from the UCLA Center for AIDS Research (CFAR) Gene and Cellular Therapy Core using institutional review board (IRB)-approved de-identified and consented human fetal tissues. Use of human tissues was IRB exempt by the UCLA Office of the Human Research Protection Program (IRB no. 15-000959). Skeletal muscle cells were isolated from quadriceps according to the protocol described in Hicks et al.[174] and FACS (fluorescence activated cell sorting) enriched for (-) CD45, (-) CD31, (-) CD235A, (+) ERBB3, (+) NGFR. Adherent cells were cultured in complete growth medium (Ham's F12 basal medium supplemented with 10% fetal bovine serum, 10 ng/ml EGF, 5 ng/ml bFGF, insulin, dexamethasone and 1% penicillin-streptomycin.)

Human aorta endothelial cells were generously donated from the lab of Song Li (UCLA Bioengineering) at passage 11. Adherent cultures were expanded in supplemented endothelial cell medium containing 5% FBS, 1% ECGS and 1%

penicillin/streptomycin (ScienCell). Cells were collected for seeding using Trypsin-EDTA (Corning) and used for hydrogel seeding at P13.

Immunostaining and gel embedding

Hydrogels were prepared for immunostaining by washing with PBS 3× and then fixing with formalin (1:10 dilution, Fisher) for 15-20 minutes. Cells were next permeabilized with 0.1% Triton X-100 (Fisher) in PBS buffer for 5-10 minutes and washed twice with 0.05% TWEEN® 20 (Acros), followed by blocking with 5% BSA overnight at 4°C. Actin cytoskeleton was stained with 1:500 TRITC-phalloidin (Millipore) in 0.5% BSA solution for 1 h in room temperature for the C2C12 cell seeding on PEG o-NB samples or with rhodamine phalloidin (Cytoskeleton) at 3.5 μl per 500 ml 0.5% BSA blocking buffer for all other samples. Nuclei were counterstained with 1:1000 acridine orange (Fisher) in 1% BSA solution for 30 minutes in room temperature for the C2C12 cell seeding on PEG o-NB samples or at 1:2000 in 0.5% BSA blocking buffer for 30 minutes for all other samples.

Since folded hydrogels are floating in solution, they need to be fixed spatially for imaging sections and tiled images. Following immunostaining, folded gels were embedded in 0.2% agar by adding equal volume of 0.4% agar to folded hydrogels in PBS. The samples were stored at 4°C until imaging.

Microscopy

Widefield phase contrast and fluorescence microscopy imaging was done with 10×, Axiovert Observer Z1, Zeiss.

Confocal images were collected with an EC Plan-Neofluar 10×/0.30 M27 objective mounted on a laser scanning microscope (Zeiss LSM 780) at the UCLA BSCRC Microscopy Core imaging facility.

Image processing for illustration purposes was done using both Zen 2012 SP1 software (Zeiss) and FIJI ImageJ[105].

Imaging of folded samples

Folded tubular samples were imaged in PBS with a macro lens (Micro-Nikkor 55 mm f/2.8) attached to a digital camera (Olympus E-PL6). Black silicon nitride balls of known diameter (1/16", McMaster-Carr) were used as size references and imaged together with each sample. From the images, the cross-sectional width of the lumen view and maximum length of length view of folded tubular samples was measured using GIMP 2.8 software.

Cell width and density analysis

Cell width and density were measured for hAECs on (-) and (+) shape-change photodegradable hydrogels using confocal fluorescence images. The width was measured across the shorter side of mononuclear cells using the measurement tool in FIJI. Boundaries were distinguished by changes in actin fiber alignment. Average and standard deviation values are reported. The cell density was determined from 515×1014 pixel×pixel (428×842 μm×μm) images of cell nuclei. The nuclei were counted in FIJI using the cell counter plugin. Values are reported as number of nuclei/100 μm^2 area.

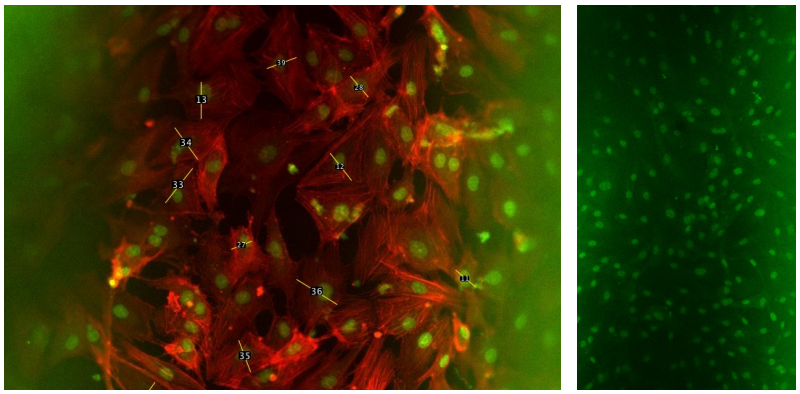

Figure 5.12 Confocal fluorescence images used to calculate cell width and density. The cell widths were measured along the shorter of the principal lengths across mononuclear cells (left). The nuclei were counted per known rectangular cross-sectional areas for the density measurements (right).

Orientation analysis

Orientation analysis was done using either nuclei or actin staining images of hAECs seeded on photodegradable hydrogels. The directionality plugin in FIJI was used to analyze 3 images from each group (e.g. (-) and (+) shape-change conditions)). We ran a Fourier components analysis for each image and collected the histograms of the orientation angles. The plugin generates statistics of the highest peak (most common orientation angle) fitted by a Gaussian function. We collected the results summarizing dispersion angle (e.g., standard deviation of the Gaussian), amount (e.g. the sum of the histogram densities between the ± standard deviation boundaries) and the goodness of the Gaussian fit ranging from 0 to 1 where 1 is the best fit and 0 is the worst. We also reported the modality of the Gaussian fit from the histogram output whether the fit had one peak (mono) or two peaks (dual).

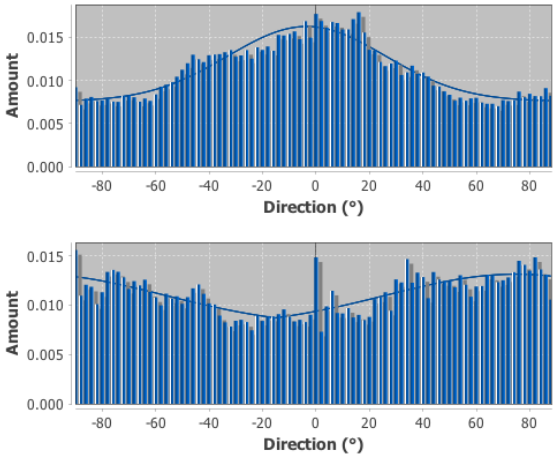

Figure 5.13 Directionality analysis histogram for actin orientation. The top and bottom graphs are representative histograms of (-) and (+) shape change samples.

Gelatin and PEG mixing experiments

Gelatin from porcine skin, type A, 300g bloom (Sigma) was dissolved in PBS at 2 wt% by heating to 40°C. Next PEG 2000 (Alfa Aesar), PEG 4000 (MW measured to be 2900 by GPC using PEG standards for calibration, Mallinckrodt), or PEG 3350 (Integra Chemical Company) were added until the solution became cloudy and did not return to transparent again.

Gelatin methacrylamide synthesis

Gelatin methacrylamide (gelMA) was synthesized using the same procedure as described in[171] for high conversion of amines. The conversion was monitored by H^1 NMR disappearance of the lysine peaks. Approximately 80-90% conversion was calculated using the ratio of phenylalanine:vinylic proton peaks.

Hydrogel polymerization with gelMA and o-NB PEG 2000 macromer

GelMA was dissolved in PBS at 40°C in PBS at 2 wt%. Then, *o*-NB macromer dimer with PEG 2000 spacer was added at 5 wt% or 8 wt%. LAP photoinitiator was then

added to the polymer mix for final 1 wt% solution. Polymerization was initiated using 405 nm filtered UV light at 12.5 mW/cm^2 for 300 s.

Hydrogel polymerization with gelMA and o-NB PEG 3350? macromer using surfactant (different polymer contents and thickness)

GelMA *o*-NB hydrogels with different macromer concentrations were prepared by dissolving gelMA and *o*-NB in 25% SDS at 50°C for about 1 h until transparent. The 2:3 (gelMA:*o*-NB) gels were prepared by dissolving gelMA (12.6 mg) with *o*-NB PEG 2000 spacer (18.4 mg) in 136.5 μl of 25% SDS. Next, 21 μl 1.0 M APS and 21 μl 0.5 M TEMED were added and mixed well. The 2:5 gels were prepared by dissolving gelMA (8.4 mg) with 20.9 mg *o*-NB PEG 2000 spacer (18.4 mg) in 126.8 μl of 25% SDS. Then 19.5 μl 1.0 M APS and 19.5 μl 0.5 M TEMED were added to initiate polymerization and mixed well. The 2:7 gels were prepared by dissolving 6.5 mg gelMA with 22.8 mg *o*-NB PEG 2000 spacer in 126.8 μl 25% SDS solution. Then 19.5 μl 1.0 M APS and 19.5 μl 0.5 M TEMED were added to initiate polymerization and mixed well. Hydrogels were polymerized on glass slides between 150 μm or 100 μm spacers (as indicated in main text) at 40°C for 15 minutes. After 15 minutes, the reaction was quenched with water and gels were transferred to 12 well plates for overnight equilibration prior to photodegradation.

GelMA o-NB hydrogel film photodegradation for actuating shape-change

Hydrogel films were placed on a glass slide covered with a 25 mm × 25 mm coverslip. Hydrogels were maintained hydrated with PBS during exposure. The gels were exposed to collimated 365 nm wavelength light using an Omnicure 1000 mercury vapor

lamp (EXFO) for 600 s at 10-50 mW/cm^2 (as indicated in the main text). Following photodegradation, 4 mm diameter discs were punched using a biopsy punch and discs were transferred to a PBS bath for folding and imaging. Samples were imaged immediately after degradation and folding (day 0), 1 day (24 h) after folding, or 15 days later (as indicated in the main text) using a digital camera (Olympus) with a macro lens (Micro-Nikkor 55 mm f/2.8) attached. At least 3 samples were imaged per condition. Values are reported as average and standard deviation. Two-way analysis of variance (ANOVA) was run in GraphPad Prism Version 7.0 to compare the 2:3, 2:5, and 2:7 gelMA:*o*-NB wt:wt% for each light exposure condition.

C2C12s seeded on gelMA o-NB PEG hydrogels

GelMA o-NB PEG hydrogels were again co-polymerized in 25% SDS at 2:5 weight% ratio (gelMA:*o*-NB) and final 15 wt% polymer content total. The macromer, APS and TEMED solutions were sterile filtered prior to use. Hydrogels were polymerized on glass slides between 100 μm spacers and covered with a coverslip to fabricate 100 μm thickness films, before equilibration. Samples were equilibrated in complete C2C12 growth medium overnight.

C2C12s were collected at passage 3 and seeded at 50,000 cells/cm^2 in complete growth medium. The cells were allowed time to attach to the hydrogels. Cells seeded on gels were imaged by phase microscopy (10×, Axiovert Observer Z1, Zeiss) before and after shape-change. The medium was exchanged for phenol red free medium (Hyclone) immediately before UV exposure. Photodegradation was initiated 1 day after seeding using collimated 365 nm light at 50 mW/cm^2 for 600 s from the bottom of the well plate (opposite cell seeding side).

Chapter 6

CONCLUSIONS AND FUTURE DIRECTIONS

I. Conclusions

Motivation and background

The dissertation begins with our general motivation and rationale for developing photodegradable shape changing hydrogels for cell and tissue culture. In Chapter 2 we introduce the role of the extracellular matrix and discuss how hydrogels can be engineered to recapitulate some of the roles of the native in vivo extracellular matrix for in vitro applications. We also outline several studies that suggest that the extracellular matrix plays an active role in cell response, focusing on its significance in regeneration and development. With a particular focus on development, we turn our attention towards extracellular matrix dependent mechanisms that guide shape-change during embryogenesis. Our aim is to highlight that, although poorly understood, changes in tissue shape, have an effect on cell behavior. This is where we expect that photodegradable shape changing hydrogels may be able to play a role as tools to help study the effects of shape-change and curvature on cell behavior.

Synthesis and post-polymerization photopatterning of shape-changing hydrogel films

In Chapter 3, we review hydrogel swelling and elasticity theory as well as photodegradation as a method for changing hydrogel crosslink density post-equilibration. We also introduce variables that can be tuned in a photodegradable system for modulating changes in through-depth gradient crosslink density and resulting swelling induced shape-change. After establishing the physical framework for photodegradation actuated shape-change, we discuss our proof of concept approach for bending hydrogels

using long wave UV light. Finally, we systematically empirically study variables for modulating the amount of curvature.

Patterning arbitrary curvatures and shapes, mimicking tissue geometries observed during morphogenesis and development

In Chapter 4, we discuss how planar sheet geometry and light patterning can be used to control bending directions and resulting curvatures. We begin with the simplest case of generating hollow tubular shapes whose curvatures can mimic curvatures observed in hollow tubes of the digestive tract and blood vessels. We next demonstrate how negative Gaussian curvatures can be generated and draw comparisons to generation of similar curvatures during heart development. Next, we generate folds in sheets resulting in non-periodic rippling. The creation of rippled sheets with mixed, arbitrary curvatures demonstrates the flexibility of photodegradation-induced shape-change compared to materials that are pre-programmed with the inhomogeneities that generate shape-change. We also draw comparisons to rippled elastic sheets in the body, such as the dorsal mesentery. Finally, we demonstrate that we can combine patterning of micro-scale topographical features with macro-scale bending in the same hydrogels by tuning the light dose.

In Chapter 5, we demonstrate shape-change in the presence of mammalian cells. We show that cells can either be seeded on planar sheets or encapsulated within the hydrogel. We also demonstrate that, like in the acellular system, the amount of folding can be tuned by modulating the light dose and that shape-change can be actuated at arbitrary time points, upon exposure to UV light. We also discuss preliminary results demonstrating differences in human endothelial cell behavior on flat sheets compared to

cells on shape-changed sheets. We provide evidence that the cells on flat sheets have characteristics similar to cells under pathologic conditions, while cells on tubular sheets have characteristic actin arrangement of endothelial cells lining large vessels under normal physiological flow conditions. These results hopefully provide a launching point for future research on the topic.

II. Future directions

We hope that the work discussed in this dissertation is only the beginning of continuing research on shape changing photodegradable hydrogel scaffolds. This dissertation establishes the concept and introduces a framework for generating different shapes from flat hydrogels, with or without living cells. Accordingly, there is work yet to be done towards developing the system for applications with and without living cells.

One area of research that should be further explored is on the effects of the solution on shape-change. We found that the partially degraded hydrogels swelled much more in distilled water compared to buffered water. The changes in swelling actuated strain led to 2-3 fold decrease in cross-sectional width in DI water compared to 1× PBS (depending on the exposure conditions). In addition to being sensitive to ion concentration, the hydrogels should also be sensitive to pH near the pKa of pendant carboxylic acids (i.e., ca. pH 4-5). These shape-changing hydrogels could be developed for sensor applications where the curvature could be calibrated for determining buffer ion concentration or small pH windows ca. 4-5. Because the change in curvature is reversible, several solutions could be analyzed with a single gel. This same concept could also be applied towards moving devices or robots in gradient solutions.

Furthermore, we demonstrate shapes with different mean and Gaussian curvatures, and only start to explore mixed curvatures. The development of a finite element model for predicting bending direction should be developed to instruct design of binary or even gradient photomasks. Predictive models can also be used to determine the bending direction for different flat, 2D sheet geometries. In this way, more precise curvature tuning can be achieved in order to generate shapes with increasing complexity. Furthermore, although the photodegradation reaction is not reversible, by photopatterning select regions on the same sheet, sequentially changing curvatures can be programmed on the same sheet. This can increase the sophistication of scaffolds used for studying dynamic shape-change events during morphogenesis and development. The series of experiments discussed in Chapter 4 demonstrate a series of curvatures and shapes that are relevant for tissue engineering. Furthermore, different curvatures and shapes could be generated by spatially patterning light at different positions, doses and wavelengths. This capability expands the use of the photodegradable shape-changing hydrogel platform for preparing a wide array of tissue engineering and wound healing relevant shapes. We demonstrate curvatures ranging from approximately 0.5 to 1 mm^{-1}. However, we also demonstrated that the 2D sheet dimensions, and light patterning could be used to modulate direction and amount of curvature. Development of a finite element model to forecast swelling induced shape change resulting from photodegradation will allow the prediction of light patterning and 2D sheet geometries to generate the desired shape.

That brings us to future directions regarding the use of photodegradable shape changing hydrogels for cell and tissue culture. We introduce gelMA and *o*-NB PEG co-polymer hydrogels in an effort to create shape-changing scaffolds that are not only

photodegradable, but that the cells can also remodel. However, those hydrogels required a cytotoxic surfactant for mixing the macromers, thus excluding encapsulation as a viable option. Incorporation of the *o*-NB functional group directly on gelatin could eliminate the PEG mixing problem, allowing for encapsulation of cells during the polymerization process. This would open opportunities for encapsulation of muscle cells that could not only form myotubes along the tube lumen, but also eventually completely degrade the matrix and form a dense muscle tube. Of course, other cell types could be used as well. Another interesting avenue will be co-culture studies where cells, such as mesenchymal or smooth muscle cells, are encapsulated and another cell type, such as endothelial cells, are seeded prior to actuating shape-change. Studying the co-cultures in the folded and flat state may provide insight into the effects of curvature or shape-change on co-cultured cell behavior. Finally, we demonstrate that human endothelial cells seeded on photodegradable sheets can be folded in to tubes. The cells demonstrated changes in actin arrangement in response to the shape-change by adopting characteristics of cells under physiological laminar flow conditions (without exposure to laminar flow). If the cells indeed mature under the shape change conditions without need for laminar flow conditions, this may offer a method for generating tissue engineered endothelial cell-lined tubes. These preliminary results warrant further investigation in to the mechanism of the change in phenotype compared to cells on flat hydrogels. Studies suggest that changes in NO production are correlated with similar phenotypic changes,[156] offering a potential route of investigation.

We discuss here only a few of several avenues for continuing investigations with shape-changing photodegradable hydrogel scaffolds. We intend for the preliminary

findings discussed in this dissertation to (i) serve as a guide for further research in the field as well as to (ii) turn attention towards shape changing materials for tissue culture and finally (iii) serve as a tool for studying effects of geometry and mechanics on cell behavior.

REFERENCES

1. Kapyla, E.; Delgado, S. M.; Kasko, A. M., Shape-Changing Photodegradable Hydrogels for Dynamic 3D Cell Culture. *ACS Appl Mater Interfaces* **2016,** *8* (28), 17885.
2. Trinh, L. A.; Stainier, D. Y., Fibronectin regulates epithelial organization during myocardial migration in zebrafish. *Dev Cell* **2004,** *6* (3), 371.
3. Davis, N. M.; Kurpios, N. A.; Sun, X.; Gros, J.; Martin, J. F.; Tabin, C. J., The chirality of gut rotation derives from left-right asymmetric changes in the architecture of the dorsal mesentery. *Dev Cell* **2008,** *15* (1), 134.
4. Kurpios, N. A.; Ibanes, M.; Davis, N. M.; Lui, W.; Katz, T.; Martin, J. F.; Izpisua Belmonte, J. C.; Tabin, C. J., The direction of gut looping is established by changes in the extracellular matrix and in cell:cell adhesion. *Proc Natl Acad Sci U S A* **2008,** *105* (25), 8499.
5. Savin, T.; Kurpios, N. A.; Shyer, A. E.; Florescu, P.; Liang, H.; Mahadevan, L.; Tabin, C. J., On the growth and form of the gut. *Nature* **2011,** *476* (7358), 57.
6. Shyer, A. E.; Huycke, T. R.; Lee, C.; Mahadevan, L.; Tabin, C. J., Bending gradients: how the intestinal stem cell gets its home. *Cell* **2015,** *161* (3), 569.
7. Jamal, M.; Kadam, S. S.; Xiao, R.; Jivan, F.; Onn, T. M.; Fernandes, R.; Nguyen, T. D.; Gracias, D. H., Bio-Origami Hydrogel Scaffolds Composed Of Photocrosslinked PEG Bilayers. *Adv Healthcare Mater* **2013,** *2*, 1142.
8. Welsh, I. C.; Thomsen, M.; Gludish, D. W.; Alfonso-Parra, C.; Bai, Y.; Martin, J. F.; Kurpios, N. A., Integration of left-right Pitx2 transcription and Wnt signaling drives asymmetric gut morphogenesis via Daam2. *Dev Cell* **2013,** *26* (6), 629.
9. Soffers, J. H.; Hikspoors, J. P.; Mekonen, H. K.; Koehler, S. E.; Lamers, W. H., The growth pattern of the human intestine and its mesentery. *BMC Dev Biol* **2015,** *15*, 31.
10. Moorman, A.; Webb, S.; Brown, N. A.; Lamers, W.; Anderson, R. H., Development of the Heart: (1) Formation of the Cardiac Chambers and Arterial Trunks *Heart* **2003,** *89* (7), 806.
11. Xue, C.; Wong, D. Y.; Kasko, A. M., Complex Dynamic Substrate Control: Dual-Tone Hydrogel Photoresists Allow Double-Dissociation Of Topography And Modulus. *Adv Mater* **2014,** *26*, 1577.
12. Randall, C. L.; Gultepe, E.; Gracias, D. H., Self-Folding Devices And Materials For Biomedical Applications. *Trends Biotechnol* **2012,** *30*, 138.
13. Stoychev, G.; Zakharchenko, S.; Turcaud, S.; Dunlop, J. W.; Ionov, L., Shape-programmed folding of stimuli-responsive polymer bilayers. *ACS Nano* **2012,** *6* (5), 3925.
14. Gracias, D. H., Stimuli Responsive Self-Folding Using Thin Polymer Films. *Curr Opin Chem Eng* **2013,** (2), 112.
15. Elbaum, R.; Zaltzman, L.; Burgert, I.; Fratzl, P., The role of wheat awns in the seed dispersal unit. *Science* **2007,** *316* (5826), 884.
16. Oliver, K.; Seddon, A.; Trask, R. S., Morphing in nature and beyond: a review of natural and synthetic shape-changing materials and mechanisms. *J Mater Sci* **2016,** *51* (24), 10663.
17. Burgert, I.; Fratzl, P., Actuation systems in plants as prototypes for bioinspired devices. *Philos Trans A Math Phys Eng Sci* **2009,** *367* (1893), 1541.

18. Fratzl, P.; Elbaum, R.; Burgert, I., Cellulose fibrils direct plant organ movements. *Faraday Discuss* **2008,** *139*, 275.
19. Forterre, Y.; Skotheim, J. M.; Dumais, J.; Mahadevan, L., How the Venus flytrap snaps. *Nature* **2005,** *433* (7024), 421.
20. Kim, J.; Hanna, J. A.; Byun, M.; Santangelo, C. D.; Hayward, R. C., Designing Responsive Buckled Surfaces By Halftone Gel Lithography. *Science* **2012,** *335*, 1201.
21. Bende, N. P.; Evans, A. A.; Innes-Gold, S.; Marin, L. A.; Cohen, I.; Hayward, R. C.; Santangelo, C. D., Geometrically Controlled Snapping Transitions In Shells With Curved Creases. *Proc Natl Acad Sci U S A* **2015,** *112* (36), 11175.
22. Erb, R. M.; Sander, J. S.; Grisch, R.; Studart, A. R., Self-Shaping Composites With Programmable Bioinspired Microstructures. *Nat Commun* **2013,** *4*, 1712.
23. Schoenwolf, G. C.; Smith, J. L., Mechanisms Of Neurulation: Traditional Viewpoint And Recent Advances. *Development* **1990,** *109*, 243.
24. Lin, C. J.; Lin, C. Y.; Chen, C. H.; Zhou, B.; Chang, C. P., Partitioning The Heart: Mechanisms Of Cardiac Septation And Valve Development. *Development* **2012,** *139*, 3277.
25. Nawroth, J. C.; Lee, H.; Feinberg, A. W.; Ripplinger, C. M.; McCain, M. L.; Grosberg, A.; Dabiri, J. O.; Parker, K. K., A Tissue-Engineered Jellyfish With Biomimetic Propulsion. *Nat Biotechnol* **2012,** *30*, 792.
26. Timoshenko, S., Analysis Of Bi-Metal Thermostats. *J Opt Soc Am* **1925,** *11* (3), 233.
27. Ionov, L., Hydrogel-Based Actuators: Possibilities And Limitations. *Mater Today* **2014,** *17* (10), 494.
28. Liu, Y.; Genzer, J.; Dickey, M. D., "2D or not 2D": Shape-programming polymer sheets. *Prog Polym Sci* **2016,** *52*, 79.
29. Vannozzi, L.; Yasa, I. C.; Ceylan, H.; Menciassi, A.; Ricotti, L.; Sitti, M., Self-Folded Hydrogel Tubes for Implantable Muscular Tissue Scaffolds. *Macromol Biosci* **2018**.
30. Herbert, K. M.; Schrettl, S.; Rowan, S. J.; Weder, C., 50th Anniversary Perspective: Solid-State Multistimuli, Multiresponsive Polymeric Materials. *Macromolecules* **2017,** *50* (22), 8845.
31. Kwag, H. R.; Serbo, J. V.; Korangath, P.; Sukumar, S.; Romer, L. H.; Gracias, D. H., A Self-Folding Hydrogel In Vitro Model For Ductal Carcinoma. *Tissue Eng Part C Methods* **2016,** *22*, 398.
32. Hughes, A. J.; Miyazaki, H.; Coyle, M. C.; Zhang, J.; Laurie, M. T.; Chu, D.; Vavrusova, Z.; Schneider, R. A.; Klein, O. D.; Gartner, Z. J., Engineered Tissue Folding by Mechanical Compaction of the Mesenchyme. *Dev Cell* **2018,** *44* (2), 165.
33. Varga, Z. M.; Wegner, J.; Westerfield, M., Anterior movement of ventral diencephalic precursors separates the primordial eye field in the neural plate and requires cyclops. *Development* **1999,** *126* (24), 5533.
34. von Dassow, M.; Davidson, L. A., Physics and the canalization of morphogenesis: a grand challenge in organismal biology. *Phys Biol* **2011,** *8* (4), 045002.
35. Kim, J.; Yoon, J.; Hayward, R. C., Dynamic Display Of Biomolecular Patterns Through An Elastic Creasing Instability Of Stimuli-Responsive Hydrogels. *Nat Mater* **2010,** *9* (2), 159.

36. Kloxin, A. M.; Kasko, A. M.; Salinas, C. N.; Anseth, K. S., Photodegradable hydrogels for dynamic tuning of physical and chemical properties. *Science* **2009,** *324*, 59.
37. Griffin, D. R.; Kasko, A. M., Photodegradable macromers and hydrogels for live cell encapsulation and release. *J Am Chem Soc* **2012,** *134*, 13103.
38. Dempsey, M.; Haines, B. M., Nature of the ground substance in interstitial connective tissue. *Nature* **1949,** *164* (4165), 368.
39. Alberts, B.; Johnson, A. B.; Lewis, J.; Raff, M.; Roberts, K.; Walter, P., The extracellular matrix of animals. In *Molecular biology of the cell*, 4th ed.; Garland Science: New York, **2002**.
40. Rozario, T.; DeSimone, D. W., The extracellular matrix in development and morphogenesis: a dynamic view. *Dev Biol* **2010,** *341* (1), 126.
41. González-Díaz, E.; Varghese, S., Hydrogels as extracellular matrix analogs. *Gels* **2016,** *2* (3), 20.
42. Pierschbacher, M. D.; Ruoslahti, E., Cell attachment activity of fibronectin can be duplicated by small synthetic fragments of the molecule. *Nature* **1984,** *309* (5963), 30.
43. Buck, C. A.; Horwitz, A. F., Cell surface receptors for extracellular matrix molecules. *Annu Rev Cell Biol* **1987,** *3* (1), 179.
44. Shapiro, S. D., Matrix metalloproteinase degradation of extracellular matrix: biological consequences. *Curr Opin Cell Biol* **1998,** *10* (5), 602.
45. Cushing, M. C.; Anseth, K. S., Materials science. Hydrogel cell cultures. *Science* **2007,** *316* (5828), 1133.
46. Tibbitt, M. W.; Anseth, K. S., Hydrogels As extracellular matrix mimics for 3D cell culture. *Biotechnol Bioeng* **2009,** *103*, 655.
47. Hersel, U.; Dahmen, C.; Kessler, H., RGD modified polymers: biomaterials for stimulated cell adhesion and beyond. *Biomaterials* **2003,** *24* (24), 4385.
48. Lutolf, M. P.; Hubbell, J. A., Synthetic biomaterials as instructive extracellular microenvironments for morphogenesis in tissue engineering. *Nat Biotechnol* **2005,** *23* (1), 47.
49. Lutolf, M. P.; Lauer-Fields, J. L.; Schmoekel, H. G.; Metters, A. T.; Weber, F. E.; Fields, G. B.; Hubbell, J. A., Synthetic matrix metalloproteinase-sensitive hydrogels for the conduction of tissue regeneration: engineering cell-invasion characteristics. *Proc Natl Acad Sci U S A* **2003,** *100* (9), 5413.
50. Benoit, D. S.; Durney, A. R.; Anseth, K. S., The effect of heparin-functionalized PEG hydrogels on three-dimensional human mesenchymal stem cell osteogenic differentiation. *Biomaterials* **2007,** *28* (1), 66.
51. Flory, P. J., *Principles Of Polymer Chemistry*. Cornell University Press: Ithaca, **1953**.
52. deGennes, P. G., *Scaling Concepts in Polymer Physics*. Cornell University Press: Ithaca, NY, **1979**.
53. Canal, T.; Peppas, N. A., Correlation between mesh size and equilibrium degree of swelling of polymeric networks. *J Biomed Mater Res* **1989,** *23*, 1183.
54. Peppas, N. A.; Hilt, J. Z.; Khademhosseini, A.; Langer, R., Hydrogels in biology and medicine: from molecular principles to bionanotechnology. *Adv Mater* **2006,** *18* (11), 1345.
55. Anseth, K. S.; Bowman, C. N.; Brannon-Peppas, L., Mechanical properties of hydrogels and their experimental determination. *Biomaterials* **1996,** *17* (17), 1647.

56. Drury, J. L.; Mooney, D. J., Hydrogels for tissue engineering: scaffold design variables and applications. *Biomaterials* **2003,** *24* (24), 4337.
57. DeForest, C. A.; Anseth, K. S., Advances in bioactive hydrogels to probe and direct cell fate. *Annu Rev Chem Biomol Eng* **2012,** *3*, 421.
58. Petersen, O. W.; Rønnov-Jessen, L.; Howlett, A. R.; Bissell, M. J., Interaction with basement membrane serves to rapidly distinguish growth and differentiation pattern of normal and malignant human breast epithelial cells. *Proc Natl Acad Sci U S A* **1992,** *89* (19), 9064.
59. Engler, A. J.; Sen, S.; Sweeney, H. L.; Discher, D. E., Matrix elasticity directs stem cell lineage specification. *Cell* **2006,** *126* (4), 677.
60. Leipzig, N. D.; Shoichet, M. S., The effect of substrate stiffness on adult neural stem cell behavior. *Biomaterials* **2009,** *30* (36), 6867.
61. Gilbert, P. M.; Havenstrite, K. L.; Magnusson, K. E.; Sacco, A.; Leonardi, N. A.; Kraft, P.; Nguyen, N. K.; Thrun, S.; Lutolf, M. P.; Blau, H. M., Substrate elasticity regulates skeletal muscle stem cell self-renewal in culture. *Science* **2010,** *329* (5995), 1078.
62. Nemir, S.; Hayenga, H. N.; West, J. L., PEGDA hydrogels with patterned elasticity: Novel tools for the study of cell response to substrate rigidity. *Biotechnol Bioeng* **2010,** *105* (3), 636.
63. George, E. L.; Georges-Labouesse, E. N.; Patel-King, R. S.; Rayburn, H.; Hynes, R. O., Defects in mesoderm, neural tube and vascular development in mouse embryos lacking fibronectin. *Development* **1993,** *119* (4), 1079.
64. Matsui, T.; Raya, A.; Callol-Massot, C.; Kawakami, Y.; Oishi, I.; Rodriguez-Esteban, C.; Izpisua Belmonte, J. C., miles-apart-Mediated regulation of cell-fibronectin interaction and myocardial migration in zebrafish. *Nat Clin Pract Cardiovasc Med* **2007,** *4 Suppl 1*, S77.
65. Ingber, D. E.; Levin, M., What lies at the interface of regenerative medicine and developmental biology? *Development* **2007,** *134* (14), 2541.
66. Turner, N. J.; Keane, T. J.; Badylak, S. F., Lessons from developmental biology for regenerative medicine. *Birth Defects Res C Embryo Today* **2013,** *99* (3), 149.
67. Beanes, S. R.; Hu, F. Y.; Soo, C.; Dang, C. M.; Urata, M.; Ting, K.; Atkinson, J. B.; Benhaim, P.; Hedrick, M. H.; Lorenz, H. P., Confocal microscopic analysis of scarless repair in the fetal rat: defining the transition. *Plast Reconstr Surg* **2002,** *109* (1), 160.
68. Longaker, M. T.; Whitby, D. J.; Adzick, N. S.; Crombleholme, T. M.; Langer, J. C.; Duncan, B. W.; Bradley, S. M.; Stern, R.; Ferguson, M. W.; Harrison, M. R., Studies in fetal wound healing, VI. Second and early third trimester fetal wounds demonstrate rapid collagen deposition without scar formation. *J Pediatr Surg* **1990,** *25* (1), 63.
69. Redd, M. J.; Cooper, L.; Wood, W.; Stramer, B.; Martin, P., Wound healing and inflammation: embryos reveal the way to perfect repair. *Philos Trans R Soc Lond B Biol Sci* **2004,** *359* (1445), 777.
70. Longaker, M. T.; Chiu, E. S.; Harrison, M. R.; Crombleholme, T. M.; Langer, J. C.; Duncan, B. W.; Adzick, N. S.; Verrier, E. D.; Stern, R., Studies in fetal wound healing. IV. Hyaluronic acid-stimulating activity distinguishes fetal wound fluid from adult wound fluid. *Ann Surg* **1989,** *210* (5), 667.

71. Alaish, S. M.; Yager, D.; Diegelmann, R. F.; Cohen, I. K., Biology of fetal wound healing: hyaluronate receptor expression in fetal fibroblasts. *J Pediatr Surg* **1994,** *29* (8), 1040.
72. Fakhari, A.; Berkland, C., Applications and emerging trends of hyaluronic acid in tissue engineering, as a dermal filler and in osteoarthritis treatment. *Acta Biomater* **2013,** *9* (7), 7081.
73. Neuman, M. G.; Nanau, R. M.; Oruna-Sanchez, L.; Coto, G., Hyaluronic acid and wound healing. *J Pharm Pharm Sci* **2015,** *18* (1), 53.
74. Consortium, I. H. G. S., Initial sequencing and analysis of the human genome. *Nature* **2001,** *409* (6822), 860.
75. Consortium, I. H. G. S., Finishing the euchromatic sequence of the human genome. *Nature* **2004,** *431* (7011), 931.
76. Cochran, W. J. Malrotation of the bowel *The Merck manual* [Online], **2018**.
77. Armon, S.; Efrati, E.; Kupferman, R.; Sharon, E., Geometry and mechanics in the opening of chiral seed pods. *Science* **2011,** *333* (6050), 1726.
78. Bassik, N.; Abebe, B. T.; Laflin, K. E.; Gracias, D. H., Photolithographically Patterned Smart Hydrogel Based Bilayer Actuators. *Polymer* **2010,** *51*, 6093.
79. Vasiev, I.; Greer, A. I. M.; Khokhar, A. Z.; Stormonth-Darling, J.; Tanner, K. E.; Gadegaard, N., Self-folding nano- and micropatterned hydrogel tissue engineering scaffolds by single step photolithographic process. *Microelectron Eng* **2013,** *108*, 76.
80. Yoon, C.; Xiao, R.; Park, J.; Cha, J.; Nguyen, T. D.; Gracias, D. H., Functional stimuli responsive hydrogel devices by self-folding. *Smart Mater Struct* **2014,** *23*, 094008.
81. Klein, Y.; Efrati, E.; Sharon, E., Shaping of elastic sheets by prescription of non-Euclidean metrics. *Science* **2007,** *315*, 1116.
82. Richter, A.; Paschew, G., Optoelectrothermic control of highly integrated polymer-based MEMs applied in an artificial skin. *Adv Mater* **2009,** *21*, 979.
83. Zakharchenko, S.; Puretskiy, N.; Stoychev, G.; Stamm, M.; Ionov, L., Temperature controlled encapsulation and release using partially biodegradable thermo-magneto-sensitive self-rolling tubes. *Soft Matter* **2010,** *6*, 2633.
84. Fujigaya, T.; Morimoto, T.; Niidome, Y.; Nakashima, N., NIR Laser-driven reversible volume phase transition of single-walled carbon nanotube/poly(N-Isopropylacrylamide) composite gels. *Adv Mater* **2008,** *20*, 3610.
85. Juodkazis, S.; Mukai, N.; Wakaki, R.; Yamaguchi, A.; Matsuo, S.; Misawa, H., Reversible phase transitions in polymer gels induced by radiation forces. *Nature* **2000,** *408*, 178.
86. Zhang, X.; Pint, C. L.; Lee, M. H.; Schubert, B. E.; Jamshidi, A.; Takei, K.; Ko, H.; Gillies, A.; Bardhan, R.; Urban, J. J.; Wu, M.; Fearing, R.; Javey, A., Optically- and thermally-responsive programmable materials based on carbon nanotube-hydrogel polymer composites. *Nano Lett* **2011,** *11*, 3239.
87. Therien-Aubin, H.; Wu, Z. L.; Nie, Z. H.; Kumacheva, E., Multiple shape transformations of composite hydrogel sheets. *J Am Chem Soc* **2013,** *135*, 4834.
88. Wu, Z. L.; Moshe, M.; Greener, J.; Therien-Aubin, H.; Nie, Z. H.; Sharon, E.; Kumacheva, E., Three-dimensional shape transformations of hydrogel sheets induced by small-scale modulation of internal stresses. *Nat Commun* **2013,** *4*, 1586.

89. Gladman, S. A.; Matsumoto, E. A.; Nuzzo, R. G.; Mahadevan, L.; Lewis, J. A., Biomimetic 4D Printing. *Nat Mater* **2016,** *15*, 413.
90. Capadona, J. R.; Shanmuganathan, K.; Tyler, D. J.; Rowan, S. J.; Weder, C., Stimuli-Responsive Polymer Nanocomposites Inspired by the Sea Cucumber Dermis. *Science* **2008,** *319* (5868), 1370.
91. Shanmuganathan, K.; Capadona, J. R.; Rowan, S. J.; Weder, C., Biomimetic mechanically adaptive nanocomposites. *Prog Polym Sci* **2010,** *35* (1-2), 212.
92. Schild, H. G., Poly (N-Isopropylacrylamide) - Experiment, Theory And Application. *Prog Polym Sci* **1992,** *17*, 163.
93. Guan, Y.; Zhang, Y. J., PNIPAM Microgels For Biomedical Applications: From Dispersed Particles To 3d Assemblies *Soft Matter* **2011,** *7*, 6375.
94. Stoychev, G.; Puretskiy, N.; Ionov, L., Self-Folding All-Polymer Thermoresponsive Microcapsules. *Soft Matter* **2011,** *7*, 3277.
95. Chen, D.; Hyldahl, R. D.; Hayward, R. C., Creased Hydrogels As Active Platforms For Mechanical Deformation Of Cultured Cells. *Lab Chip* **2015,** *15*, 1160.
96. Stroganov, V.; Zakharchenko, S.; Sperling, E.; Meyer, A. K.; Schmidt, O. G.; Ionov, L., Biodegradable Self-Folding Polymer Films With Controlled Thermo-Triggered Folding. *Adv Funct Mater* **2014,** *24*, 4357.
97. Jamal, M.; Bassik, N.; Cho, J. H.; Randall, C. L.; Gracias, D. H., Directed Growth Of Fibroblasts Into Three Dimensional Micropatterned Geometries Via Self-Assembling Scaffolds. *Biomaterials* **2010,** *31*, 1683.
98. Ruskowitz, E. R.; DeForest, C. A., Photoresponsive biomaterials for targeted drug delivery and 4D cell culture. *Nat Rev Mater* **2018,** *3*, 17087.
99. Kaplan, J. H.; Forbush, B., 3rd; Hoffman, J. F., Rapid photolytic release of adenosine 5'-triphosphate from a protected analogue: utilization by the Na:K pump of human red blood cell ghosts. *Biochemistry* **1978,** *17* (10), 1929.
100. Norris, S. C. P.; Chou, T.; Kasko, A. M., Diffusion of Photoabsorbing Degradation Byproducts in Photodegradable Polymer Networks. *Macromol Theory Simul* **2017,** *26* (4), 1700007.
101. Tibbitt, M. W.; Kloxin, A. M.; Sawicki, L.; Anseth, K. S., Mechanical Properties and Degradation of Chain and Step Polymerized Photodegradable Hydrogels. *Macromolecules* **2013,** *46*, 2785.
102. Pezzulla, M.; Smith, G. P.; Nardinocchi, P.; Holmes, D. P., Geometry and mechanics of thin growing bilayers. *Soft Matter* **2016,** *12* (19), 4435.
103. Donnan, F. G.; Guggenheim, E. A., *Z Phys Chem* **1932,** *A162* (346).
104. Wells, R. G., The role of matrix stiffness in regulating cell behavior. *Hepatology* **2008,** *47* (4), 1394.
105. Schindelin, J.; Arganda-Carreras, I.; Frise, E.; Kaynig, V.; Longair, M.; Pietzsch, T.; Preibisch, S.; Rueden, C.; Saalfeld, S.; Schmid, B.; Tinevez, J. Y.; White, D. J.; Hartenstein, V.; Eliceiri, K.; Tomancak, P.; Cardona, A., Fiji: An Open-Source Platform For Biological-Image Analysis. *Nat Methods* **2012,** *9*, 676.
106. Griffith, C. K.; Miller, C.; Sainson, R. C. A.; Calvert, J. W.; Jeon, N. L.; Hughes, C. C. W.; George, S. C., Diffusion limits of an in vitro thick prevascularized tissue. *Tissue Eng Part A* **2005,** *11* (1-2), 257.
107. Alben, S.; Balakrisnan, B.; Smela, E., Edge effects determine the direction of bilayer bending. *Nano Lett* **2011,** *11* (6), 2280.

108. Hou, M. T. K.; Chen, R. S., Effect of width on the stress-induced bending of micromachined bilayer cantilevers. *J Micromechanics Microengineering* **2003,** *13* (1), 141.
109. Mansfield, E. H., Bending, Buckling and Curling of a Heated Thin Plate. *Proc R Soc Lond A Math Phys Sci* **1962,** *268* (1334), 316.
110. Mansfield, E. H., Bending Buckling and Curling of a Heated Elliptical Plate. *Proc R Soc Lond A Math Phys Sci* **1965,** *288* (1414), 396.
111. Freund, L. B., Substrate curvature due to thin film mismatch strain in the nonlinear deformation range. *J Mech Phys Solids* **2000,** *48* (6-7), 1159.
112. Ionov, L., Biomimetic Hydrogel-Based Actuating Systems. *Adv Funct Mater* **2013,** *23* (36), 4555.
113. Chun, I. S.; Challa, A.; Derickson, B.; Hsia, K. J.; Li, X., Geometry effect on the strain-induced self-rolling of semiconductor membranes. *Nano Lett* **2010,** *10* (10), 3927.
114. Nerurkar, N. L.; Mahadevan, L.; Tabin, C. J., BMP signaling controls buckling forces to modulate looping morphogenesis of the gut. *Proc Natl Acad Sci U S A* **2017,** *114* (9), 2277.
115. Trietsch, S. J.; Naumovska, E.; Kurek, D.; Setyawati, M. C.; Vormann, M. K.; Wilschut, K. J.; Lanz, H. L.; Nicolas, A.; Ng, C. P.; Joore, J.; Kustermann, S.; Roth, A.; Hankemeier, T.; Moisan, A.; Vulto, P., Membrane-free culture and real-time barrier integrity assessment of perfused intestinal epithelium tubes. *Nat Commun* **2017,** *8* (1), 262.
116. Flory, P. J., *Stastical Mechanics of Chain Molecules*. Wiley: New York, **1969**.
117. Rubinstein, M.; Colby, R. H., *Polymer Physics*. OUP Oxford: **2003**.
118. Wei, Z.; Jia, Z.; Athas, J.; Wang, C.; Raghavan, S. R.; Li, T.; Nie, Z., Hybrid Hydrogel Sheets That Undergo Pre-Programmed Shape Transformations. *Soft Matter* **2014,** *10* (41), 8157.
119. Fournier, J. B., Nontopological saddle-splay and curvature instabilities from anisotropic membrane inclusions. *Phys Rev Lett* **1996,** *76* (23), 4436.
120. Jinnai, H.; Watashiba, H.; Kajihara, T.; Nishikawa, Y.; Takahashi, M.; Ito, M., Surface curvatures of trabecular bone microarchitecture. *Bone* **2002,** *30* (1), 191.
121. Harvey, R. P., Patterning the vertebrate heart. *Nat Rev Genet* **2002,** *3* (7), 544.
122. Taber, L. A.; Perucchio, R., Modeling heart development. *J Elast* **2000,** *61* (1-3), 165.
123. Nerurkar, N. L.; Ramasubramanian, A.; Taber, L. A., Morphogenetic adaptation of the looping embryonic heart to altered mechanical loads. *Dev Dyn* **2006,** *235* (7), 1822.
124. Bruneau, B. G.; Nemer, G.; Schmitt, J. P.; Charron, F.; Robitaille, L.; Caron, S.; Conner, D. A.; Gessler, M.; Nemer, M.; Seidman, C. E.; Seidman, J. G., A murine model of Holt-Oram syndrome defines roles of the T-box transcription factor Tbx5 in cardiogenesis and disease. *Cell* **2001,** *106* (6), 709.
125. Linask, K. K.; Lash, J. W., Early heart development: dynamics of endocardial cell sorting suggests a common origin with cardiomyocytes. *Dev Dyn* **1993,** *196* (1), 62.
126. Palmer, S.; Groves, N.; Schindeler, A.; Yeoh, T.; Biben, C.; Wang, C. C.; Sparrow, D. B.; Barnett, L.; Jenkins, N. A.; Copeland, N. G.; Koentgen, F.; Mohun, T.; Harvey, R. P., The small muscle-specific protein Csl modifies cell shape and promotes myocyte fusion in an insulin-like growth factor 1-dependent manner. *J Cell Biol* **2001,** *153* (5), 985.

127. Lyons, I.; Parsons, L. M.; Hartley, L.; Li, R.; Andrews, J. E.; Robb, L.; Harvey, R. P., Myogenic and morphogenetic defects in the heart tubes of murine embryos lacking the homeo box gene Nkx2-5. *Genes Dev* **1995,** *9* (13), 1654.
128. Striedter, G. F.; Srinivasan, S.; Monuki, E. S., Cortical folding: when, where, how, and why? *Annu Rev Neurosci* **2015,** *38*, 291.
129. Richman, D. P.; Stewart, R. M.; Hutchinson, J. W.; Caviness, V. S., Jr., Mechanical model of brain convolutional development. *Science* **1975,** *189* (4196), 18.
130. Tallinen, T.; Chung, J. Y.; Biggins, J. S.; Mahadevan, L., Gyrification from constrained cortical expansion. *Proc Natl Acad Sci U S A* **2014,** *111* (35), 12667.
131. Nelson, C. M., On Buckling Morphogenesis. *J Biomech Eng* **2016,** *138* (2), 021005.
132. Taber, L. A., Mechanical aspects of cardiac development. *Prog Biophys Mol Biol* **1998,** *69* (2-3), 237.
133. Odell, G. M.; Oster, G.; Alberch, P.; Burnside, B., The mechanical basis of morphogenesis. I. Epithelial folding and invagination. *Dev Biol* **1981,** *85* (2), 446.
134. Wen, F. L.; Wang, Y. C.; Shibata, T., Epithelial Folding Driven by Apical or Basal-Lateral Modulation: Geometric Features, Mechanical Inference, and Boundary Effects. *Biophys J* **2017,** *112* (12), 2683.
135. Zong, X.; Bien, H.; Chung, C. Y.; Yin, L.; Fang, D.; Hsiao, B. S.; Chu, B.; Entcheva, E., Electrospun fine-textured scaffolds for heart tissue constructs. *Biomaterials* **2005,** *26* (26), 5330.
136. Ghrebi, S.; Hamilton, D. W.; Douglas Waterfield, J.; Brunette, D. M., The effect of surface topography on cell shape and early ERK1/2 signaling in macrophages; linkage with FAK and Src. *J Biomed Mater Res A* **2013,** *101* (7), 2118.
137. Simitzi, C.; Karali, K.; Ranella, A.; Stratakis, E., Controlling the Outgrowth and Functions of Neural Stem Cells: The Effect of Surface Topography. *ChemPhysChem* **2018,** *19*, 1143.
138. Barriga, E. H.; Franze, K.; Charras, G.; Mayor, R., Tissue stiffening coordinates morphogenesis by triggering collective cell migration in vivo. *Nature* **2018,** *554* (7693), 523.
139. Tsang, K. M. C.; Annabi, N.; Ercole, F.; Zhou, K.; Karst, D. J.; Li, F. Y.; Haynes, J. M.; Evans, R. A.; Thissen, H.; Khademhosseini, A.; Forsythe, J. S., Facile One-Step Micropatterning Using Photodegradable Gelatin Hydrogels for Improved Cardiomyocyte Organization and Alignment. *Adv Funct Mater* **2015,** *25* (6), 977.
140. Kim, D. H.; Lipke, E. A.; Kim, P.; Cheong, R.; Thompson, S.; Delannoy, M.; Suh, K. Y.; Tung, L.; Levchenko, A., Nanoscale cues regulate the structure and function of macroscopic cardiac tissue constructs. *Proc Natl Acad Sci U S A* **2010,** *107* (2), 565.
141. Li, J.; Minami, I.; Shiozaki, M.; Yu, L.; Yajima, S.; Miyagawa, S.; Shiba, Y.; Morone, N.; Fukushima, S.; Yoshioka, M.; Li, S.; Qiao, J.; Li, X.; Wang, L.; Kotera, H.; Nakatsuji, N.; Sawa, Y.; Chen, Y.; Liu, L., Human Pluripotent Stem Cell-Derived Cardiac Tissue-like Constructs for Repairing the Infarcted Myocardium. *Stem Cell Reports* **2017,** *9* (5), 1546.
142. Zhao, Y.; Zeng, H.; Nam, J.; Agarwal, S., Fabrication of skeletal muscle constructs by topographic activation of cell alignment. *Biotechnol Bioeng* **2009,** *102* (2), 624.

143. Bettadapur, A.; Suh, G. C.; Geisse, N. A.; Wang, E. R.; Hua, C.; Huber, H. A.; Viscio, A. A.; Kim, J. Y.; Strickland, J. B.; McCain, M. L., Prolonged Culture of Aligned Skeletal Myotubes on Micromolded Gelatin Hydrogels. *Sci Rep* **2016,** *6*, 28855.
144. Mathur, A. B.; Collinsworth, A. M.; Reichert, W. M.; Kraus, W. E.; Truskey, G. A., Endothelial, Cardiac Muscle And Skeletal Muscle Exhibit Different Viscous And Elastic Properties As Determined By Atomic Force Microscopy. *J Biomech* **2001,** *34*, 1545.
145. Jacot, J. G.; McCulloch, A. D.; Omens, J. H., Substrate stiffness affects the functional maturation of neonatal rat ventricular myocytes. *Biophys J* **2008,** *95* (7), 3479.
146. Boothe, S. D.; Myers, J. D.; Pok, S.; Sun, J.; Xi, Y.; Nieto, R. M.; Cheng, J.; Jacot, J. G., The Effect of Substrate Stiffness on Cardiomyocyte Action Potentials. *Cell Biochem Biophys* **2016,** *74* (4), 527.
147. Wong, D. Y.; Griffin, D. R.; Reed, J.; Kasko, A. M., Photodegradable Hydrogels to Generate Positive and Negative Features over Multiple Length Scales. *Macromolecules* **2010,** *43* (6), 2824.
148. Hosseini, V.; Ahadian, S.; Ostrovidov, S.; Camci-Unal, G.; Chen, S.; Kaji, H.; Ramalingam, M.; Khademhosseini, A., Engineered Contractile Skeletal Muscle Tissue on a Microgrooved Methacrylated Gelatin Substrate. *Tissue Engineering Part A* **2012,** *18* (23-24), 2453.
149. Born, M.; Wolf, E., *Principles of Optics*. Cambridge University Press: **1997**; Vol. 7.
150. Kumar, T.; Majumdar, A.; Das, P.; Sarafis, V.; Ghose, M., Trypan blue as a fluorochrome for confocal laser scanning microscopy of arbuscular mycorrhizae in three mangroves. *Biotech Histochem* **2008,** *83* (3-4), 153.
151. Kubin, R. F.; Fletcher, A. N., Fluorescence quantum yields of some rhodamine dyes. *J Lumin* **1982,** *27* (4), 455.
152. Wong, D. Y.; Ranganath, T.; Kasko, A. M., Low-dose, long-wave UV light does not affect gene expression of human mesenchymal stem cells. *PLoS One* **2015,** *10*, e0139307.
153. Pernus, F.; Erzen, I., Arrangement Of Fiber Types Within Fascicles Of Human Vastus Lateralis Muscle. *Muscle Nerve* **1991,** *14*, 304.
154. Staron, R. S.; Hagerman, F. C.; Hikida, R. S.; Murray, T. F.; Hostler, D. P.; Crill, M. T.; Ragg, K. E.; Toma, K., Fiber Type Composition Of The Vastus Lateralis Muscle Of Young Men And Women. *J Histochem Cytochem* **2000,** *48*, 623.
155. Burattini, S.; Ferri, P.; Battistelli, M.; Curci, R.; Luchetti, F.; Falcieri, E., C2C12 Murine Myoblasts As A Model Of Skeletal Muscle Development: Morpho-Functional Characterization. *Eur J Histochem* **2004,** *48*, 223.
156. Kolluru, G. K.; Sinha, S.; Majumder, S.; Muley, A.; Siamwala, J. H.; Gupta, R.; Chatterjee, S., Shear stress promotes nitric oxide production in endothelial cells by sub-cellular delocalization of eNOS: A basis for shear stress mediated angiogenesis. *Nitric Oxide* **2010,** *22* (4), 304.
157. Fleming, I.; Busse, R., Molecular mechanisms involved in the regulation of the endothelial nitric oxide synthase. *Am J Physiol Regul Integr Comp Physiol* **2003,** *284* (1), R1.
158. Balaguru, U. M.; Sundaresan, L.; Manivannan, J.; Majunathan, R.; Mani, K.; Swaminathan, A.; Venkatesan, S.; Kasiviswanathan, D.; Chatterjee, S., Disturbed flow

mediated modulation of shear forces on endothelial plane: A proposed model for studying endothelium around atherosclerotic plaques. *Sci Rep* **2016,** *6*, 27304.
159. Chien, S., Mechanotransduction and endothelial cell homeostasis: the wisdom of the cell. *Am J Physiol Heart Circ Physiol* **2007,** *292* (3), H1209.
160. Kaunas, R.; Nguyen, P.; Usami, S.; Chien, S., Cooperative effects of Rho and mechanical stretch on stress fiber organization. *Proc Natl Acad Sci U S A* **2005,** *102* (44), 15895.
161. Sipkema, P.; van der Linden, P. J.; Westerhof, N.; Yin, F. C., Effect of cyclic axial stretch of rat arteries on endothelial cytoskeletal morphology and vascular reactivity. *J Biomech* **2003,** *36* (5), 653.
162. Lacolley, P., Mechanical influence of cyclic stretch on vascular endothelial cells. *Cardiovasc Res* **2004,** *63* (4), 577.
163. Nerem, R. M.; Levesque, M. J.; Cornhill, J. F., Vascular endothelial morphology as an indicator of the pattern of blood flow. *J Biomech Eng* **1981,** *103* (3), 172.
164. Malek, A. M.; Izumo, S., Mechanism of endothelial cell shape change and cytoskeletal remodeling in response to fluid shear stress. *J Cell Sci* **1996,** *109 (Pt 4)*, 713.
165. Mironi-Harpaz, I.; Wang, D. Y.; Venkatraman, S.; Seliktar, D., Photopolymerization of cell-encapsulating hydrogels: crosslinking efficiency versus cytotoxicity. *Acta Biomater* **2012,** *8*, 1838.
166. Fairbanks, B. D.; Schwartz, M. P.; Bowman, C. N.; Anseth, K. S., Photoinitiated polymerization of PEG-diacrylate with lithium phenyl-2,4,6-trimethylbenzoylphosphinate: polymerization rate and cytocompatibility. *Biomaterials* **2009,** *30* (35), 6702.
167. Ki, C. S.; Shih, H.; Lin, C. C., Facile preparation of photodegradable hydrogels by photopolymerization. *Polymer* **2013,** *54* (8), 2115.
168. Rosales, A. M.; Vega, S. L.; DelRio, F. W.; Burdick, J. A.; Anseth, K. S., Hydrogels with reversible mechanics to probe dynamic cell microenvironments. *Angew Chem Int Edit* **2017,** *56* (40), 12132.
169. Bagdasaryan, K.; Sinitsina, Z. A., Polymerization Inhibition by Aromatic Compounds. *Journal of Polymer Science* **1961,** *52* (157), 31.
170. Van Den Bulcke, A. I.; Bogdanov, B.; De Rooze, N.; Schacht, E. H.; Cornelissen, M.; Berghmans, H., Structural and rheological properties of methacrylamide modified gelatin hydrogels. *Biomacromolecules* **2000,** *1* (1), 31.
171. Nichol, J. W.; Koshy, S. T.; Bae, H.; Hwang, C. M.; Yamanlar, S.; Khademhosseini, A., Cell-laden microengineered gelatin methacrylate hydrogels. *Biomaterials* **2010,** *31* (21), 5536.
172. Aubin, H.; Nichol, J. W.; Hutson, C. B.; Bae, H.; Sieminski, A. L.; Cropek, D. M.; Akhyari, P.; Khademhosseini, A., Directed 3D cell alignment and elongation in microengineered hydrogels. *Biomaterials* **2010,** *31* (27), 6941.
173. Polson, A.; Potgieter, G. M.; Largier, J. F.; Mears, G. E.; Joubert, F. J., The fractionation of protein mixtures by linear polymers of high molecular weight. *Biochim Biophys Acta* **1964,** *82*, 463.
174. Hicks, M. R.; Hiserodt, J.; Paras, K.; Fujiwara, W.; Eskin, A.; Jan, M.; Xi, H.; Young, C. S.; Evseenko, D.; Nelson, S. F.; Spencer, M. J.; Handel, B. V.; Pyle, A. D., ERBB3 and NGFR mark a distinct skeletal muscle progenitor cell in human development and hPSCs. *Nat Cell Biol* **2018,** *20* (1), 46.